Marshall Plan Scholarship Research Report

In Situ Mechanical Cyclic Testing of Nanostructured Alloys

Cameron Howard

Adviser
Assoc. Prof. Dr. Peter Hosemann
University of California, Berkeley, USA

Co-Adviser
Assoc. Prof. Dr. Daniel Kiener
Montanuniversität Leoben, Austria

This work has been carried out at the Department of Nuclear Engineering, University of California, Berkeley, USA, in cooperation with the Department of Materials Physics, Montanuniversität Leoben, Austria.

April 7, 2015

1

Affidavit

I declare in lien of oath, that I wrote this thesis and performed the associated research myself, using only literature cited in this volume.

April 7, 2015
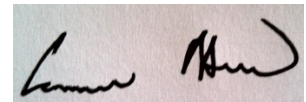
_____

Cameron Howard

Acknowledgments

Abstract

The objective of this research proposal is to perform a new method of micro scale in situ mechanical testing on candidate reactor materials that focuses on the evolution of fatigue properties by correlating mechanical properties with sample microstructure and observed damage mechanisms. As received and nanostructured materials will be investigated. This work will compose a significant portion of a doctoral thesis in the department of nuclear engineering at University of California Berkeley.

Ultra small scale mechanical testing has been made possible due to the development of focused ion beam instruments and nanoindentation equipment. In 2004, M. Uchic et al. [1] introduced micro compression testing to the scientific community as a means to examine size effects in micrometer sized single crystal compression specimens using a truncated Berkovich tip in a conventional nanoindenter. Since that many basic science papers were published where mechanical materials properties such as yield strength and elastic modulus are characterized. However, now with the availability of these techniques and an initial understanding of the basic science, engineering components such as reactor and spallation source materials analysis can benefit from it. Small scale samples provide many benefits including reduction in the amount of material necessary to obtain information about a material's mechanical properties, availability of ion beam and reactor irradiated materials for mechanical testing, fundamental insight in structure-property relationships, increased statistics on less sample material, direct observation of sample deformation, and cost reductions. Nanostructured alloys, ultra-fine grained material, and oxide dispersion strengthened materials have spiked the interest of the nuclear materials community for fusion and fission applications.

Some small scale mechanical tests and size effects studies have been performed on candidate reactor materials and basic science materials via nanoindentation, micro compression testing, and bending tests. The aim of this project is to fabricate micron scale rods out of nanostructured candidate reactor materials and basic science materials brought from UC Berkeley at the Montanuniversität Leoben using a Zeiss 1540 XB focused ion beam (FIB) workstation and subsequently test these materials in situ in a scanning electron microscope (SEM, Leo 982) at room temperature.

Significant outcomes and benefits of this project will be a fundamental understanding of the failure mechanisms of reactor components which will add insight into new testing methods for reactor lifetime extension program.

Abbreviations and Symbols

a	....	crack length
A	....	amplitude ratio
a_c	....	critical crack length
ARB	....	Accumulative Roll Bonding
b	....	Burgers vector, HCF strength exponent
bcc	....	body centered cubic
c	....	fatigue ductility exponent
d_1, d_2	....	indent diagonal distances
d_c	....	cell size
DC	....	dislocation climbing
DS	....	dislocation sinks
$d\phi$	....	bend angle
E	....	elastic modulus
EBSD	....	Electron Backscatter Diffraction
ECAP	....	Equal Channel Angular Pressing
F	....	Force
fcc	....	face centered cubic
FIB	....	Focused Ion Beam
FSP	....	Friction Stir Processing
G	....	shear modulus
GB	....	Grain Boundary
GBS	....	Grain Boundary Sliding
GD	....	dislocation gliding

MGB	……………………………………………	migrating grain boundaries
h	……………………………………………	sample thickness
HCF	……………………………………………	High Cycle Fatigue
HPT	……………………………………………	High Pressure Torsion
HV	……………………………………………	Vickers Hardness
I	……………………………………………	moment of inertia
k	……………………………………………	thermal conductivity, Hall-Petch paramter
K_c	……………………………………………	fracture toughness
LCF	……………………………………………	Low Cycle Fatgiue
l	……………………………………………	length after deformation
l_o	……………………………………………	original length
l_b	……………………………………………	bending length
M	……………………………………………	bending moment
MA	……………………………………………	Mechanical Alloying
N	……………………………………………	number of rotations, number of cycles
ODS	……………………………………………	Oxide Dispersion Strengthened
P	……………………………………………....	Force
PSB	……………………………………………	Persistent Slip Bands
PVD	……………………………………………	Plasma Vapor Deposition
r	……………………………………………	radial distance from center
R	……………………………………………	stress ratio
RT	……………………………………………	Room Temperature
S, σ	……………………………………………	stress
SD	……………………………………………	dislocation sources
SEM	……………………………………………	Scanning Electron Microscope
SPD	……………………………………………	Severe Plastic Deformation
SSMT	……………………………………………	Small Scale Mechanical Testing
T	……………………………………………	temperature
T_m	……………………………………………	melting temperature
TD	……………………………………………	Thoria Dispersed
TEM	……………………………………………	Transmission Electron Microscopy

u	…………………………………………	indenter displacement
UFG	…………………………………………	Ultra Fine Grained
UTS	…………………………………………	Ultimate Tensile Stress
Y	…………………………………………	specimen geometry factor
α	…………………………………………	thermal expansion coefficient
ΔK	…………………………………………	stress intensity parameter
ΔK_{th}	…………………………………………	crack growth threshold
Δl	…………………………………………	change in length due to deformation
δL	…………………………………………	bend bar length
ε	…………………………………………	strain
ε_a	…………………………………………	strain amplitude
ε_{el}	…………………………………………	elastic strain
ε_f'	…………………………………………	fatigue ductility coefficient
ε_{pl}	…………………………………………	plastic strain
κ	…………………………………………	curvature
γ	…………………………………………	shear strain
ϕ	…………………………………………	channel-intersection angle
ρ	…………………………………………	dislocation density, radius of curvature
σ_a	…………………………………………	stress amplitude
σ_d	…………………………………………	dislocation stress
σ_f	…………………………………………	mean fatigue strength
σ_f'	…………………………………………	fatigue strength coefficient
σ_m	…………………………………………	mean stress
σ_{max}	…………………………………………	maximum stress of a fatigue cycle
σ_{min}	…………………………………………	minimum stress of a fatigue cycle
σ_o	…………………………………………	single crystal yield stress
$\sigma_r, \Delta\sigma$	…………………………………………	stress range
σ_{th}	…………………………………………	thermal stress
σ_y	…………………………………………	yield stress
Ψ	…………………………………………	arc of curvature

Contents

1. Introduction

During the past decades, interest in nanostructured alloys significantly increased, which is shown by the recent rise of publications regarding these materials. This is justified by three main contributions: their increased strength and ductility [2, 3], improvements in high temperature creep properties [4-15], and added radiation resistance [16]; a number of new severe plastic deformation and processing techniques [17-26]; and the increased ability to examine these materials in situ at smaller scales using SSMT and FIB techniques [27].

The effectiveness of the Y_2O_3 nano oxide particles in oxide dispersion strengthened steels as defect sinks for atoms displaced during radiation and radiation particles themselves and the ability to control the size and distribution of these particles as well as the steel's grain structure makes it a prime candidate for fast reactor fuel cladding as well as opens up considerations for it being used as a safe structural material for fusion reactors [28].

Due to their nanostructures, the deformation of these materials and their mechanical properties can no longer be described by classical theories [29, 30]. Efforts have been made to investigate intrinsic and extrinsic size effects from nanostructured alloys [31] as well as irradiation effects on single crystal basic science materials [32] using nanoindentation and micro compression. Size effects have also been investigated in monotonic loading tests involving tension [33, 34] and bending [35-37].

The majority of commercially viable nanostructured alloys are either ODS manufactured by ball milling powders and subsequent hot extrusion, rolling, and annealing [38] or made by ECAP because it can be scaled up to produce large bulk samples [39] and has been incorporated into conventional rolling mills for continuous processing [40, 41].

It has been surmised that the interfaces in the nano layered composite Cu-Nb act as slip obstacles and radiation defect sinks [42, 43]. In addition, it exhibits enhanced strength, thermal stability, and shock resistance superior to that of course grained materials. Much work has been done to attempt to match the interface structure of Cu-Nb to its mechanical properties for composites produced via PVD and ARB of constant chemistry [44]. However, a systematic investigation of many different compositions of various Cu-Nb composites produced by ball milling and subsequent HPT is rarely investigated. This would be another effective way of controlling critical parameters that define local interface structure.

Many fatigue studies of UFG metals and alloys have been conducted with large scale samples on the order of tens of millimeters or larger with a specific focus on studying ECAP materials [45]. Cyclic loading in small dimensions has only been investigated with respect to thin films [46], small in only one dimension, as well as for thin wires pulled in tension [47, 48], and cyclic indentation where all stresses are compressive [49, 50]. SSMT of nanostructured alloys under low cycle fatigue with a focus on studying load sign changes in small dimensions and how they affect cyclic plastic deformation behavior, specifically in ODS and HPT materials, have seldom if at all been performed. In order to acquire a better understanding of these materials and the evolution of their microstructure and mechanical properties as a function of cyclic stress under full load reversal on the micro and nano scale, these tests must be performed.

There is no doubt that nanostructured engineering alloys play a major role in a plethora of applications and involve an enormous innovation potential, and we hope that our in situ low cycle fatigue studies concerning the mechanical properties and microstructural evolution of single crystal and ECAP Cu and single crystal and HPT PM 2000 as well as our production

and analysis of Cu/Nb produced by combining ball milling and HPT will contribute to the body of knowledge.

2. Theoretical Background

2.1 Copper

Astronomers believe that most copper found on earth was fused in supergiant stars. When these stars die, they form supernovae that terminate in catastrophic explosion and launch the newly minted copper into space. Approximately four and a half billion years ago, when earth was formed, it grabbed and inherited some of this copper. From the time humanity has occupied earth, copper (lat. cuprum) has been known to and utilized by mankind. After gold and meteoric iron, it is the third metal to be used by humans. For over 10,000 years it has been society's tool and has been found among ancient burial sites dating back to 9000-8700 BC in northern Iraq in the form of pendants. The Chalcolithic period or Copper Age when humans began manufacturing Cu at high temperature began in 5000 BCE in Belovode on the Rudnik Mountain in Serbia [51]. Soon after, evidence of Cu smelting was seen in the UHP Cu axe found with Otzi the Iceman who lived around 3300 BC [52]. This then fueled the fire for alloying with tin and the start of the Bronze Age.

In ancient Greek and Roman times, copper was mined in Cyprus and called *Cyprium*, later simplified to *cuprum* and anglicized to copper. It is a fairly common element with about 1 kg laying in each 15-20 tons of earth's crust [53] translating to an estimated few billion tons that is economically recoverable. Sources of Cu are widespread and unequally distributed with six of the ten largest mines in the world being situated in Chile, two in Peru, and one in

Mexico. The other stands in Grasberg, Indonesia but high amounts of copper reserves over 30,000 tonnes also exist in Australia, The United States, China, and Russia.

Chemical, physical, as well as known mechanical properties of conventional pure copper to be used in the report are displayed in table 2.1.

Table 2.1 Properties of pure bulk Cu

Atomic Number	29
Standard Atomic Weight	63.546
Density	8.96 g/cm^3
Melting Point	1357.8 K
Thermal Conductivity	401 W/mK
Bulk Tensile Strength	100 MPa
Young's Modulus	110-128 GPa
Shear Modulus	48 GPa
Poisson's Ratio	0.34
Hardness	343-369 MPa
Lattice Type	Face-centered cubic (fcc)
Burgers vector	0.255 nm
Stacking fault energy	70-78 mJ/m^2
HPT – steady state hardness [54]	1275 MPa
HPT – steady state grain size [55]	530 nm

2.2 Mechanical Alloying

Mechanical alloying and the birth of ODS type alloy products began in 1910 with thoriated tungsten. Edison and J.W. Swan had invented electrical lamps in 1879, but all the early lamps of this period had been using carbon filaments that had inherent brittleness, low light

outputs and short lifetimes in addition to blackening the lightbulb after use. Thus, a search for better incandescent materials began. Early movements were towards Carl Auer von Welsbach's gas mantle lamps in 1883 [56] and Walther Nernst's ceramic rod lamps in 1898 [57]. The disadvantages of these lamps are there risk of being a fire hazard and the fact that the ceramic rod was not electrically conductive at RT, so it required a separate heater filament. After, a third lamp using a complicated process involving Osmium paste was manufactured in 1898 [58] and then in 1902 Tantalum wires were developed by von Bolton and Feuerlein [59]. These proved inefficient due to the high evaporation rate of Osmium filaments and brittleness of Tantalum when running alternating currents. Finally, in 1903, tungsten filaments arrived thanks to A. Just and F. Hanaman [60]. From 1905 to 1911 tungsten filaments were produced with a carbonless binder paste mixture that was extruded through fine diamond dies, wound into wire loops, cut into hairpins, and heated to a red heat to remove the binder. The hairpins were mounted in clips and heated via current in an H_2 atmosphere, sintering the tungsten particles together to produce a solid metallic tungsten filament. Meanwhile, Coolidge had developed a way of making tungsten filaments more ductile by amalgamating them with Hg, Cd, and Bi and flattening them between heated steel blocks or rollers [61]. In January 1910, Coolidge realized that when his tungsten oxide was heated in clay Battersea-type crucibles, the tungsten filaments lasted longer and did not sag due to increased resistance to grain off-setting. After, he proved that this wasn't a special effect of the crucibles by intentionally mixing the tungsten powder with many different refractory metals that produced the same results, noting that thorium nitrate and thoriated tungsten proved to be most ductile. This is the first time the influencing positive effect of minor amounts of foreign elements was clearly recognized and metal processing via doping and oxide dispersion strengthening was born [62, 63].

After Coolidge, Mechanical Alloying (MA) in the 20th century evolved into primarily focusing on either nickel or aluminum as shown in Figure 2.2a below.

CHRONOLOGY OF MECHANICAL ALLOYING

Aluminum–Titanium Alloys Introduced
Multiple Commercial Producers
INCOMAP Light Alloys Plant Commissioned
Wide Range of Mill Product Forms Available
Air Force Very High Temperature Aluminum Program
1990
Forged Airfoils
Development of MA Aluminum Lithium Alloys
First Commercial Use of MA 956
1980
Large Scale Ball Mills
MA Aluminum Pilot Plant
First Commercial use of MA 754
Reaction Milled Aluminum Described
Manufacturing Scale-up Nickel Base Alloys
First Al Alloy Patent Issued
First MA Patents Issued
MA Process Announced
1970
First MA Experiments on Aluminum
First MA Experiments on Nickel Alloys
Thoriated Nickel
1960
SAP Aluminum
1950
1910
Thoriated Tungsten

MA ALUMINUM

MA NICKEL

Figure 2.2a A Chronology of MA processes [64]

Notable developments include sintered aluminum product alloys in the 1950s that displayed outstanding elevated strength at high temperatures for high performance aircraft, thoria dispersed (TD) nickel in 1960 as a creep resistant high temperature material for combustion engines, TD Nichrome in 1965 with increased particle/matrix interfacial strength [65], traditional MA in 1967 to produce ODS nickel and iron superalloys for the aerospace and nuclear industries, reaction milled aluminum in the 1970s as an alternative approach to dispersion strengthening that produces Al_4C_3 with γ-Al_2O_3 dispersoids, and by 1985 multiple competitive, commercial MA producers.

The MA process involves creating an alloy via repeated cold welding, fracturing, and re-welding without melting by violently deforming and sintering mixtures of different powders in a way that uniformly introduces inert nano oxides into the alloy's microstructure. First, alloy materials are combined in a ball mill and ground to a fine powder. Any combination of elemental, pre-alloyed, and insoluble fine oxide powders can be combined. The powders are consolidated using hot isostatic pressing, forging, or slab rolling and extruded to produce a

bulk metal with an UFG microstructure. Heat treatments are then performed to activate recrystallization and remove existing internal stresses produced during cold compaction, either into a course columnar grain structure or a fine, equiaxed grain structure for superior strength. Commercial alloys often contain Cr and/or Al for corrosion and oxidation resistance and yttrium or titanium oxides for creep strength. Texture and grain aspect ratio must be optimized for maximum creep strength. Figure 2.2b below shows a schematic of the evolution of the powder solution during the ball milling process and Figure 2.2c shows the step-by-step process of MA.
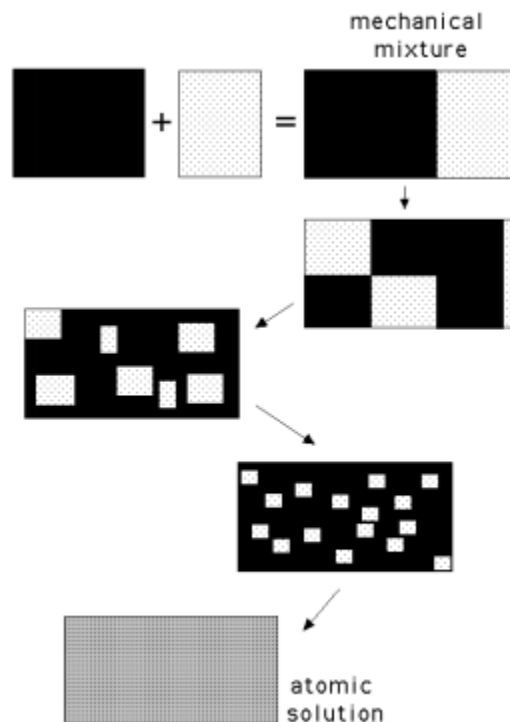
Figure 2.2b A schematic illustration of the evolution of a powder solution by progressive reduction in particle size during ball milling (H.K.D.H. Bhadeshia: http://www.msm.cam.ac.uk/phase-trans/mphil/MP4-4.pdf)
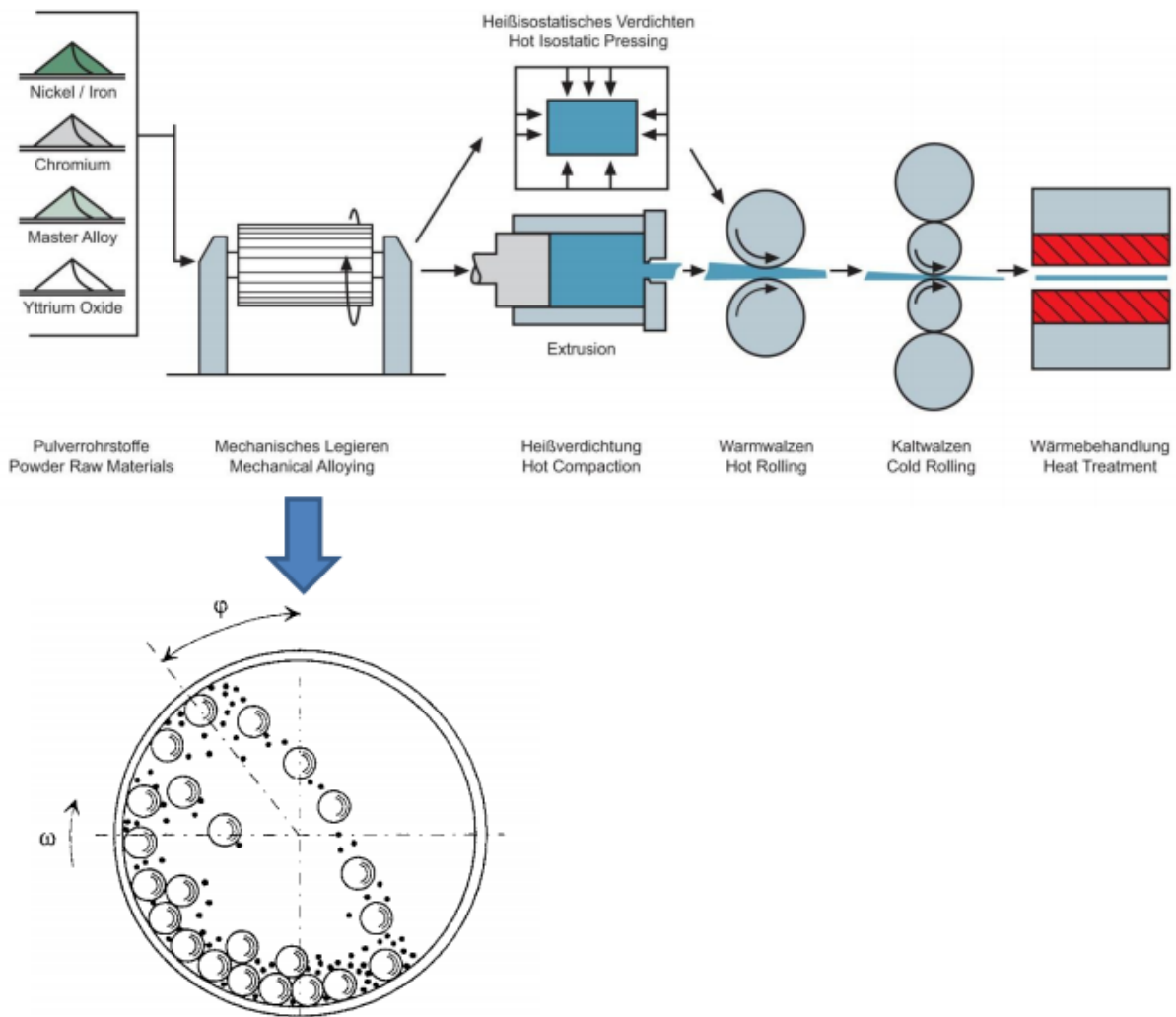
Figure 2.2c A step-by-step illustration of the MA process beginning with elemental, oxide, and raw pre-alloyed powders ball milled with rotation of the milling bowl velocity ω and angle of break ɸ. Next, the mixture is consolidated by hot isostatic pressing or hot compaction and extrusion, followed by hot rolling and cold rolling to produce a bulk alloy with UFG, and finally heat treatment to activate recrystallization and remove existing internal stresses produced during consolidation.

(http://www.netl.doe.gov/File%20Library/Events/2010/ods/Andy_Jones_Historical_perspective.pdf)

Complications arise in scaling up the production of MA materials because all processes involve the use of an energized ball mill. Academic research studies employ multi axis vigorously shaken canisters that produce only a few grams of material in a few hours. Subsequently, this has been scaled up to mechanically stirred mills that work with 100 lbs. of powder in 1-2 days. Eventually, commercial production shifted to gravity-assisted ball mills which increased production to 3000 lbs. in 50-150 hours of milling time. Limitations exist due to wear, vibration, structural integrity, heat extraction and product uniformity. The size of the powders must be controlled to avoid over-welding and seizing of the mill and over-fracturing and producing pyrophoric powder. Milling environments play a substantial role as well, and reducing environments and inert environments can be deployed in order to diminish some of these difficulties.

Processing difficulties remain due to the fact that each new alloy is a new R&D project. Predictability of fabrication and yield is often unachievable due to specialized and complex applications. In addition, precise control of final grain structures is difficult and non-reproducible. Joining MA materials has remained a constant challenge as welding has shown strength reduction, brazing, diffusion and explosion bonding have been explored, and friction stir welding may appear promising but is still being developed.

However, MA and ODS alloys have proved to be excellent across a variety of industrial applications spanning a broad class of materials summarized in Table 2.2a and Table 2.2b. These alloys are produced worldwide by various commercial suppliers as seen in Table 2.2c. In addition, many ODS ferritics have been successfully developed for nuclear applications in the form of swelling and creep resistant tubes for liquid salt cooled fast reactor fuel pins that trap α particles created by intense neutron radiation (DT 2906, DT 2203Y065, DT, DY, MA 957) and structural materials for next generation fusion reactors (ODS Eurofer 97).

Table 2.2a Selected MA Material Classes

Class of Material	Alloys
Light Alloys	Al-Mg-Li
ODS Alloys	FeCrAl + Y, rapidly solidified Al-Fe-Ce
Metal Matrix Composites	Al-SiC
Intermetallics	Cr3 Si, MoSi2 , NiTiAl
Cermets	Ni-TiC (reactive milling)
Metastable Systems	Fe-Zr, Co-Zr (amorphous/glassy)
Nano-crystalline Materials	Cu-Ta, Fe-Ta-W
Superconductors	Si-Pb (metallic), Ba-Ln-Cu (ceramic)
Super-corroding Alloys	Mg-Fe
Magnetic Materials	Fe-Nd-B

Table 2.2b MA ODS Alloy Applications

Industry Sector	Alloy Base	Component/Application
Aerospace/Military	Fe	Gas turbine combustor liners
		Fuel nozzle shrouds
	Ni	Turbine
		Compressor blades
		Nozzle guide valves
	Al	Low density aerospace forgings
		Spars
		Ribs
		Wing Tip Panels
		Compressor Vanes
		Torpedo Hulls
Automotive	Fe	Diesel fuel inlet atomiser
		Turbocharger scrolls
	Ni	Recombustors
	Al	Composite pistons
		Compressor rotors
		Vanes
		Impellors
Power Generation	Ni	Gas Turbine Compressor Blades
Tools/Heating Elements	Fe	Nozzles
		Stirrers
		Gobbers
		Insert Tubes
		Furnace Skid Rails
		Charge Carriers
		Creep/Fatigue Rig Test Bars
		Heating Element Wires

Table 2.2c ODS Alloy Commercial Suppliers

Location	Company
USA + UK	INCO Alloys
USA	Alcoa
	Dow Chemicals
	Howmett
USA + Norway	Exxon/Raufoss
Belgium	Dour Metal SA
Germany	Krebsoge
	Siemens AG
	Plansee GmbH
Japan	Kobe Steel
	Sumitomo Metal Ind.
	NRIM
	Showa

2.2.1 PM 2000 Steel

The PM 2000 ODS steel superalloy is manufactured by Metallwerk Plansee GmbH to be a highly oxidation resistant and extremely creep resistant ferritic iron-chromium based alloy. The full composition of PM 2000 by weight percent is given in Table 2.2.1a. A homogeneous distribution of nano sized Y_2O_3 particles in combination with recrystallized course grain structure allow it to remain strong at high temperatures up to 1300 ^{o}C and maintain creep strength up to 1350 ^{o}C. It forms a passive Al_2O_3 layer for corrosion resistance at high temperatures under oxidizing environments due to high amounts of Al and Cr that is highly resistant to high speed gas flows up to 1300 ^{o}C. PM 2000 is more resistant to coking and carburization than NiCr alloys, its components are lighter than those made from Ni, and it can be machined with normal tooling.

Typical fields of application for PM 2000 include: thermocouple sleeves for high temperatures, burner nozzles, charge carriers for high temperature furnace construction parts, pull rod assemblies for high temperature testing, stirrers for the glass industry, honeycomb structures for aerospace application, components for chemical plant construction, and combustion parts for engines. Since it is an ODS alloy it could be considered as a candidate for the structural material to be used in the future generation of high temperature gas cooled nuclear reactors as well as a replacement for tubing and structural components of existing generation three reactors, and as a structural material for future generation fusion plants.

Table 2.2.1a Nominal Composition of PM 2000

	Fe	Cr	Al	Ti	C	Y_2O_3
PM 2000	74.45	19	5.5	0.5	0.05	0.5

(http://www.matweb.com/search/datasheet.aspx?matguid=21e9ec9a0de24b47bcf69ab1 1c375567&ckck=1)

Chemical, physical, as well as known mechanical properties of PM 2000 at RT are displayed in Table 2.2.1b.

Table 2.2.1b Nominal Properties of Bulk PM 2000

Density	7.18 g/cm^3
Melting Point	1756 K
Thermal Conductivity	10.9 W/mK
Bulk Tensile Strength	525 MPa
Young's Modulus	157-173 GPa
Hardness	2.844 GPa
Lattice Type	Body-centered cubic (bcc)

(http://www.matweb.com/search/datasheet.aspx?matguid=21e9ec9a0de24b47bcf69ab1 1c375567&ckck=1)

2.3 Methods of Severe Plastic Deformation

In order to produce nanostructured materials, a top-down approach can be employed, where existing coarse grained materials are processed to produce substantial grain refinement until a nanostructure is achieved. The most successful of these approaches involve severe plastic deformation (SPD), subjecting materials to very large strains while they remain constrained to a fixed cross-sectional dimension. Materials produced by SPD normally have grain sizes between 100 nm and 1 µm, but they often also contain subgrains, dislocation cells, and x-ray diffraction coherency smaller than 100 nm [66]. Thus, they are given the name ultra fine grained materials. The nanostructure term refers to the nano-scale oxide precipitates preventing grain growth and providing creep strength.

A number of SPD techniques are now available, including Equal Channel Angular Pressing (ECAP) [17, 67], high pressure torsion (HPT) [66, 68], accumulative roll bonding (ARB) [69, 70], repetitive corrugation and straightening [71, 72], and friction stir processing (FSP) [73, 74]. Some combinations of these procedures have also been attempted including ECAP with cold rolling [75], ARB and FSP [76], and ECAP and HPT [77, 78].

ECAP has become the front runner due to its commercially viable processing route and favorable microstructures produced. ECAP can be scaled to produce large samples and performed in conventional rolling mills for continuous processing [39-41]. Thus, it is already cost competitive for 5-20 mm diameter bars at $50-$150 per kg and it has potential to be cost competitive for high volume samples. ECAP was used to produce the copper fatigue specimen studied in the present work.

HPT has an added capability of consolidating powders directly without a heat treatment step. Therefore, it was chosen for the production of the Cu-Nb nano composites. It was also combined with MA to produce an HPT PM 2000 fatigue specimen for this work.

2.3.1 Equal Channel Angular Pressing

The concept of using pure shear for ideal forming, extrusion and drawing of materials was first theorized by Richmond and Devenpeck modelling billets and products as rectangular strips [79]. Soon after, attempts were made to try to investigate simple shear deformation experimentally, but they were limited to rather small volumes and only successful during deformation initiation [80, 81]. Concurrently, new methods of using cold-working to produce specific textures in materials were being developed [82].

In efforts to transform shear theory and materials shear testing on limited volume into a large scale materials synthesis, processing, and production technique, ECAP was invented in the Soviet Union in 1973 and patented in 1977 by V.M. Segal [83]. A schematic of the SPD process can be seen in Figure 2.3.1a.
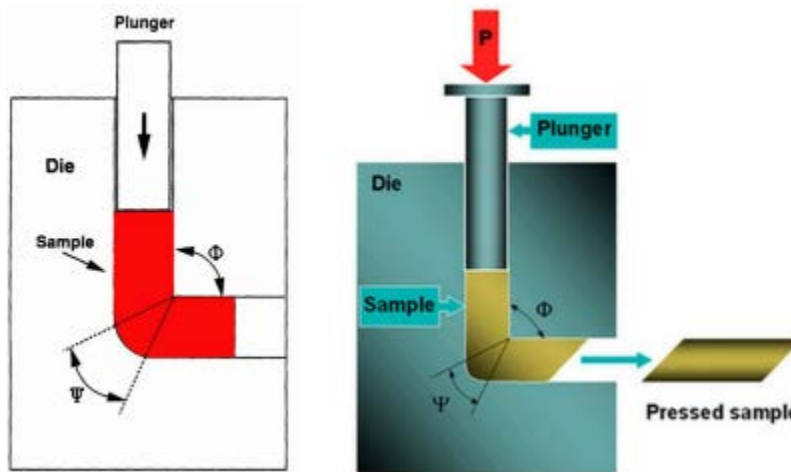
Figure 2.3.1a The principle of ECAP. The internal channel in the die is bent through a channel-intersection angle, φ. The angle Ψ represents the arc of curvature, bend angle, where the entrance and exit channels intersect. A rod or bar is machined to fit tightly inside the channel and pressed through the die using a plunger with force P shown on the right. (http://neel.cnrs.fr/spip.php?article2816&lang=fr)

Simple shear occurs as the billet passes through the die while a fixed cross-sectional area is retained. Deformation passes may be repeated any number of times to produce a final

pressed sample that underwent a very large strain. Between two adjacent passes, it is also possible to rotate the billet along its longitudinal axis and create multiple deformation routes that will change grain refinement and shape. There are four common rotation routes illustrated in Figure 2.3.1b.
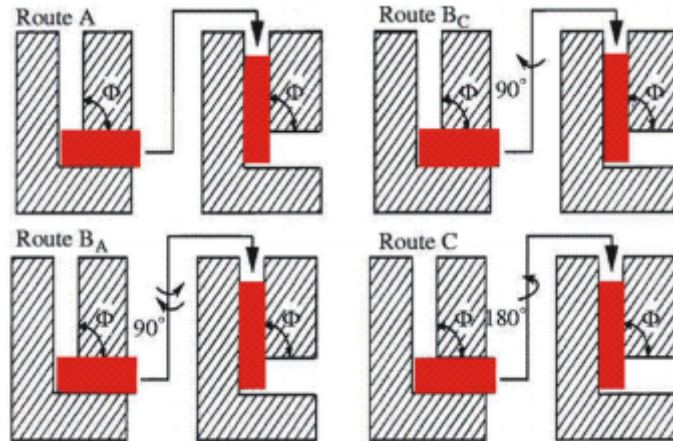
Figure 2.3.1b Four common rotation routes for repetitive pressing via ECAP. In Route A, the billet is not rotated, in Route B_A the billet is rotated 90º clockwise and counterclockwise alternatively, in Route B_C the billet is always rotated 90º clockwise, and in Route C the billet is rotated 180º in between deformation passes [84].

The channel-intersection angle, ɸ, also significantly affects microstructural development because it determines the shear strain from an individual deformation pass. ɸ values between 90º and 157.5º have been investigated [85, 86]. The shear strain for an individual pass is given by

$$\gamma = 2 \cot(\frac{\varphi}{2}) \tag{2.1}$$

Smaller channel-intersection angles will result in higher shear strains from each pass and thus have the most effectiveness for grain refinement [86]. The copper fatigue sample in this report produced via ECAP underwent 8 deformation passes following route B_C and was deformed with a channel-intersection of ɸ = 90º.

2.3.2 High Pressure Torsion

HPT arose out of the work of P.W Bridgeman at Harvard University who won the Nobel Prize in Physics in 1946 for high pressure physics. He was able to modify his pressure apparatus by overriding safety controls to create pressures exceeding 10 GPa, vastly surpassing previous machinery limited to 300 MPa. His interests in plastic flow deformation under high pressure eventually led him to realize that by combining torsion and compression on thin discs, he could demonstrate many effects of intensive plastic strain on various materials [87]. A schematic of the HPT process can be seen in Figure 2.3.2a.
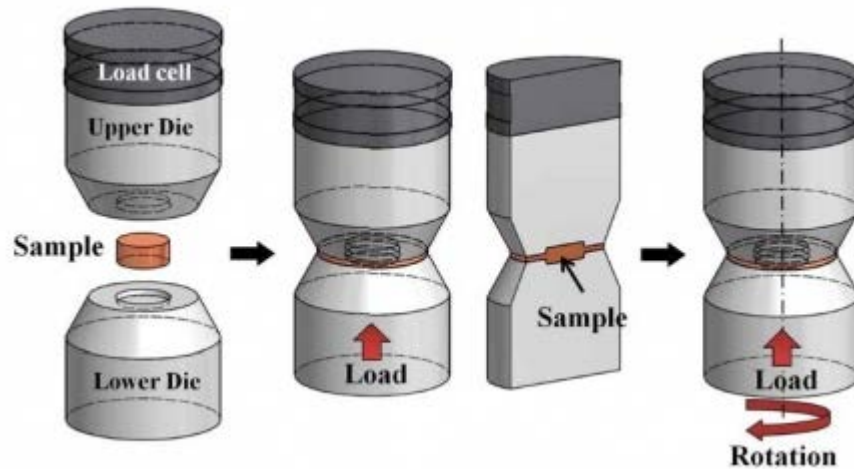
Figure 2.3.2a Schematic illustration of an HPT device (www.koreascholar.co.kr)

There exist three modes of HPT based on the level of constraint of the disk as it is compressed and turned: unconstrained, constrained, and quasi-constrained. A depiction of these three HPT modes can be seen in Figure 2.3.2b. In unconstrained mode, the disc sample is allowed to freely expand as it is compressed, in constrained mode the anvils are machined so that the bottom anvil holding the disc provides a barrier for outflow while the top anvil compresses only onto the disc, and in quasi-constrained mode both anvils have matching cavities for the disc sample to hold it in place but allow outflow through the small center gap.
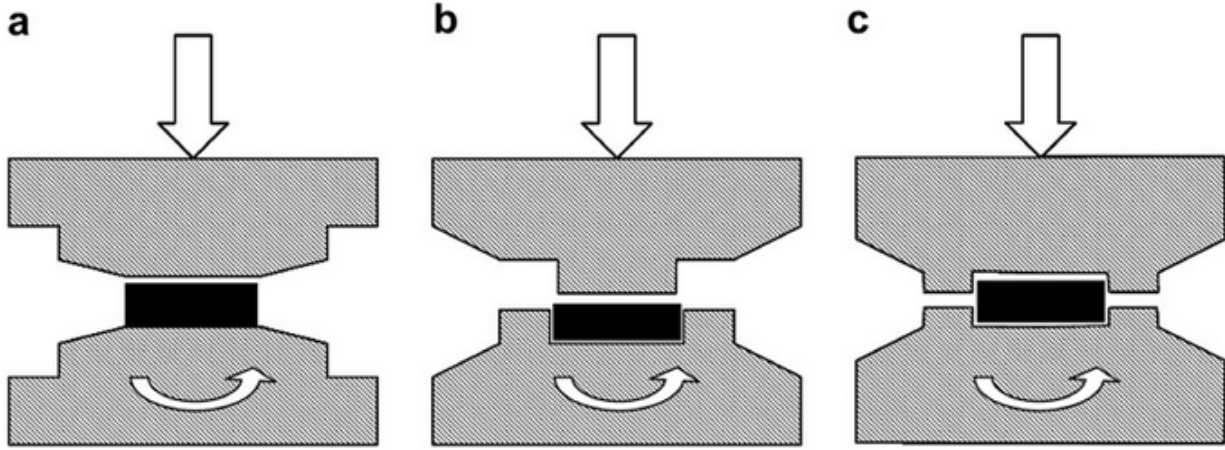
Figure 2.3.2b HPT disk fabrication by: (a) unconstrained mode, (b) constrained mode, and (c) quasi-constrained mode. [68]

Properties of the deformed material depend on the pressure applied and number of revolutions, but it is generally noted that forces at or above 5 GPa and more than 5 rotations produce reasonably homogeneous microstructures throughout the sample with grain sizes less than or equal to 100 nm [17, 88]. The shear strain is given by

$$\gamma = \frac{2 \pi N r}{h} \tag{2.2}$$

where N is the number of turns, r is the radial distance from the center of the disc, and h is the final thickness of the disc. The cumulative strain can be estimated as follows:

$$\varepsilon = \ln\left(\frac{2 \pi N r}{h}\right) \tag{2.3}$$

where h_o is the initial thickness of the disc [89]. It can be seen that no shear strain is induced in the center of the disc, so no hardening will occur here. The highest shear strains will occur at the edges of the sample. It is also presumed that the dislocation density will be higher at the edges of the disc than at the center since this is related to the microstrain by

$$\rho = \frac{2 \sqrt{3} \, \varepsilon}{d_c \, b} \tag{2.4}$$

where b is the magnitude of the Burgers vector, d_c is the cell size, and ε is the cumulative micro strain. Higher compressive forces lead to higher hardness levels and more homogeneous microstructures that span the radius of the disc. In addition, a greater number of turns leads to a higher hardness and more homogeneous hardness across the

radius of the disk. For materials with a fast recovery rate, hardness values will be larger at the center of the disc, but for materials with a slow recovery rate hardness values will be lower at the center of the disc for early stages of HPT prior to the formation of a homogeneous structure. This is shown in the drawing of Figure 2.3.2c.
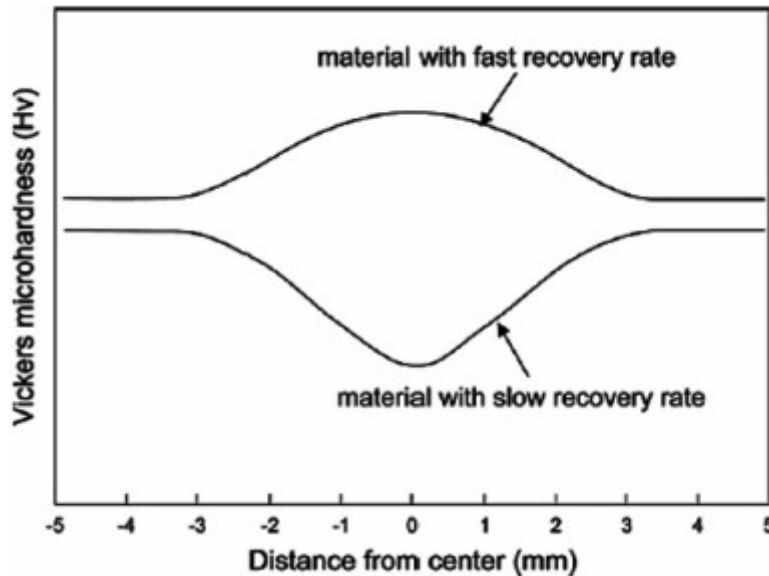
Figure 2.3.2c A depiction of the radial hardness across an HPT disc for materials with slow and fast recovery rates at low total strains [90]

Because every material has steady-state properties, there is a limit to the amount of grain refinement and hardening each material can undergo under HPT. There will be a number of turns where each material becomes saturated and will no longer change when undergoing further HPT [90]. HPT has been performed on metal matrix composites successfully with grain size reduction, down to as low as 10-50 nm for Cu-Fe composites, with homogeneous distributions [89], so it is expected for the HPT deformed samples discussed in this report, PM 2000 steel and Cu-Nb to behave in a similar manner.

2.4 Microhardness

The hardness value of materials is an economical, non-destructive testing method of bulk materials that can employ lightweight and even sometimes portable equipment. Because hardness values often have a linear correlation with bulk tensile strength [91], they are an important parameter for studying a material's mechanical properties due to its simple deployment. Microhardness values can be determined by various methods, but the two most commonly used, Vickers and Brinell, can be applied with heavier loads as macroindentation tests as well. In this report, microhardness values were measured by Vickers hardness tests.

Vickers testing is convenient because calculations are independent of the size of the indenter and the indenter can be used on any metallic material. A square-based, diamond pyramid with an opening angle of 136° is used as the indenter tip. Indents should be performed between 200 and 1000 grams force and sample thicknesses should be at least 2.5 times larger than the indent diameter, or roughly h > d/7, where h is the sample thickness and d is the average length of the diagonals of the indent. Distances between indents should be at least three times the average length of the diagonals of an indent, and the distance between the sample edge and center of the closest indent should be 2.5 times larger than the average length of the diagonals of the indent according to standard ISO 6507-1 for the materials investigated in this report.

After this tip punctures the sample surface, the HV number is given by the ratio of applied force in kilogram-force to sample surface area in square millimeters. By using the diagonals of the indent, d_1 and d_2, to determine the surface area, the following equation arrives for Vickers hardness in terms of kgf/mm^2:

$$HV = \frac{8 \sin(68^o)\, F}{(d_1 + d_2)^2} \qquad (2.5)$$

To calculate Vickers hardness using SI units, this value is then multiplied by the standard gravitational constant, g = 9.80665, to convert the force applied to Newtons. This can

further be divided by 1000 to yield a value in GPa. The simplified approximate equation for HV in GPa can be given as:

$$HV \approx \frac{0.1891\,F}{\left(\frac{d_1 + d_2}{2}\right)^2} \tag{2.6}$$

Microhardness measurements across HPT disc specimens provide insight into the deformation process by correlating hardness to degree of deformation.

2.5 Fatigue

Fatigue failure occurs in materials subjected to dynamic and fluctuating, cyclic stresses. Due to these circumstances, materials can fail at stresses lower than their static yield stresses after a lengthy amount of cycling. This type of mechanical failure occurs in over 80 percent of all engineering components in service, whether that be due to cyclic plasticity, a combination of cyclic stress and chemical attack, thermal creep fatigue at elevated temperatures, or contact fatigue involving sliding, fretting, or rolling [118]. What makes this type of failure even more detrimental is the fact that it occurs catastrophically and suddenly without warning. The failure itself mocks that of brittle failure in that there is little gross plastic deformation associated with the failure. However, the driving force leading up to the failure is initiated by cracks forming in areas of high stress concentrations or on material surfaces and these cracks advancing incrementally in a direction roughly perpendicular to the main tensile axis during each stress cycle. Ultimately, the cross-sectional area of the component is reduced to the point where it is no longer load bearing and failure occurs in tension instantly.

2.5.1 Early Beginnings

Fatigue research has an early history, beginning in 1837 with Willhelm Albert constructing a test machine for conveyer chains that had failed in service in the mines in Clausthal [92].

Two years later, Jean-Victor Poncelet was describing metals as tired in his lectures in Metz. In 1842, Rankine published "On the causes of the unexpected breakage of the journals of railway axles, and on the means of preventing such accidents by observing the law of continuity in their construction," suggesting a crack growth mechanism through repeated stressing [93]. Coincidentally, during the same year the catastrophic Versailles train crash occurred due to fatigue failure in an axle, leading to efforts centered on fatigue in railway axles for the remainder of the next few decades. This culminated with funding from the British Parliament to Eaton Hodgkinson to perform experiments on the cyclic loading of iron in 1849 and Morin's book *Resistance des Materiaux* in 1853 prescribing safe life design approaches to axles [94]. A year later, Braithwaite and his colleague "Mr. Field" coin the term fatigue in an 1854 paper on common service fatigue failures [95].

August Wöhler was the first to perform systematic fatigue testing and calibrate forces based on deflections, relating the largest deflection to bending and torsional stresses and ultimately suggesting design for a finite fatigue life [96, 97]. In 1870, Wöhler's laws reported that a material can be induced to fail by many repetitions of stresses, all of which are lower than the static yield stress. Also, they remarked that the higher the maximum stress, the lower the number of cycles that lead to failure, and that the stress amplitude plays a key role in the failure of the material. His conclusions were to implement two safety factors: one an allowable ratio between the maximum stress in service and the static yield stress (2:1), and one for an allowable stress amplitude (2:1). Wöhler highlights the effects of crack growth and propagation for the first time as well. [98-100]. He is most well known for being credited with the S-N curve, termed Wöhler curve beginning in 1936 [101], plotted by his successor Spangenberg.

At the turn of the 20th century, Sir James Alfred Ewing demonstrated that fatigue originated in microscopic cracks [102] and Bauschinger had hypothesized that yield stresses are lowered on reversal of strain during cyclic loading [103-105]. In 1910, O.H. Basquin suggested a log-log relationship between stress and number of cycles to failure for this high cycle, finite life region of the Wöhler curve. Finally, all of this work was summarized in the first book dedicated entirely to fatigue in 1924 by Gough [106]. At this point in the 20th

century, extensive global fatigue research was being performed in Germany, the US, and the UK that would shape our modern understanding.

2.5.2 Cyclic Stresses

Fatigue of components in service occurs as one of three or some combination of three applied stress states: axial, tension and compression; flexural, bending; and torsional, twisting. There are also three possible fluctuating stress-times modes: reversed, repeated, and random. These are shown and described in Figure 2.5.2a. Some useful parameters for characterizing a stress cycle in terms of its minimum and maximum stresses, σ_{min} and σ_{max}, are the mean stress

$$\sigma_m = \frac{\sigma_{max} + \sigma_{min}}{2} \tag{2.7}$$

range of stress

$$\sigma_r = \sigma_{max} - \sigma_{min} \tag{2.8}$$

stress amplitude

$$\sigma_a = \frac{\sigma_{max} + \sigma_{min}}{2} \tag{2.9}$$

stress ratio

$$R = \frac{\sigma_{min}}{\sigma_{max}} \tag{2.10}$$

and amplitude ratio

$$A = \frac{\sigma_a}{\sigma_m} = \frac{1 - R}{1 + R} \tag{2.11}$$

Conventionally, compressive stresses are negative and tensile stresses are positive. All fatigue tests performed were done in a bending stress state with sinusoidal reversed cycles with an approximate strain ratio of R = -1. The tests were displacement controlled, so it is more appropriate to replace stress parameters with strain parameters.
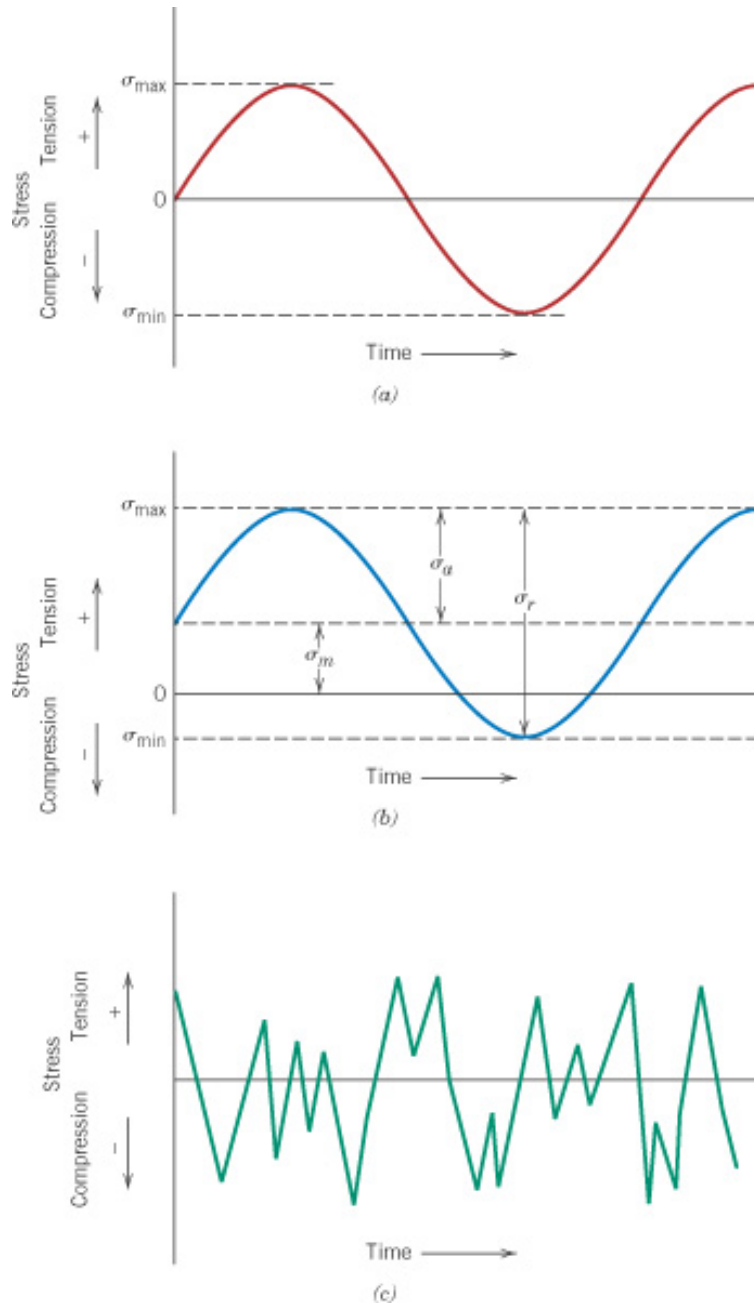
Figure 2.5.2a Stress-time cycle modes. (a) A reversed stress cycle where the amplitude is symmetric about a mean zero stress level, alternating between maximum tensile and compressive stresses of equal magnitude. (b) A repeated stress cycle, where the maximum tensile and compressive stresses are asymmetrical with respect to the zero stress level. (c) A random stress cycle where there is no order to the amplitude or frequency of stress. (Materials Science and Engineering: An Introduction, William D. Callister Jr. p. 407)

2.5.3 The S-N Curve

In traditional large scale fatigue tests, a test apparatus designed to duplicate the service stress conditions is used to subject test specimens to load-controlled cycling at maximum stresses up to 2/3 of the yield stress and the number of cycles is counted until failure. Following the convention of Wöhler and Spangenberg, the data is then plotted as stress, S, versus the number of cycles to failure, N. There are two characteristic material responses as shown in Figure 2.5.3a of an example S-N curve. The S value plotted may be σ_{max}, σ_{min}, or σ_a. In the first case, mostly for ferrous and titanium alloys, the S-N curve becomes horizontal at high N values. This means there is a limiting stress level, the fatigue limit, below which fatigue failure will not occur, presumably for an infinite number of cycles. This limit is approximately 0.35 to 0.6 σ_y, the static yield strength, for most steels, and is highly dependent on surface conditions, residual stresses, and inclusions that serve as stress concentrators. An infinite life design where the material is always held at stress levels below its fatigue limit can be employed in cases where it cannot be inspected. In the second case, for non-ferrous alloys, there is no fatigue limit. The fatigue strength of these materials is defined as the stress level at which failure will occur for a specified number of cycles. The fatigue life, N_f, of both materials is defined as the number of cycles to failure at a specified stress level. A significant number of tests should be performed to reduce scatter to an acceptable level.
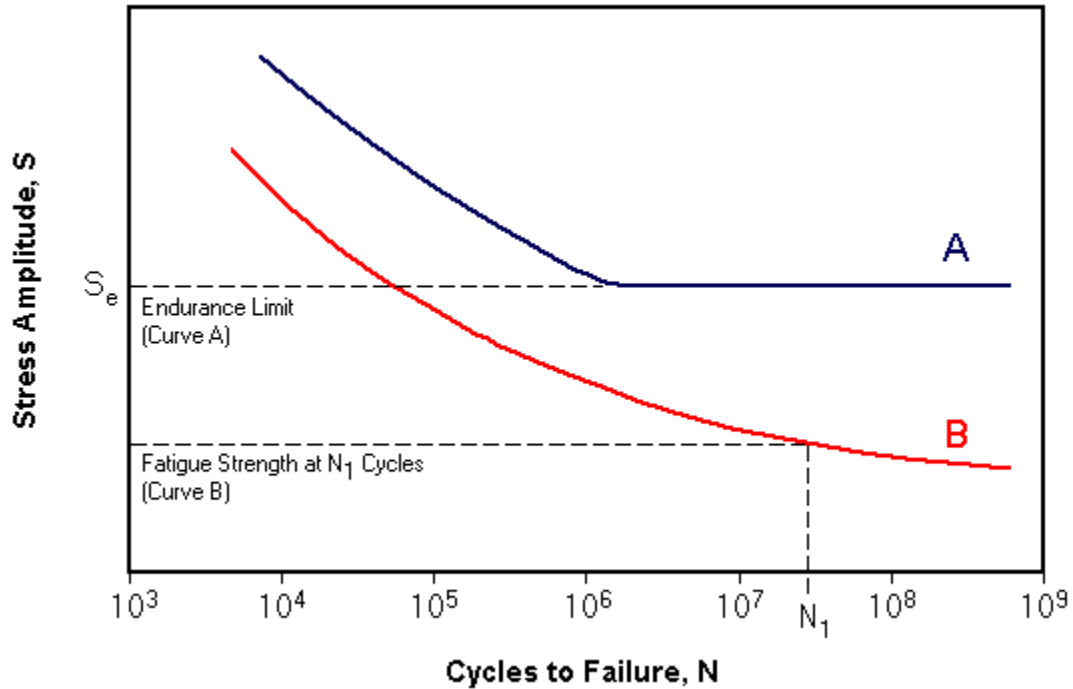
Figure 2.5.3a Representative S-N curves for (a) a material with a fatigue limit and (b) a material with no fatigue limit.

(http://www.feaoptimization.com/ETBX/stresslife_help.html)

2.5.4 High Cycle Fatigue

For cycles with lower stress/strain levels where deformation is completely elastic, longer fatigue lives occur and this regime is termed high cycle fatigue. Relatively large numbers of cycles, greater than about 10^4 are required to produce failure. For non-ferrous metals, this number can be as large as 10^9 cycles. Plastic deformation only occurs at the crack tip after cracks form. The data for high-cycle fatigue is expressed as a S-N curve. This curve is then plotted on a log scale to determine a relationship between σ_m, R, or A versus number of cycles to failure. Normally in this regime, fatigue strength increases as static yield strength of the material increases. However, with increased σ_y comes decreased fracture toughness and increased environmental sensitivity, therefore often times it is not advised to use the strongest steel available. For high cycle fatigue where the deformation is completely elastic, the S-N curve can be modelled by the Basquin equation

$$\sigma_a = \sigma'_f (2N)^b \ (stress) \qquad\qquad \varepsilon_{a\,el} = \frac{\sigma'_f}{E}(2N)^b \ (strain) \qquad\qquad (2.12)$$

where σ_a is the stress amplitude, $\varepsilon_{a\,el}$ is the elastic strain amplitude, σ'_f is the fatigue strength coefficient defined as the stress intercept at 2N = 1, 2N is the number of reversals to failure, and b is the fatigue strength exponent, which varies between -0.05 and -0.12 for most metals. σ'_f is often approximately equal to the true tensile fracture stress of a metal. A smaller b results in a longer fatigue life. High cycle fatigue life is normally increased by selecting materials with a higher UTS, or by performing compressive surface stressing via shot peening or nitriding. (see Section 2.5.10)

2.5.5 Low Cycle Fatigue

Low cycle fatigue is associated with relatively high loads/strains that produce elastic and plastic strain during each cycle, making fatigue lives much shorter, less than 10^4 cycles. The elastic loading and unloading portion of each cycle falls under equation (2.12) where the stress and strain are directly linked through the elastic modulus. However, because there is also plastic deformation, each cycle forms a hysteresis loop shown in Figure 2.5.5a. From point O to A the component is in tension, unloading occurs from A to D, and at D the component is under no stress. Then, from D to B the component is being compressed, from B to C this compressive stress is unloaded, and again at C the component is under no stress. When the component is again loaded under tension, the strain profile moves from C to A. A and B represent the cyclic stress and strain maximum and minimum values for the cycle and are termed the cyclic stress and strain limits. The total strain can be expressed in terms of elastic and plastic components as

$$\varepsilon = \varepsilon_{el} + \varepsilon_{pl} \qquad\qquad\qquad (2.13)$$

The elastic component can be expressed as σ/E. The plastic strain is the width of the loop at its center, or CD, as shown in Figure 2.2.5a. The area of this loop is the energy dissipated in one cycle of fatiguing. The tests performed for this report were cyclic strain-controlled fatigue, where the strain amplitude was held constant. Because plastic deformation is not completely reversible, these hysteresis loops can change with cycle number depending on

the initial condition of the material. The material can either undergo cyclic softening, cyclic hardening, or remain stable. Hardening and softening are shown in Figure 2.2.5b.
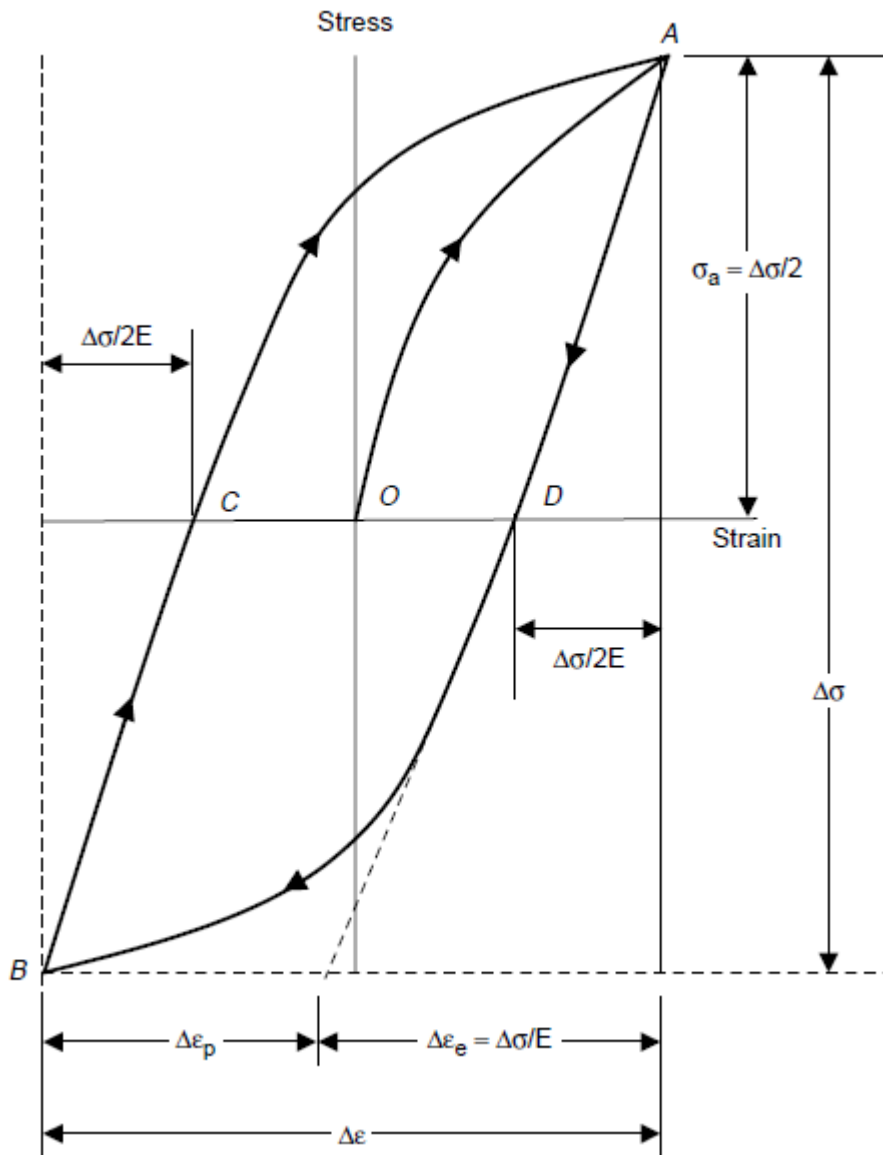
Figure2.5.5a A stress-strain hysteresis loop for a load cycle in the low cycle fatigue regime (http://www.asminternational.org/documents/10192/1849770/05224G_Chapter14.pdf)

Stress
Response

σ

Time

Constant Applied
Strain Amplitude

ε

Time

5000
3000
1

σ

ε

2
4

Cyclic Stress-Strain
Response

Cyclic Hardening

Stress
Response

σ

Time

Constant Applied
Strain Amplitude

ε

Time

1
3000
5000

σ

ε

Cyclic Stress-Strain
Response

4
2
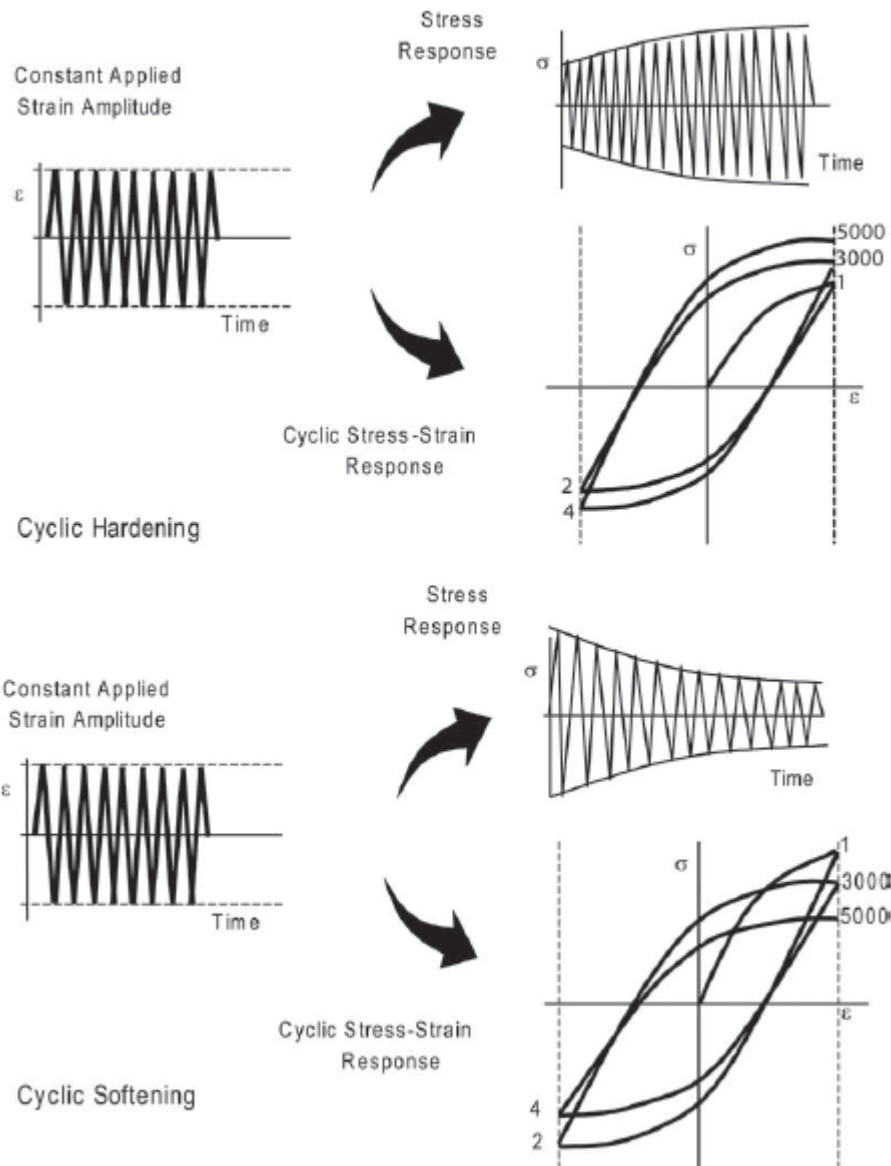
Cyclic Softening

Figure 2.5.5b Cyclic hardening and cyclic softening during constant strain amplitude low cycle fatigue

(http://www.asminternational.org/documents/10192/1849770/05224G_Chapter14.pdf)

Cyclic hardening leads to increased peak stress with increasing cycles, while cyclic softening leads to decreased peak stress with increasing cycles. Strong metals tend to soften while low-strength metals tend to harden. A rule of thumb is that metals will harden if $\sigma_{UTS}/\sigma_y \geq 1.4$ and soften if $\sigma_{UTS}/\sigma_y \leq 1.2$. These responses are also highly dependent upon the metal's pre-

existing dislocation microstructure. If the material has been intensively cold worked by SPD, its initial dislocation density is very high, so cyclic strain will allow these dislocations to rearrange into more stable configurations, reducing the stress required to initiate plastic deformation. Concurrently, if the initial dislocation density is low, cyclic strain will increase it and thus harden the material.

Low-cycle fatigue data is often presented as ε_{pl} versus N_f on a log-log scale for strain-amplitude controlled tests. The Coffin-Manson relation is used to model this behavior

$$\varepsilon_{pl} = \varepsilon'_f (2N)^c \tag{2.14}$$

where ε_{pl} is the plastic strain amplitude, ε'_f is the fatigue ductility coefficient defined by the strain intercept at 2N = 1, 2N is the number of reversals to failure, and c is the fatigue ductility exponent that varies between -0.5 and -0.8. Often times ε'_f is approximately equal to the true tensile fracture strain of the metal. A smaller c results in a longer fatigue life.

2.5.6 The Bauschinger Effect

When the specimen undergoes plastic deformation during low cycle fatigue testing, the Bauschinger effect may occur. Since Bauschinger had been performing experiments with multiple load reversals with both tensile and compressive stresses in 1886, he noticed that the elastic limit of metals changed after repeated stress cycles [103-105]. After the metal is loaded in tension to beyond its yield stress to a point σ_{max} and then unloaded through the zero stress level and loaded into compression to a point -σ_{max}, it yields this time before at a stress level magnitude less than its initial yield stress, -σ$_y$. Masing proposed that this new yield occurs at $\sigma'_y = \sigma_{max} - 2\sigma_y$. This can be seen in Figure 2.5.6a. This stress decrease occurs regardless of which stress state comes first: tension or compression.
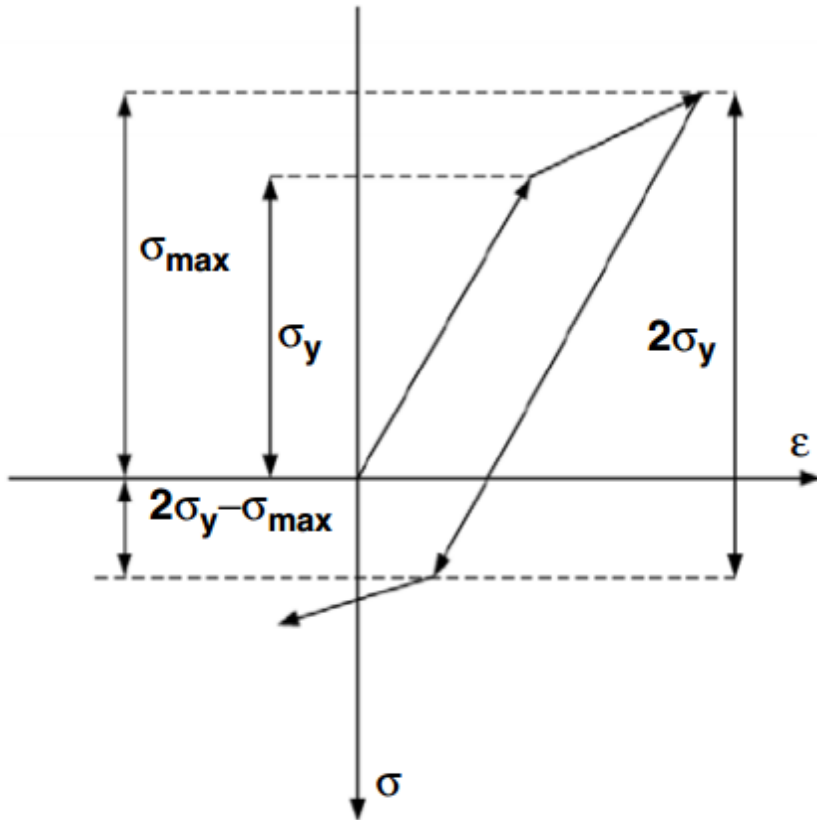
Figure 2.5.6b An illustration of the Bauschinger effect, showing that when a material is reverse loaded to beyond its initial yield point, this second yield point occurs at a lower stress magnitude. [120]

2.5.7 The Strain-Life Curve

In order to obtain a full description of the complete fatigue process and estimate the entire range of fatigue lives, elastic and plastic strains induced by fatigue are combined into total strain by combining the models of Basquin and Coffin and Mason by the following:

$$\varepsilon = \frac{\sigma'_f}{E}(2N)^b + \varepsilon'_f(2N)^c \tag{2.15}$$

All data can be plotted together in a strain-life curve, where large strain amplitudes tend toward the plastic model and small strain amplitudes tend toward the elastic model. An illustration of the strain life curve can be seen in Figure 2.5.7a.
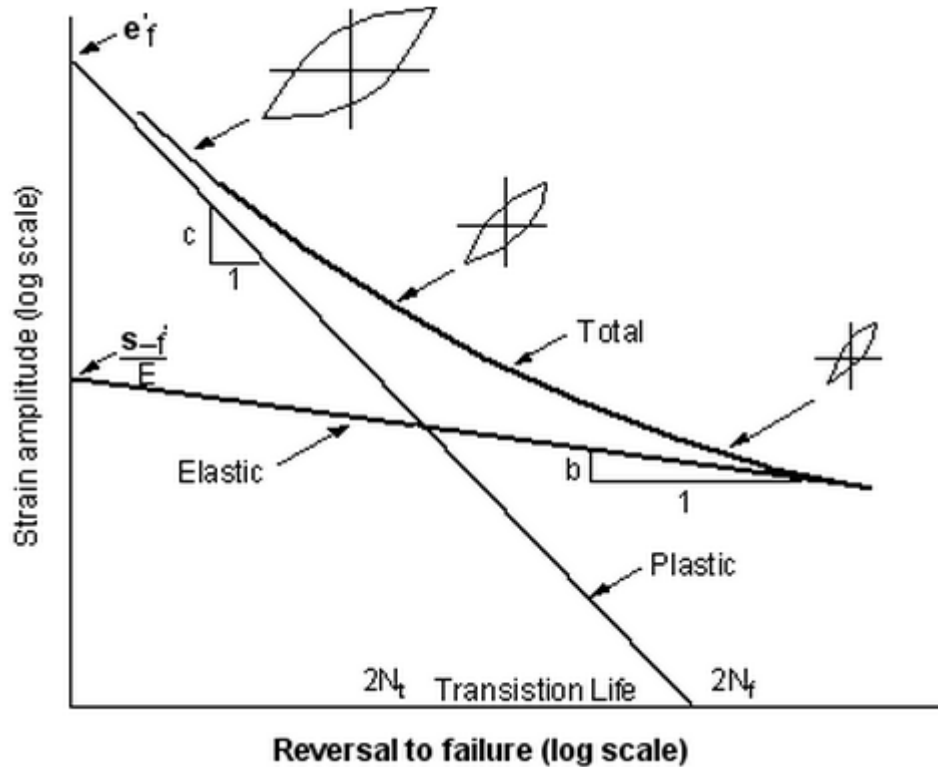
Figure 2.5.7a The Total Strain-Life Curve with plastic, transition and elastic regimes (R. W. Landgraf, in *ASTM STP* 467 p. 3.)

At the point where the elastic and plastic life curves intersect, the transition life is obtained. This represents a point where stable hysteresis loops have equal elastic and plastic components. At fatigue lives, cycles to failure, less than this intersection, plasticity dominates fatigue life, but at fatigue lives greater than this intersection elasticity dominates fatigue life. Safe-life design is normally implemented for materials subjected to plastic strains where the material has a finite lifetime to develop a critical crack size and is taken out of service when a crack forms.

2.5.8 The Cyclic Stress-Strain Curve

During strain controlled fatigue testing early on in a specimen's fatigue life, after a relatively low number of cycles, no more than about 10% of that metal's total fatigue life, stable hysteresis loops occur. Stress amplitudes remain reasonably constant for each controlled strain amplitude. The cyclic stress-strain curve is obtained by plotting the stress-strain coordinates from the tips of stable hysteresis loops of differing strain amplitudes and drawing a locus line through them. An example cyclic stress strain curve is shown in Figure 2.5.8a.
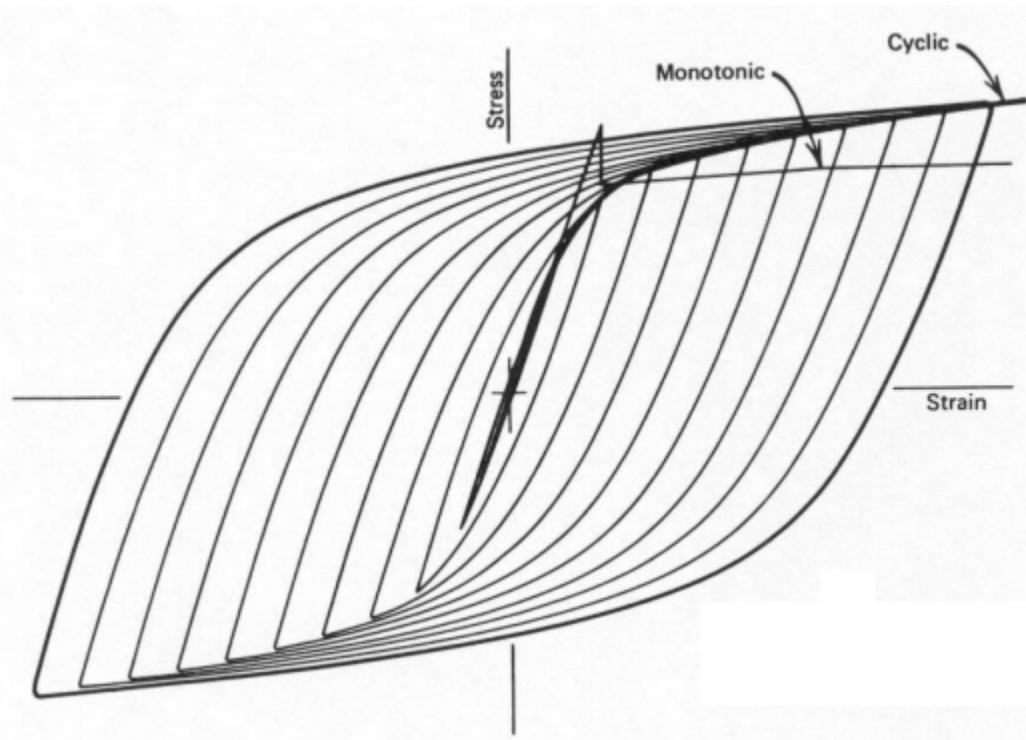
Figure 2.5.8a Cyclic Stress-Strain Curve constructed by connecting the tips of several stable hysteresis loops with various strain amplitudes
(https://www.efatigue.com/training/Chapter_5.pdf)

This cyclic stress-strain curve can be compared directly to a monotonic stress-strain curve obtained by a compression, tension, or bending test for direct comparison. When a material cyclically softens, yield strength is below the yield during a monotonic test. In the reverse case, cyclic hardening occurs. Mixed mode behavior may occur, where cyclic hardening precedes cyclic softening or vice versa. Finally, cyclically stable metals will trace their monotonic stress-strain curves. The four modes are shown in Figure 2.5.8b.
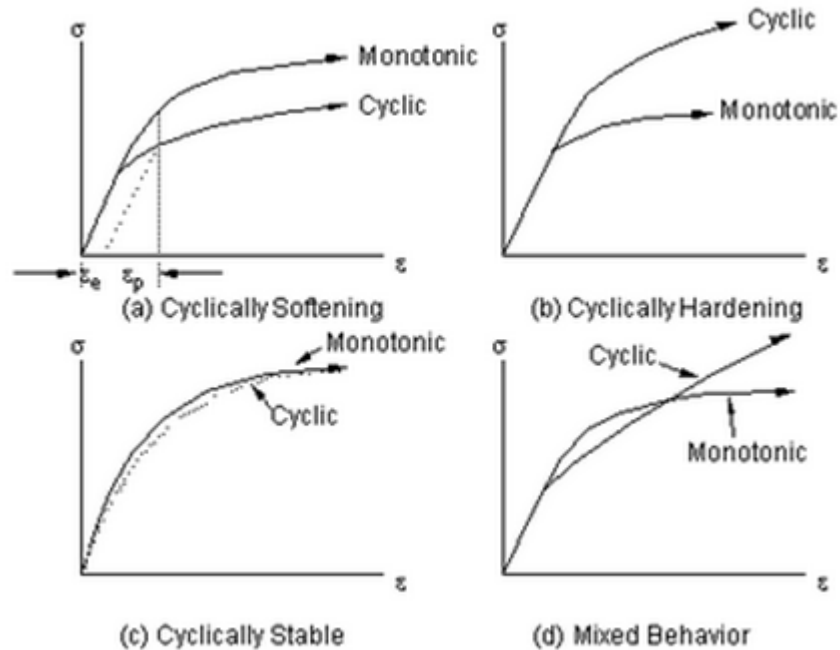
Figure 2.5.8b A comparison between cyclic and monotonic stress-strain curves and the four modes that may result: (a) cyclic softening, (b) cyclic hardening, (c) cyclic stability, and (d) mixed mode behavior

2.5.9 Crack Initiation and Propagation

Fatigue cracks begin at free surfaces due to external surface defects and discontinuities caused by surface roughness or in internal areas of high stress concentration caused by defects. Even if there are no surface defects before fatiguing, persistent slip bands (PSB) will build up as a combination of fine slip movements on the order of 1 nm joining together. Plastic strains within these PSBs can be 100 times greater than in the surrounding material. Fatigue testing causes back and forth movement of these PSBs forming intrusions and extrusions at the surface, eventually producing a crack. This development can be seen in Figure 2.5.9a.
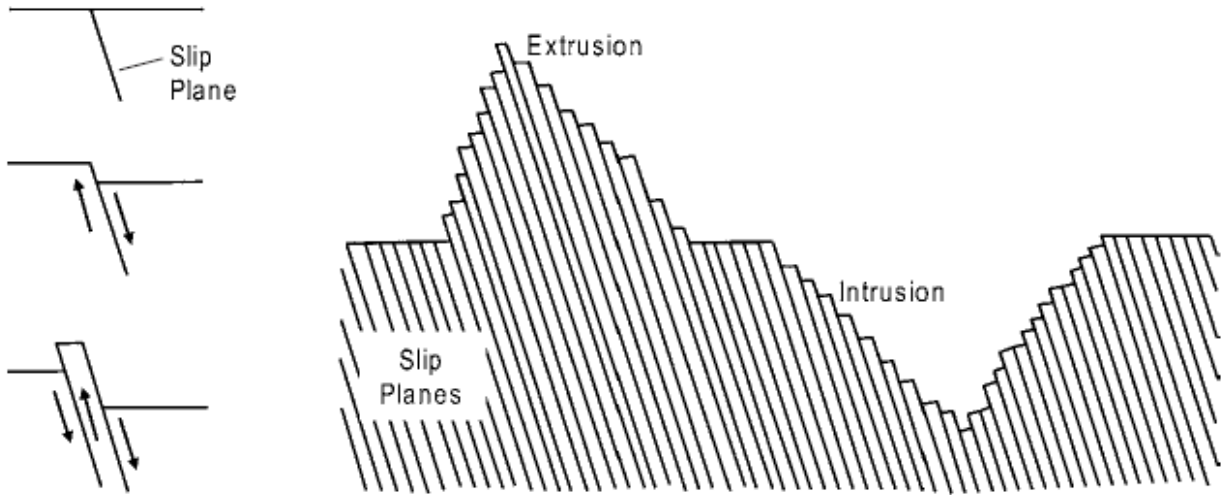
Figure 2.5.9a Development of cracks due to the formation of intrusions and extrusions on the sample surface caused by the back and forth movement of slip planes (http://www.asminternational.org/documents/10192/1849770/05224G_Chapter14.pdf)

Initially, the crack will propagate parallel to these slip bands at an angle about 45° to the principle stress direction at a very slow rate on the order of 1 nm per cycle, leaving behind a featureless fracture surface. Eventually the crack becomes long enough so that the stress field at its tip dominates. This causes the movement of the crack to shift directions and head perpendicular to the principal stress.

Stage II begins with the crack moving perpendicular to the principal stress in a way that continually sharpens and blunts the crack as it grows as shown below in Figure 2.5.9b. Often times, this crack propagation will form microscopic striations, with each striation representing one fatigue cycle, Figure 2.5.9c. However, macroscopically fatigue will appear as concentric "clamshell" beach marks, Figure 2.5.9d, if stress changes such as starting and stopping occurred during fatigue life. Therefore, each of the beach marks could contain a very large number of cycles. Crack growth rate accelerates as the fracture toughness of the material is reached and ends with catastrophic tensile overload failure when the crack is long enough so that the remaining reduced cross section cannot support the applied load.
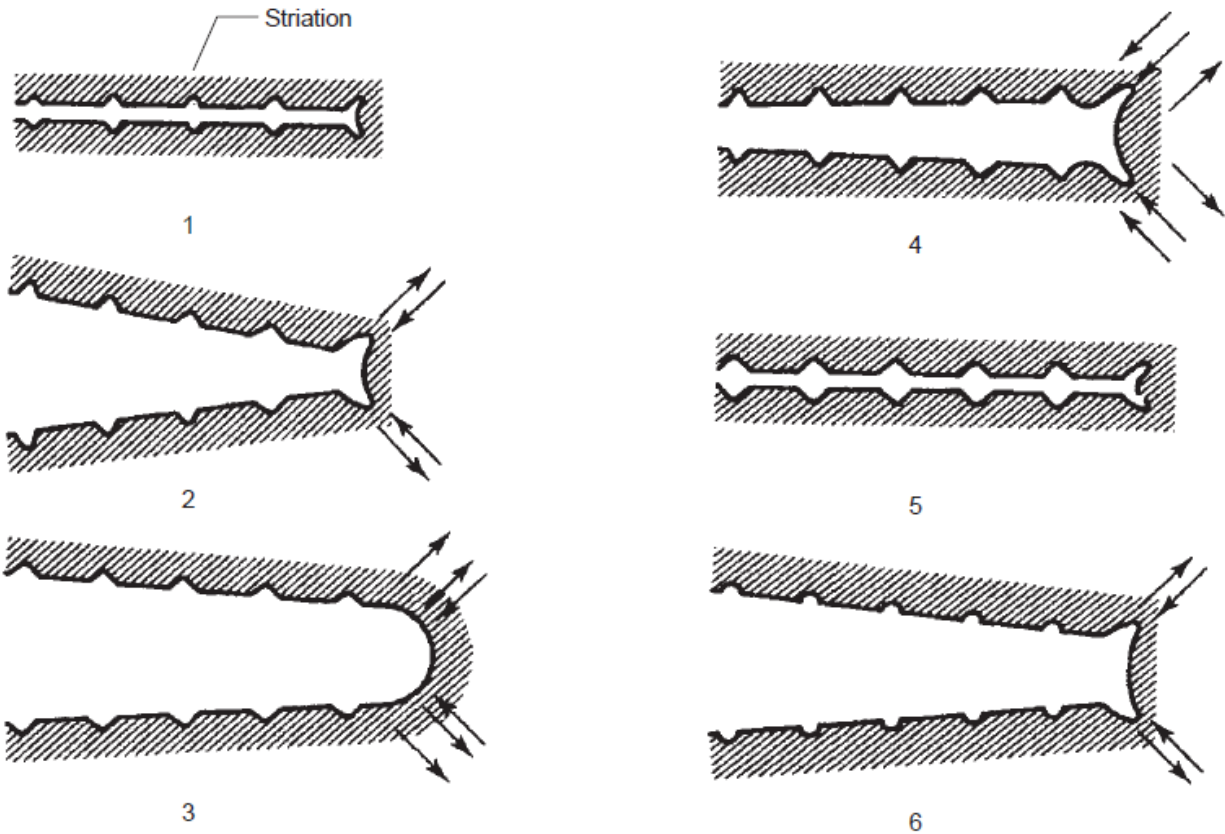
Figure 2.5.9b Crack propagation and growth occurs perpendicular to the principal stress direction by a series of periodic sharpening and blunting mechanisms.

(http://www.asminternational.org/documents/10192/1849770/05224G_Chapter14.pdf)
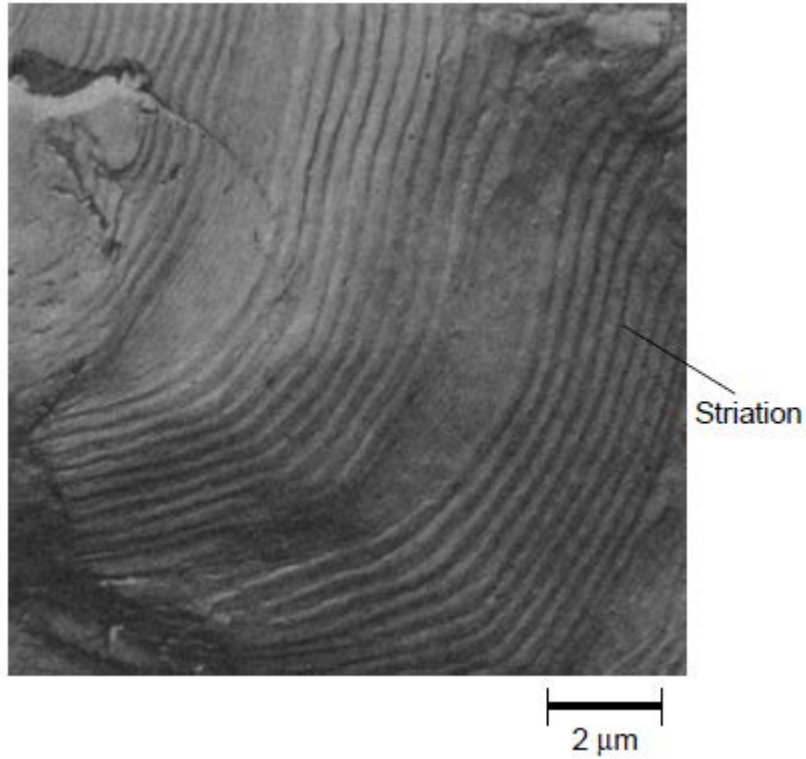
Figure 2.5.9c Microscopic fatigue striations
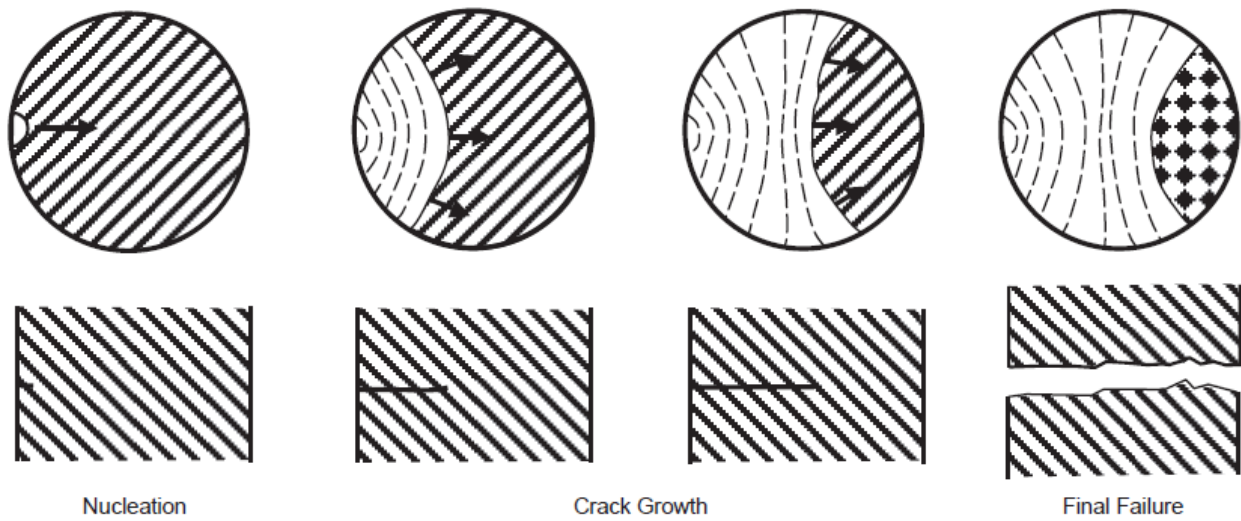
Figure 2.5.9d A schematic of the propagation of fatigue cracks as seen macroscopically as beach marks

(http://www.asminternational.org/documents/10192/1849770/05224G_Chapter14.pdf)

Fatigue crack propagation is described by linear fracture mechanics where a crack of initial size a_o grows to a length a_c when failure occurs. The rate is a function of the number of load cycles, applied stress, and crack length at a given cycle. Growth rate is correlated to a stress-intensity factor, K, and divided into three regions: a region of very slow growth, a region of steady growth, and a reason of rapid growth leading to failure. This is shown graphically in Figure 2.5.9e.
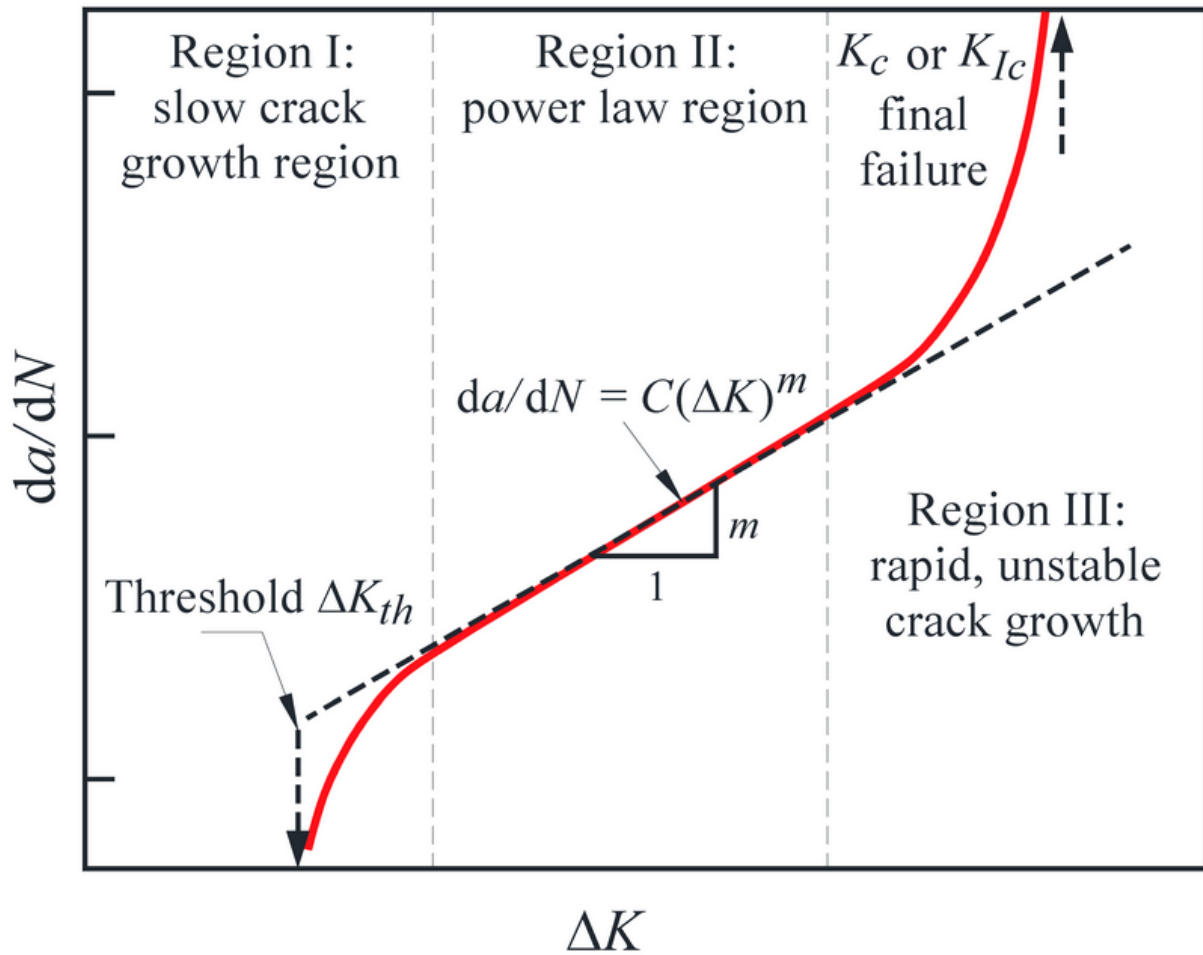
Figure 2.5.9e Crack propagation curve for cyclic loading. In region I, a crack growth threshold, ΔK_{th}, exists below which practically no crack growth occurs. In region II, crack growth rates are stable and linear, and in region III, crack growth is rapid and unstable leading to failure. [119]

The steady crack growth of region II can be modelled by the Paris Law as follows:

50

$$\frac{da}{dN} = C \, (\Delta K)^m \tag{2.16}$$

where a is the crack size, N is the number of cycles, C and m are material constants dependent on environment, temperature, and fatigue stress conditions, and ΔK is the stress-intensity parameter range for linear crack growth. m is typically between 2 and 4 for metals. This law can then be used to predict the number of cycles to failure by relating ΔK to stress via the following:

$$\Delta K = Y \, \Delta \sigma \, \sqrt{\pi a} \tag{2.17}$$

where Y is a specimen geometry dependent constant and $\Delta \sigma = \sigma_{max} - \sigma_{min}$. This equation is then substituted into the Paris Law

$$\frac{da}{dN} = C \, (Y \, \Delta \sigma \, \sqrt{\pi a})^m \tag{2.18}$$

and further rearranged to

$$dN = \frac{da}{C \, (Y \, \Delta \sigma \, \sqrt{\pi a})^m} \tag{2.19}$$

and integrated as follows to solve for N_f

$$N_f = \int_0^{N_f} dN = \frac{1}{C \, \pi^{\frac{m}{2}} \Delta \sigma^m} \int_{a_o}^{a_c} \frac{da}{Y^m a^{\frac{m}{2}}} \tag{2.20}$$

The geometry factor, Y, may or may not depend on the crack length. For metals that are sensitive to the load stress ratio, R, an expression has been developed by Foreman et al.

$$\frac{da}{dN} = \frac{C \, (\Delta K)^m}{(1 - R)K_c - \Delta K} \tag{2.21}$$

The initial and final crack lengths, a_o and a_c, are needed in this case. It is assumed that a subcritical crack will grow to a length of immediate failure where

$$K_c = Y \, \sigma_{max} \sqrt{\pi a_c} \tag{2.22}$$

Thus,

$$a_c = \frac{K_c^2}{\pi Y^2 \sigma_{max}^2} \tag{2.23}$$

These crack propagation laws allow a component to stay in service even if it has a crack by performing crack monitoring and periodic inspection. A fail safe design can be implemented where cracks are detected and repaired before they lead to failure by incorporating multiple load paths and crack stoppers in the structure. This means that if a primary load path fails it

will be picked up by an alternate load path. Damage tolerant design can also be employed where fracture mechanics approaches determine crack growth rates and inspection occurs at various intervals to repair or retire components before cracks grow critical.

2.5.10 Factors that Affect Fatigue Life

Typically, standardized, fully reversed, strain controlled fatigue tests on well-polished samples 6mm in diameter are performed to determine baseline fatigue properties for a metal. However, often times, the actual properties for real components are much different due to many factors. In addition, tests may have to be performed on materials with very different sizes and conditions due to a limit in the amount of available material, safe-handling of the material as is the case with radioactive samples, and the condition of the material if it is an actual component to be tested after service. In order to relate the various tests, it is important to outline various factors that affect fatigue life.

Mean Stress

Most realistic service situations involve materials that incur non-zero mean stresses over their lifetime. Higher mean stresses will cause earlier fatigue failures, and a series of S-N curves is plotted in order to demonstrate this effect as shown in Figure 2.5.10a.
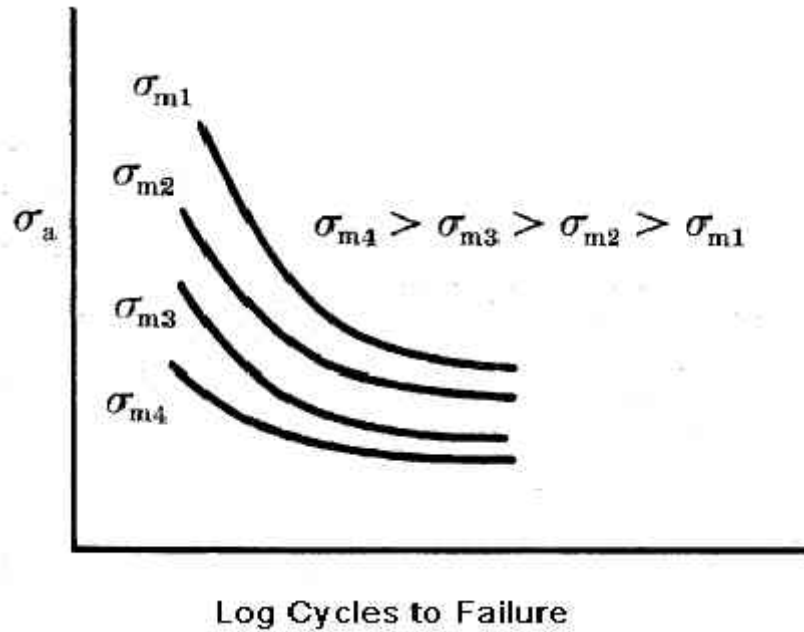
Figure 2.5.10a A demonstration of the effect of various mean stresses on the fatigue behavior of a specimen. (http://www.maintenanceworld.com/fatigue-failures/)

Typically, the effects of mean stress on fatigue life are most noticeable at the long life end of the fatigue spectrum, with compressive mean stresses extending fatigue life and tensile mean stresses decreasing fatigue life. The effect of mean stress diminishes at high strain amplitudes because mean stress relaxation occurs and any mean stress present shits toward zero.

Surface Effects and Treatments

For many common loading situations, maximum stresses occur at the surface, so cracks leading to fatigue failure originate at surface stress amplification sites. Thus, fatigue life is extremely sensitive to surface conditions and configurations. Notches and geometrical discontinuities such as scratches, grooves, holes, keyways, threads, and roughness due to component polishing, machining and preparation act as stress raisers that reduce fatigue life. The sharper the discontinuity, meaning smaller radius of curvature, the more severe the stress concentration. Therefore, smoothing out a material and giving it a well surface polish will greatly lengthen its fatigue life.

53

For high cycle fatigue, imposing a residual compressive stress by shot peening or other methods within a thin outer surface layer will increase its overall fatigue life because tensile stresses of external origin will be reduced. Shot peening is performed by firing small, hard projectiles at high velocities onto the surface to be treated and inducing compressive stresses between one-quarter and one-half the size of the shot diameter of the particles. Laser peening has become increasingly important as well. In this process, a laser pulse generates a shock wave on the sample surface which evaporates a thin water film. This process creates residual compressive stresses deeper than shot peening. Carburizing and nitriding can also be done to create a harder outer shell with residual compressive stresses. Reduction of porosity by hot isostatic pressing can also be performed.

Environmental Effects

Corrosive attacks can create pits on the surface of a material that will act as stress concentrations and initiate cracking as well as accelerate crack growth, drastically reducing fatigue life. These effects may also erase a metal's fatigue limit or its steady state crack growth that can be modelled by the Paris Law. Slow cycling rates will allow corrosive effects to have a larger impact than rapid cycling because corrosion is time dependent. In cases where it is known that corrosive effects are present, materials should be engineered to first combat corrosion before fatigue using corrosion resistant film coatings and compressive residual stresses.

Materials may be fatigued due to thermal stresses caused by temperature fluctuations and constraints on a material's expansion or compression. This thermal stress can be given as

$$\sigma_{th} = \alpha E \Delta T \qquad (2.24)$$

A rapid temperature change may cause a material to fail in one cycle, thermal shock, or after multiple thermal cycles, thermal fatigue. A thermal fatigue parameter

$$\frac{\sigma_f k}{E \, \alpha} \qquad (2.25)$$

where σ_f is the mean fatigue strength, k is thermal conductivity, E is Young's modulus and α is the coefficient of thermal expansion is a good gauge of whether a material is resistant to thermal fatigue. High values indicate strong thermal fatigue resistance.

In addition, normal mechanical fatigue can occur in combination with thermal fatigue, decreasing fatigue life, or mechanical fatigue can occur at reduced or elevated temperatures. Detrimental fatigue effects can be accelerated by creep, and when temperatures half that of the metal's melting point or higher exist, creep will become the dominant failure mechanism. Elevated temperatures can also erase a material's fatigue limit. Alloys that have the highest creep strengths will have the highest temperature fatigue strength. Also, fine grain sizes and beneficial residual stresses may be annealed out at high temperatures, decreasing the metal's fatigue life.

2.5.11 Fatigue of Single Crystal Cu

The majority of work focused on the response of pure fcc metals to cyclic loading is comprised by work on single crystal copper. The fatigue of single crystal copper can be broken up into three regions corresponding to its cyclic stress strain curve. The first is an initial hardening period due to the accumulation of unit loop patches with a relatively low density of screw dislocations at plastic strains less than 6×10^{-5}. The second is a quasi steady-state saturation regime that can be broken up into two segments where in the first phase soft PSBs form in a ladder structure that coexists with the hard pre-existing loop patches in the matrix for plastic strains between 6×10^{-5} and 2×10^{-3}. In the second segment, plastic strains between 2×10^{-3} and 7.5×10^{-3}, an increasing contribution of secondary slip causes most of the hard matrix phase and part of the PSB phase to be configured in labyrinth mazes. In the last region for strains greater than 7.5×10^{-3}, these maze like structures become increasingly refined into dislocation cells by multiple slip phenomena. A depiction of these structures can be seen in Figure 2.5.11a [107]. In addition, the cyclic stress-strain curve for fatigued single crystal copper can be seen in Figure 2.5.11b. A fatigue limit for single crystal copper occurs at a stress of 28 MPa or a plastic strain of 6×10^{-5} [108].
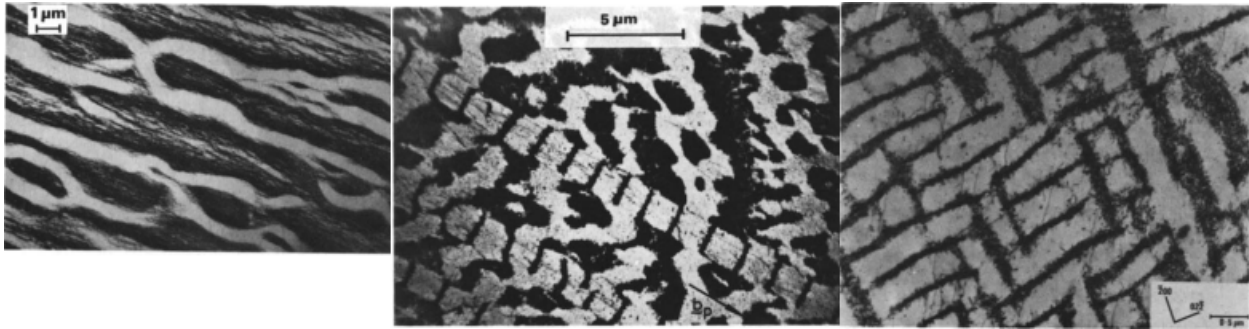
Figure 2.5.11a TEM electron micrographs showing the dislocation structures in single crystal copper after cyclic loading was performed at plastic strain amplitudes less than 6×10^{-5} (left), between 6×10^{-5} and 2×10^{-3} (middle), and greater than 2×10^{-3} (right) [107].
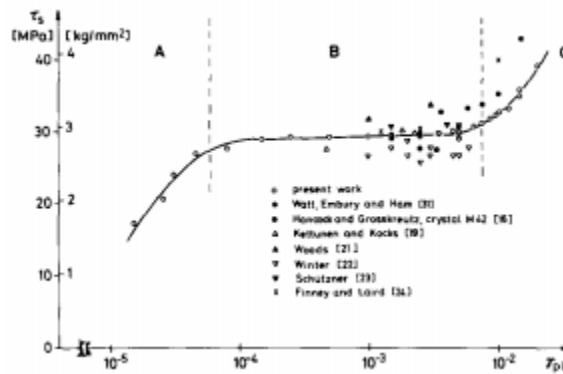
Figure 2.5.11b Cyclic stress-strain curve for fatigued single crystal copper where region A represents an initial hardening period, region B represents a steady-state plateau where PSBs are formed, and region C represents a rapid stress increase toward failure. The stress values are saturation stresses [108].

2.5.12 Fatigue of ECAP Cu

It is well known that the grain boundaries of UFG materials serve as obstacles to dislocation movement and increase the yield point of the material according to the Hall-Petch relation [29, 30]

$$\sigma_y = \sigma_o + \frac{k}{\sqrt{d}} \tag{2.26}$$

where σ_y is the yield stress for a polycrystal, σ_o is the yield stress for a single crystal, k is the Hall-Petch parameter, and d is the average grain size. However, the Hall-Petch parameter, k, does not remain constant over all fine grain regions. A plot of the strengthening effect due to decreasing grain size can be seen in Figure 2.5.12a. There is a limit at 10 nm where the volume fraction of grain boundaries is larger than 50% because grain boundary sliding dominates the deformation process [109].
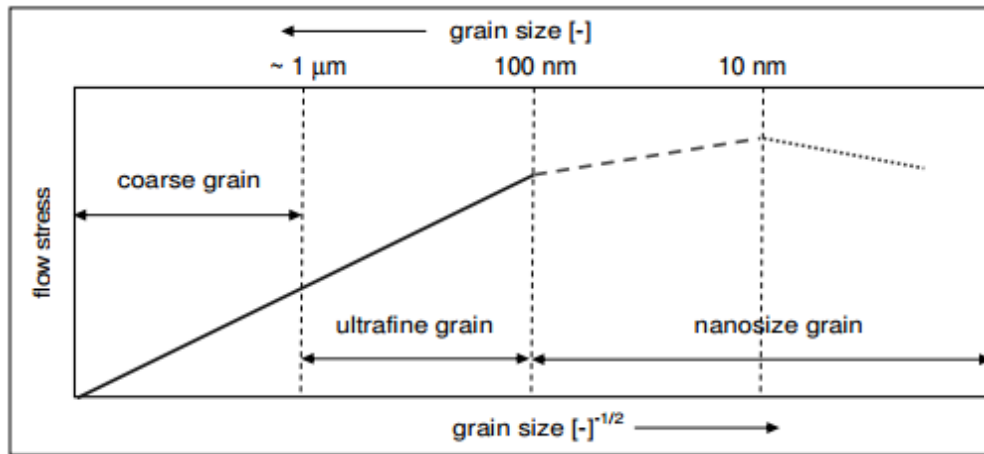
Figure 2.5.12a Strengthening effects as a function of grain size [109]

For grains larger than 100 nm, dislocation effects dominate deformation. In this case, under an applied load, dislocations more through the lattice until they encounter a grain boundary where a large atomic mismatch between the grains creates a repulsive stress field opposing further dislocation motion. As a result dislocations will pile up along this grain boundary and generate repulsive stress fields on the order of

$$\sigma_d \approx \frac{Gb}{r} \tag{2.27}$$

where σ_d is the dislocation stress, G is the shear modulus, b is the Bergers vector, and r is the distance from the dislocation. Eventually after many dislocations pile up, in combination with the applied stress, they will generate a total stress field large enough for dislocations to diffuse across the grain boundary or in cases of high misorientation to create new dislocation sources in the neighboring grain.

$$\sigma_{total} = \sigma_{applied} + n_{dislocations}\sigma_d \qquad (2.28)$$

Smaller grains do not allow as many dislocations to pile up, reducing the total stress field generated and making it more difficult to cross a grain boundary. Eventually, when the grain boundary size approaches the dislocation size, this pile up effect is eliminated because only one or two dislocations can fit inside a grain. Here, a combination of diffusion and shear causes grain boundary sliding [110]. An illustration of deformation mechanisms in an UFG material can be seen in Figure 2.5.12b.
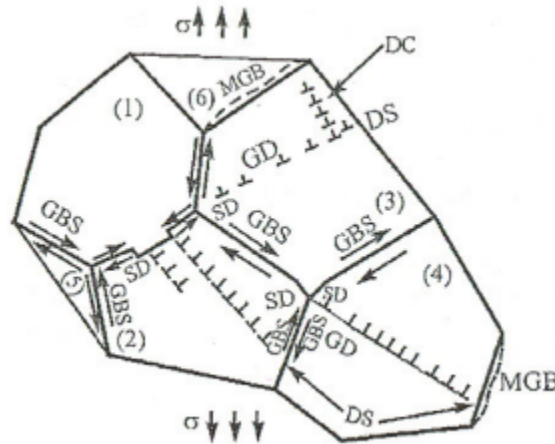
Figure 2.5.12b An illustration of deformation mechanisms in an UFG material. Grain boundary sliding (GBS) occurs along with intergranular dislocation processes: dislocation gliding (GD), migrating grain boundaries (MGB), dislocation sinks (DS), dislocation sources (SD), and dislocation climbing (DC) [110].

However, this enhanced strengthening mechanism of UFG materials does not translate into superior fatigue properties across the entire fatigue life spectrum. The low cycle fatigue (LCF) behavior of UFG materials is inferior to its course grain counterparts, whereas its high cycle fatigue (HCF) is greatly enhanced. A schematic representation of this effect can be seen in Figure 2.5.12c.
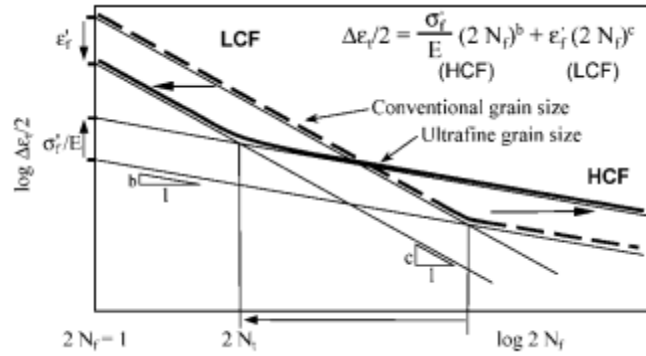
Figure 2.5.12c A schematic representation of the enhanced HCF and reduced LCF of UFG materials due to their increased strength, an increase in the σ_f'/E term, but reduced ductility, a decrease in the ε_f' term. The combined effects also reduce the transition fatigue life, N_t, of UFG materials [111].

An example of this effect in UFG ECAP copper and aluminum can be seen in Figure 2.5.12d.
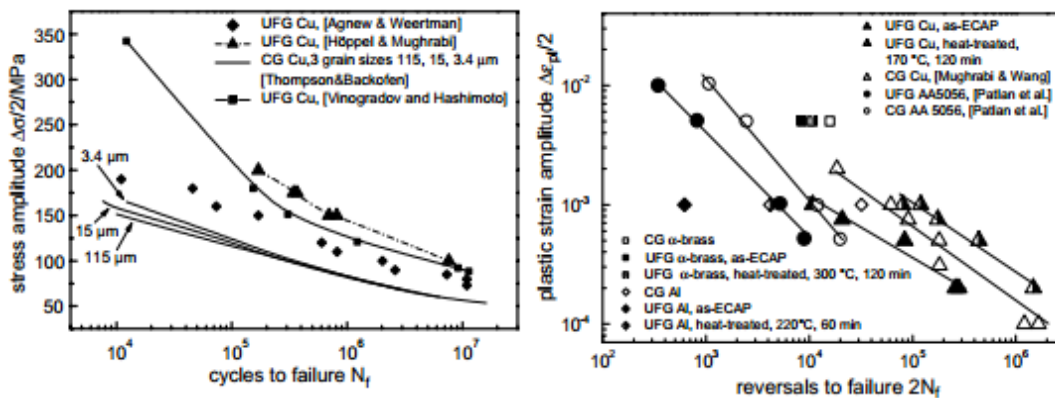
Figure 2.5.12d The enhanced HCF of ECAP Cu compared to its course grain counterparts on the left and the reduced LCF of UFG materials compared to their course grained counterparts on the right [111].

In order to improve the LCF of UFG materials, they can be annealed at low temperatures below the recrystallization temperature, a purely recovery heat treatment, at slow heating rates, 0.5 ᵒC/min. Optimal heat treatments for ECAP copper were at a final temperature 170 ᵒC for 2 hours, although partial recrystallization occurred, leaving a bimodal grain structure with large grains embedded in the original UFG structure. The bimodal grain structure provides the highest fatigue life because it is the optimal combination of strength and

ductility. Increased strength is maintained in the smallest grains, while increased ductility occurs in the larger grains. Even with this improvement, the UFG LCF life will always be less than that of its course grain counterpart [111].

During fatigue testing of ECAP copper, cyclic softening occurs in the LCF regime, but ECAP Cu remains relatively cyclically stable in the HCF regime for stress amplitudes below 200 MPa. This can be seen in Figure 2.5.12e. This softening effect during LCF is amplified with lower strain amplitudes and reaches a maximum at a plastic strain around 2×10^{-4}. At lower plastic strains, the effect vanishes.
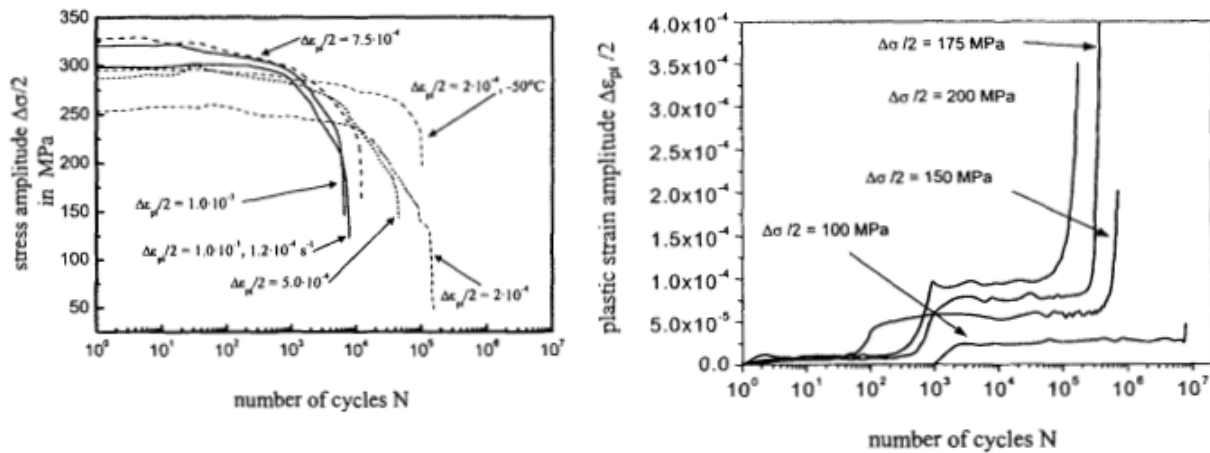
Figure 2.5.12e Cyclic softening is clearly evident during LCF of ECAP Cu, left. However, during HCF, ECAP Cu is cyclically stable under rapid failure occurs, right. [112]

During the fatigue process, ECAP copper has been known to undergo microstructural changes, specifically during LCF strain controlled fatigue tests. The amount of grain coarsening is highly dependent upon the plastic strain amplitude. Strong coarsening effects were noticed during testing at strain amplitudes of 2×10^{-4} and 1.2×10^{-4}, but these effects were absent at a plastic strain amplitude of 1×10^{-3}. In addition, these effects were absent at low temperatures, regardless of strain rate as well as during HCF stress controlled tests. Thus, the grain growth is a thermally activated, time dependent process. This grain growth is directly related to the cyclic softening behavior seen in Figure 2.5.12e on the left. Micrographs showing grain evolution for various conditions can be seen in Figure 2.5.12f.
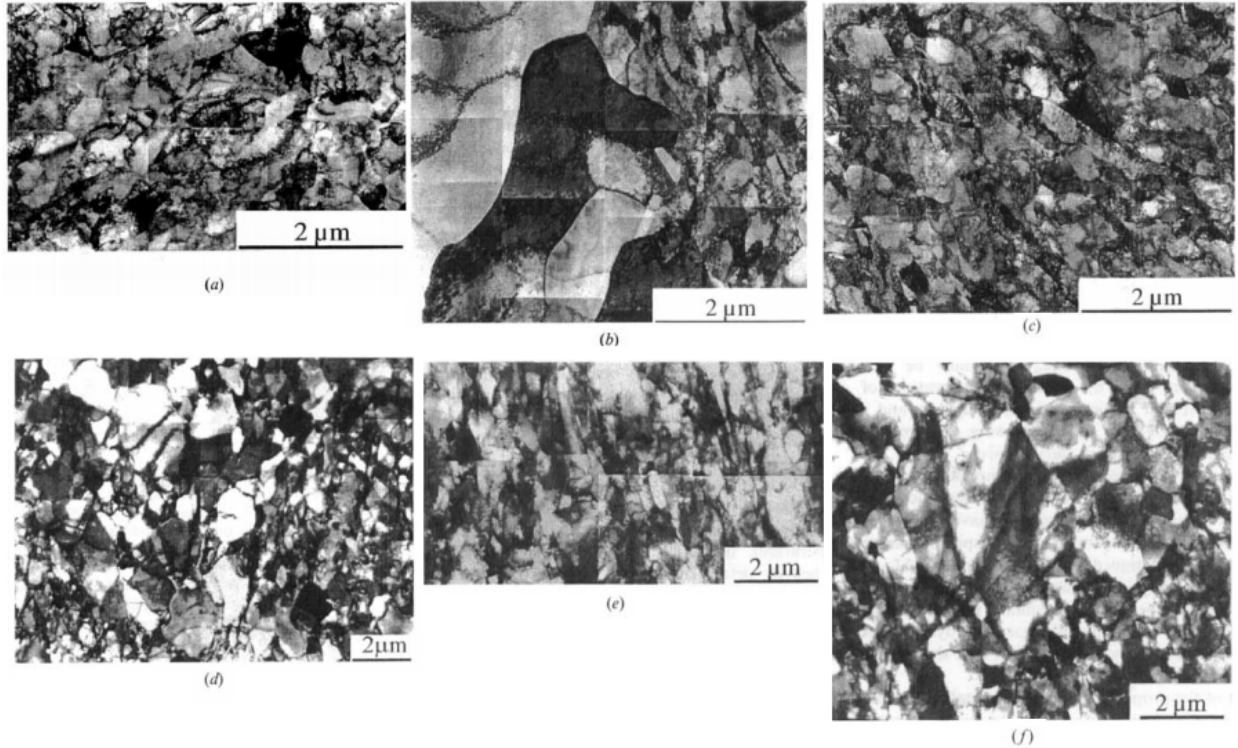
Figure 2.5.12f Micrographs of the grain structure of ECAP Cu (a) initially, (b) after a large amount of grain coarsening at a plastic strain amplitude of 2 x 10^{-4}, (c) minimal effects after a plastic strain amplitude of 1 x 10^{-3}, (d) the most severe grain coarsening after a plastic strain amplitude of 1.2 x 10^{-4}, (e) minimal effects after a stress amplitude of 100 MPa, and (f) grain growth after a stress amplitude of 200 MPa. [112]

It is believed that a dynamic recrystallization process is responsible for grain growth during the fatigue of ECAP copper due to its initially highly pre-deformed structure with a high dislocation density allowing growth to occur at homologous temperatures of $T/T_m < 0.22$. This recrystallization can be nucleation and growth of new grains and subsequent migration of high angle grain boundaries. Disappearance of subgrain boundaries may also be responsible for some growth. However, cyclic softening that is not accompanied by grain growth like in Figure 2.5.12f (c) must be governed by dynamic recovery, only reduction in dislocation density, without dynamic recrystallization within its fatigue life. [112]

2.5.13 Fatigue of ODS Steel

It is well known that the nano-oxide precipitates in ODS steels serve as obstacles to dislocation movement and highly strengthen the material. However, the knowledge of low-cycle fatigue properties of ODS steels is very limited. A few recent studies, all within the past 8 years, on 9Cr martensitic nd 12Cr ferritic ODS steels at high temperature [113], Eurofer 97 ferritic-martensitic ODS [114] at RT, and CEA and EFPL ferritic ODS at both RT and high temperature [115] have been performed. The 9Cr and 12Cr ferritic ODS steels proved to exhibit increased cyclic strength and have longer fatigue lives than their conventional non-ODS counterparts in the low total strain region. Also, the 9Cr and 12Cr ODS steels did not show any signs of cyclic hardening or softening, but their non-ODS counterpart does as seen in Figure 2.5.13a. A schematic diagram comparing the fatigue lives of ODS and non-ODS ferritic steels can be seen in Figure 2.5.13b.
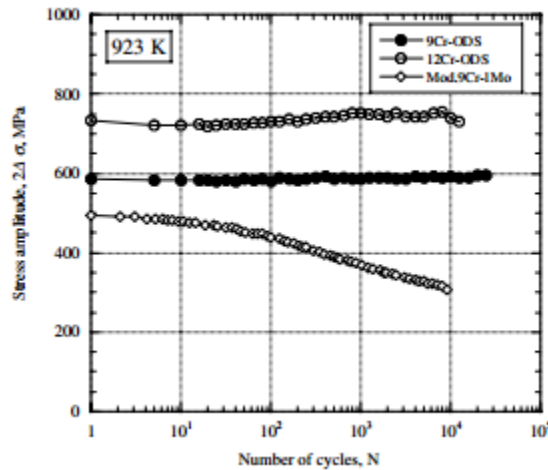
Figure 2.5.13a The stress amplitude of 9Cr and 12Cr ferritic ODS steels and a Mod. 9Cr-1Mo ferritic non-ODS steel as a function of the number of fatigue cycles at 923 K. The ODS steels do not show cyclic hardening or softening, but the non-ODS steel shows almost immediate cyclic softening [113].
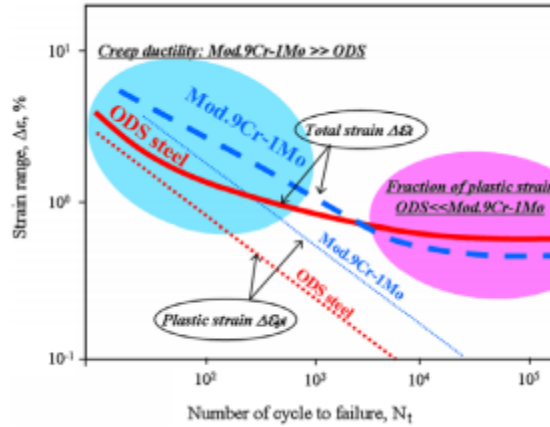
Figure 2.5.13b A schematic comparing the full fatigue lives of ODS and non-ODS steels [113].

However, room temperature strain controlled fatigue studies performed on ODS Eurofer 97 have shown cyclic softening, although this softening is greatly reduced from that of non-ODS Eurofer 97. The ODS particles appear to give the Eurofer 97 increased cyclic stability. Again the ODS version of this steel shows a stronger cyclic strength, almost double, than its counterpart. This can be seen in Figure 2.5.13c. Higher fatigue lives occur in the ODS steel for high cycle fatigue modelled by the Basquin curve, but lower fatigue lives occur in the low cycle regime modelled by the Coffin-Manson curve. This can be seen in Figure 2.5.13d. [114].
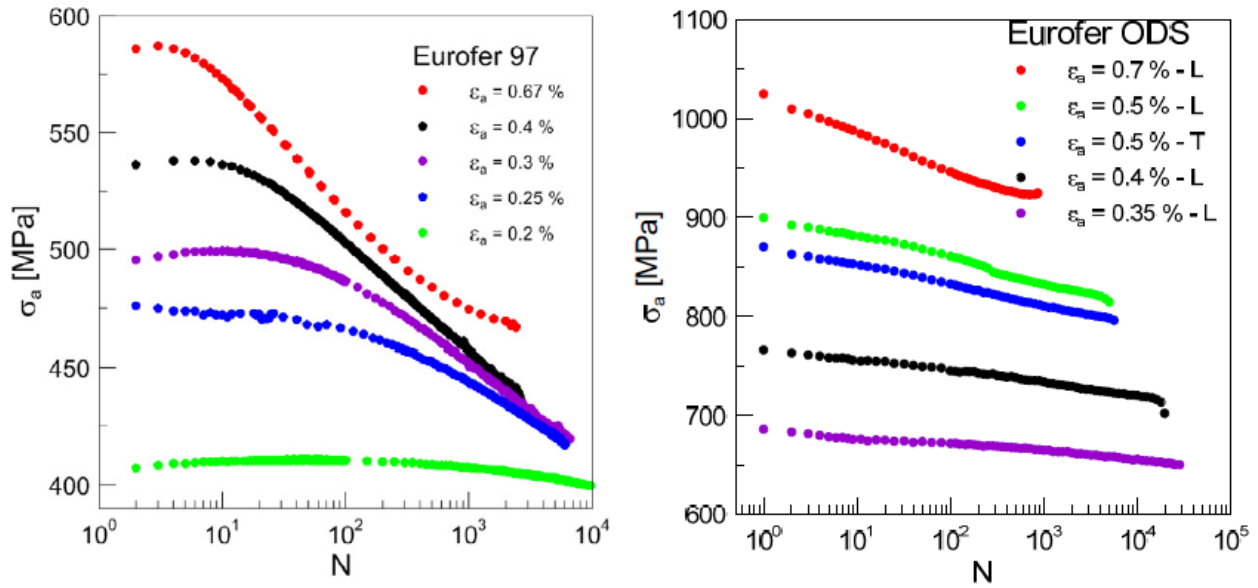
Figure 2.5.13c The cyclic stress amplitude behavior of Eurofer 97 without ODS particles, left, and with ODS particles, right [114]
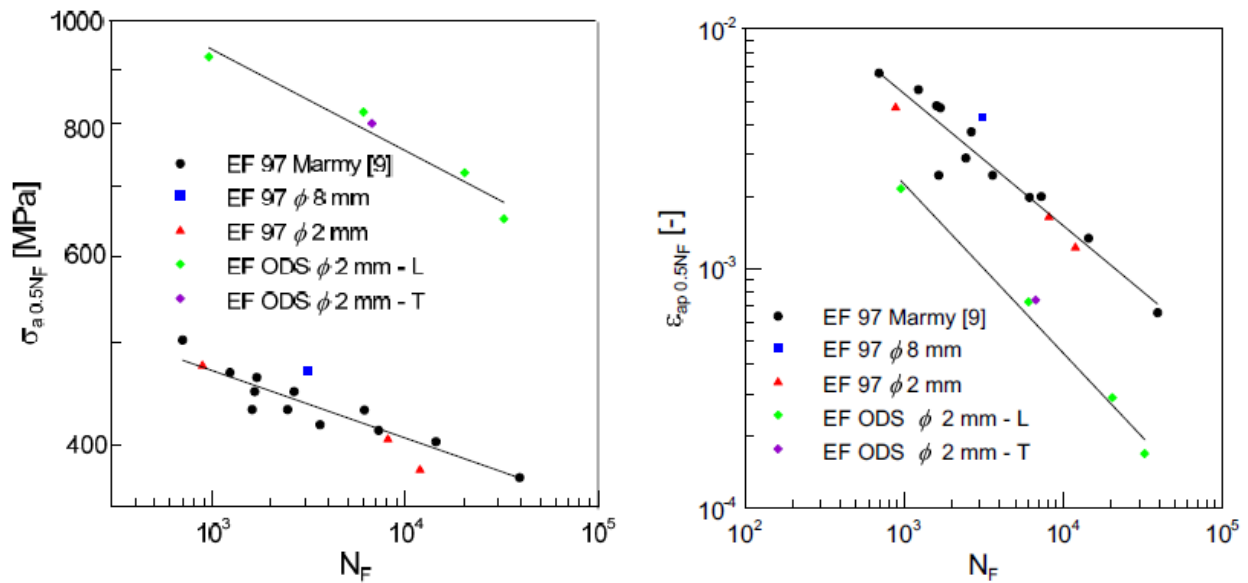
Figure 2.5.13d Fatigue life curves of Eurofer 97 and ODS Eurofer 97, showing that in the high cycle regime, left, the ODS material has a much longer fatigue life. However, in the low cycle regime, right, the ODS material has a much shorter fatigue life [114].

When this same ODS Eurofer 97 steel has been fatigued at higher temperatures, 650 °C and 750 °C, it becomes even more cyclically stable. The same occurs for two other European companion ODS steels, CEA and EPFL, as can be seen in Figure 2.5.13e.
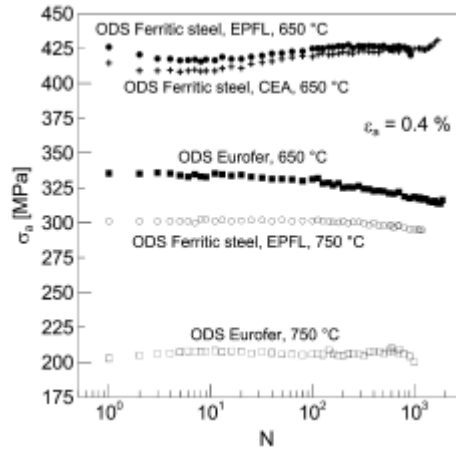
Figure 2.5.13e Cyclic stress evolution of three ODS steels, Eurofer, CEA, and EPFL, at 650 °C and 750 °C at a plastic strain amplitude of 0.4%. For EPFL and CEA, an initial cyclic softening less than 20 MPa occurs within the first 10 cycles followed by hardening back to original strength at 650 °C. The Eurofer is cyclically stable for the first 100 cycles and then cyclically softens by 40 MPa by cycle number 2000. Cyclic stability occurs at 750 °C for all samples [115].

3. Experimental Procedures

3.1 Cu-Nb Alloys

3.1.1 Starting Powders

The starting powders were purchased from Alfa Aesar, Johnson Matthey Catalog Company, Inc. USA as 99.999% pure copper powder with a mesh size of 100 (149 µm) and pure niobium powder with a mesh size of 325 (44 µm).

3.1.2 Powder Processing

The powders were ball milled under Argon atmosphere in the Simoloyer CM01 powder processing center at UC Berkeley. The powders were mixed with different compositions for different milling times as shown below in Table 3.1. The milling media consists of type 316 stainless steel balls (1 kg), with an average mass of 43 mg and an average diameter of 4.7 mm up to a rotor speed of 1200 rpm. The powder to ball weight ratio was kept larger than 1:10. Tungsten carbide balls were attempted for one sample but they fractured during the milling process and contaminated the powder, so it was decided that stainless steel balls were a better medium.

3.1.3 High Pressure Torsion

Several 8 mm diameter disk shaped samples of Cu-Nb alloys were manufactured by consolidating the powders using the HPT methods described in section 2.3.2 under a pressure of 7.68 GPa. In order to avoid outflow of the powder mixture during compaction, a thin 8 mm diameter copper ring was used to hold the powder in place. A photograph of the anvil with the copper ring can be seen in Figure 3.1.3a. The height of the powder pre-deformation was approximately 2 mm and after deformation approximately 0.6 mm. The applied torsional rotation speed was 0.6 rpm and the applied number of revolutions for the different samples has a large range between 1 and 246 as seen in Table 3.1. However, the force was kept constant at 385 kN. The upper plunger was cooled with compressed air during the entire HPT process. Some tests were performed at RT and others at 170 ^{o}C, 200 ^{o}C, and 250 ^{o}C as seen in Table 3.1. These Cu-Nb alloy samples typically become very dense within only a few revolutions of the HPT process and further revolutions appear to cause the alloys to become extremely brittle and flake apart more easily during further sample preparation.
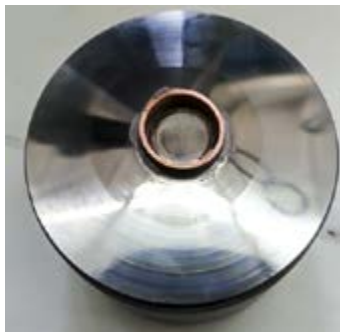
Figure 3.1.3a A photograph showing the glued copper ring on the anvil used for confinement of the Cu-Nb powders during initial compression

Table 3.1 Sample Bank of Cu-Nb Alloys

Sample Composition (Cu-Nb wt%)	Milling Time (hrs)	Number of HPT Turns	Temperature of HPT (^{o}C)
50-50	17	1	RT
50-50	17	10	RT
50-50	17	32	RT
50-50	17	51	RT
50-50	17	246	RT
50-50	17	5	170
50-50	17	5	200
50-50	17	5	250
75-25	40	5	RT

3.1.3 Preparation of Microsections

The investigation of the microstructure and the measurement of microhardness requires a smooth surface. In addition, subsequent microhardness should be performed in a homogeneous zone in the middle of the disk with respect to height. Thus, the finished Cu-Nb disks were cut in half precisely in the center using a diamond wire saw and subsequently mechanically polished first with silicon carbide grinding paper and then with a final polish using a 1 μm diamond suspension.

3.1.3 Microhardness

In order to validate the success of the HPT procedure, microhardness experiments were conducted with a Buehler Micromet 5100 after the polishing process with a weight of 500 gf to obtain radial Vickers hardness profiles across the entire cross section of each sample with a distance of 500 μm between each indent and between the edge of the sample and the first indent closest to the edge on each side. A photograph of a representative HPT Cu-Nb alloy disc sample can be seen in Figure 3.1.3a.
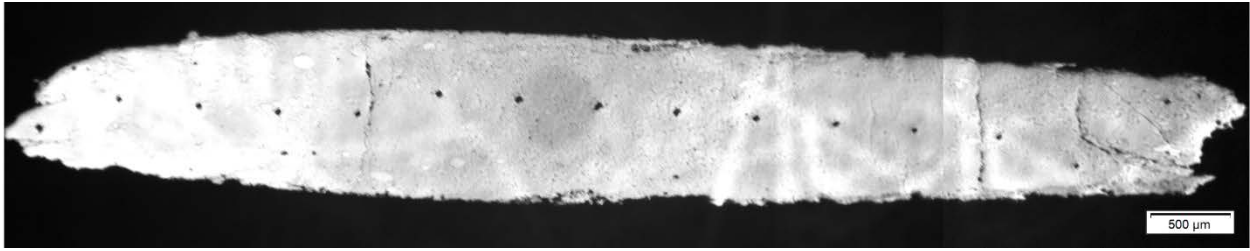
Figure 3.1.3a Optical micrograph of 50-50 Cu-Nb alloy ball milled for 17 hours after HPT of 1 turn with Vickers microhardness indents

3.2 Microfatigue Bend Bars

There are four microfatigue bend bars that were produced and investigated for this report. The first was fabricated from course-grained off the shelf copper and validated to be a single crystal fatigue bar by EBSD before testing. The second was fabricated from a cross-sectional slice of an ECAP copper rod 25 mm in diameter that underwent 8 deformation passes via Route Bc with a channel-intersection angle of 90°, having a grain size of approximately 200 nm. The ECAP process has been described in great detail in section 2.3.1. The third was a single crystal, validated by EBSD pre-test, PM 2000 steel fatigue bar. This PM 2000 steel was manufactured by PLANSEE and is described in section 2.2.1. The fourth was an HPT PM 2000 fatigue bar made after performing 26 revolutions at 0.6 rpm under a pressure of 7.6 GPa on a solid 8 mm PM 2000 disk with an initial thickness of 2 mm.

3.2.1 Mechanical Preparation

The original slices of all four metals were cut using a diamond wire saw and mechanically polished by 800 grit SiC paper into small bars of approximate dimensions 1 mm x 1 mm in cross section and 6-10 mm long. For the ECAP Cu disc, the bar was cut from a cross-sectional slice so that the radial direction is represented by the length of the bar and the axial extrusion direction by the height of the bar. For the HPT PM 2000 bar, the bar was cut in a similar way from the center of the disk so that its length represents the radial direction. Further polishing

of this bar down to a needle and micro fatigue bar was done close to the edge of the bar but well within 4 mm from the center where HPT grain refinement is greatest on the PM 2000 material desired to be studied. An illustration is provided in Figure 3.2.1a. These four bars were then mounted into specially machined sample holders pictured in Figure 3.2.1b.

Figure 3.2.1a Illustrations of the ECAP Cu slice and highlighted area from which the bar was cut, left, and HPT PM 2000 disk and where the bar was cut from the center, right.

Figure 3.2.1b Photograph of specially machined sample holder for gripping the bars

3.2.2 Needle Fabrication by Electropolishing

All four bars were them electrochemically polished for approximately 90 minutes until the final needles were measured to be 10 μm wide at the tip and 40-80 μm wide approximately 100 μm down from the tip using the circuit set up shown in Figure 3.2.2a. In Figure 3.2.2b an enlargement of the mechanically driven dipping apparatus used for cyclic submerging

and emerging of the bars to polish them into needles is shown. For the two copper bars, electropolishing was performed using Struers Electrolyte D2 at 5.6 V with an initial maximum current of 0.2 µA when the bar was fully submerged to its maximum depth. As the bar was polished into a needle this current value dropped and it read 0.04-0.1 µA when the needle was deemed finished and ready for FIB fabrication. Similarly, the two PM 2000 steel bars were electropolished using Struers Electrolyte A2 at 9 V. Tables 3.2.2a and 3.2.2b shows the compositions of the electrolytes. Finished needles can be seen in Figure 3.2.2c.
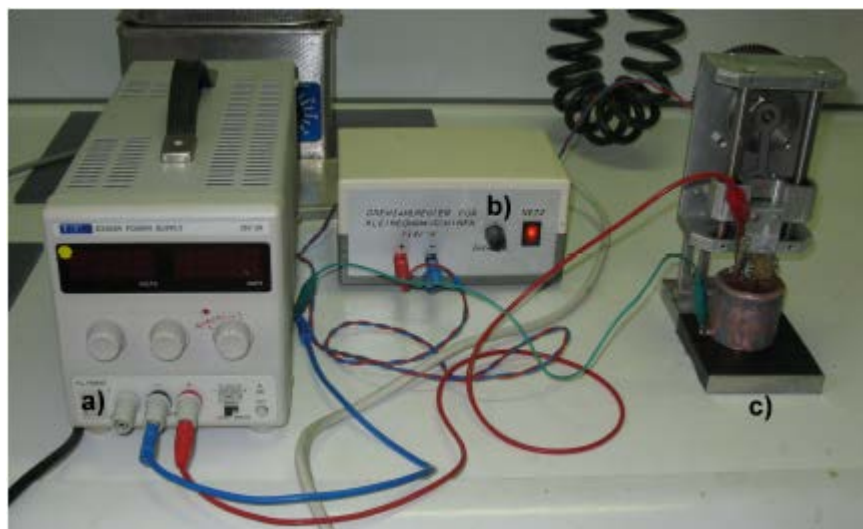
Figure 3.2.2a Circuitry used to perform electropolishing of the initial bars into needles. (a) DC power supply, (b) motor controlling the immersion speed for submerging and surfacing of the sample in the acid solution, (c) Apparatus used to hold the sample
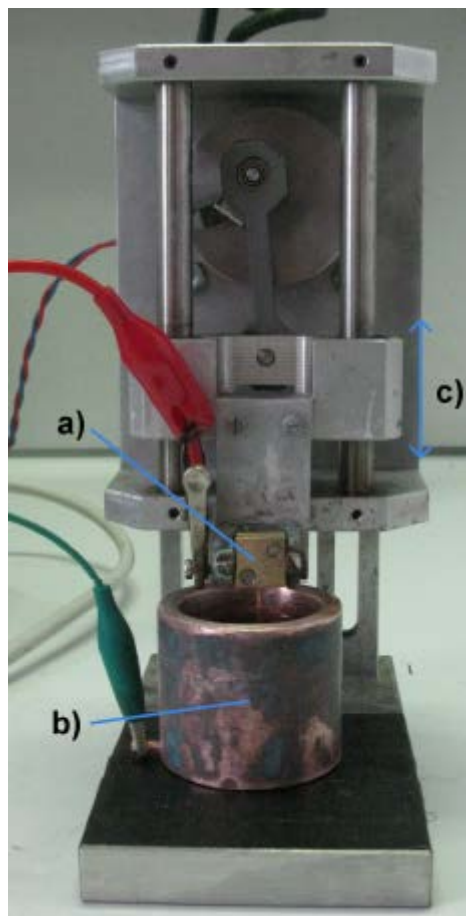
Figure 3.2.2b Close up of needle electropolishing apparatus. (a) Sample holder with bar, (b) copper cup filled with electrolyte, (c) oscillating direction of submerging and surfacing used to obtain needle shape

Table 3.2.2a Composition of Struers Electrolyte A2

Liquid	Quantity
Ethanol	65-85%
2-Butoxyethanol	10-15%
Water	5-15%

Table 3.2.2b Composition of Struers Electrolyte D2

Liquid	Quantity
Water	50-70%
Phosphoric Acid	15-35%
Ethanol	15-25%
Propan-1-ol	< 10%
Urea	< 1%
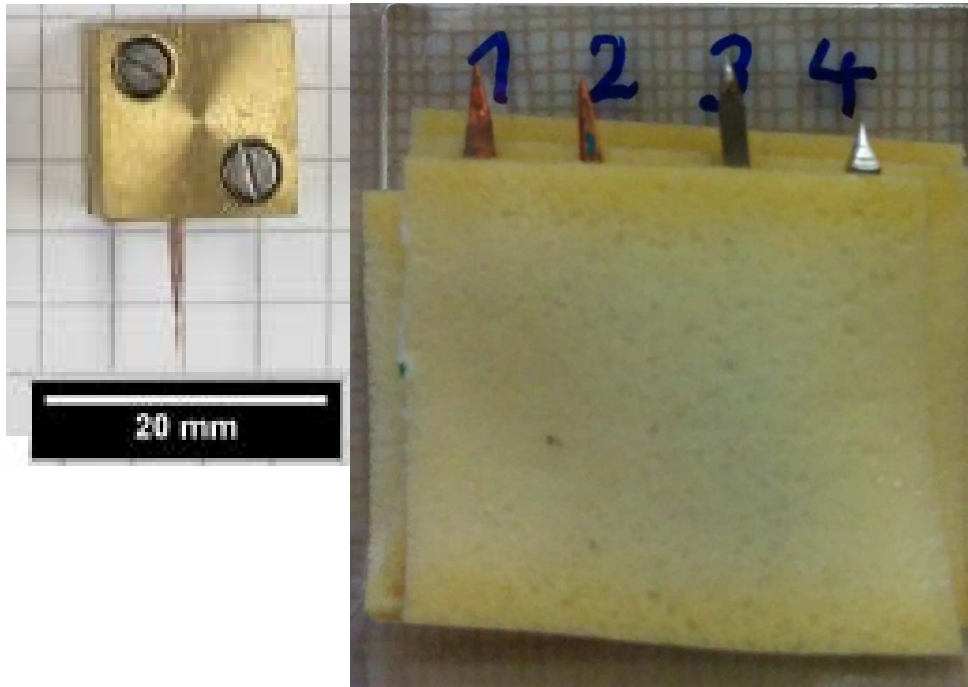
Figure 3.2.2c Finished electropolished needles. An example of the needle mounted in the sample is shown in the left and all four needles are shown on the right.

3.2.3 FIB Fabrication

A Zeiss 1540 XB dual SEM/FIB workstation was used to cut four bending beams with the following final dimensions, height by width by length (h x w x l): 3.6 µm x 3.1 µm x 31.2 µm for the single crystal copper, 4.6 µm x 4.5 µm x 29.7 µm for the ECAP Cu, 4.7 µm x 2.1 µm x 23.9 µm for the single crystal PM 2000, and 4.9 µm x 5.6 µm x 24.4 µm for the HPT PM 2000.

In order to perform the bending a tungsten needle was FIB fabricated with a 7.7 μm opening, first at rough cuts of 10 nA and final polishing cuts at 100 pA to ensure a flat smooth bending contact surface. Figure 3.2.3a shows a representative initial needle and unfinished micro fatigue bar after some rough cutting. Figure 3.2.3b shows the tungsten gripper and Figure 3.2.3c shows the final micro fatigue bars. Rough Ga^+ currents 1-20 nA were applied for quicker course milling and 100 pA was used for final shaping to reduce the ion damage. In order to cut all four sides, the sample holder had to be removed from the FIB mount and rotated 90° ex-situ to cut the remaining two sides after the first two sides had been cut. The software package includes rectangular and trapezoidal patterning options of precise dimensions allowing for easy fabrication. In the Zeiss 1540 XB, the electron and ion beams are offset by 54° as shown in Figure 3.2.3d of the inside of the chamber with a specimen tilted 54° and held in cutting position. Due to beam spreading, after rough cuts the beams appeared trapezoidal. 1°-2° offsets, a tilt of 53° for one edge of the bar and 55° for the other edge of the bar, were applied during the 100 pA polishing cuts in order eliminate this effect and ensure final beams were square.
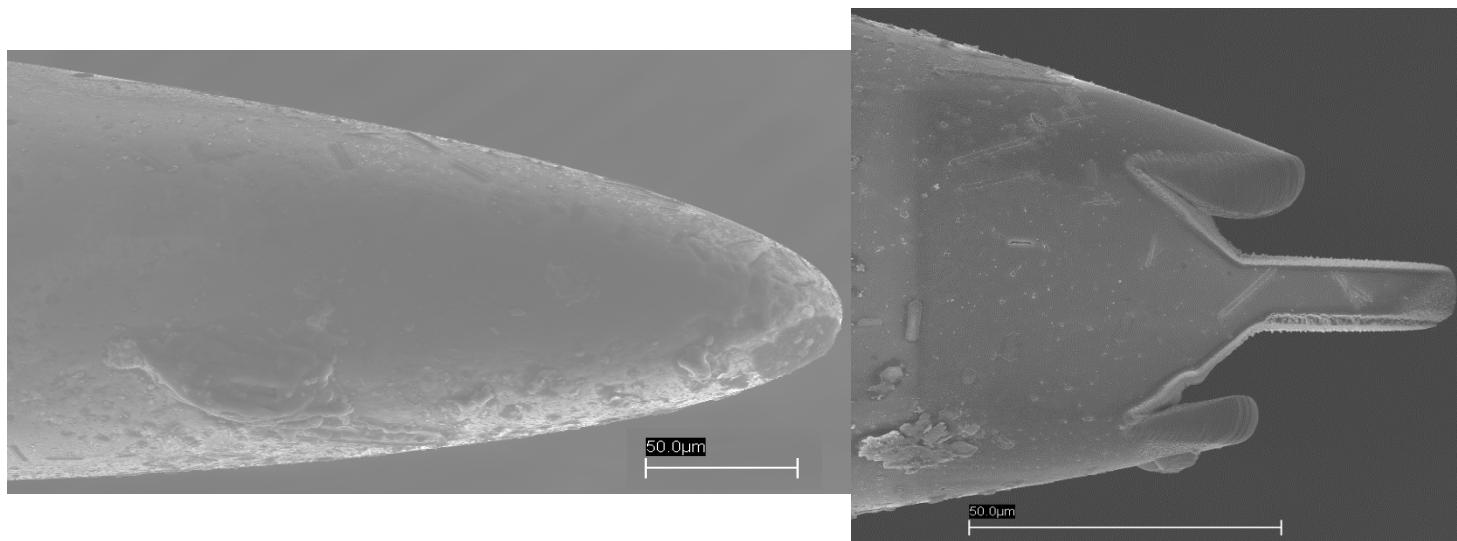
Figure 3.2.3a FIB images showing a representation of the initial needle on the left, and the needle while rough cuts for a micro fatigue bar are being performed on the right.
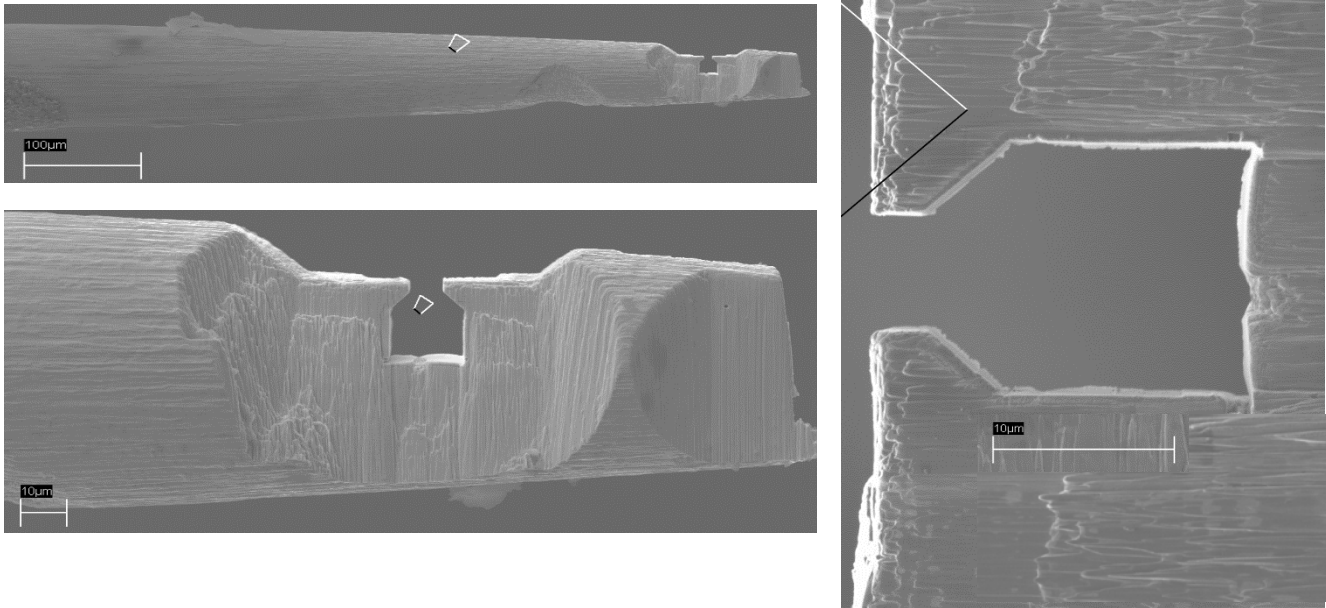
Figure 3.2.3b SEM images showing the tungsten needle with FIB fabricated gripper for cyclic bending tests. In the upper left is a zoomed out view showing the gripper at the end of the needle, on the bottom left a more zoomed view, and on the right the opening used for bending.
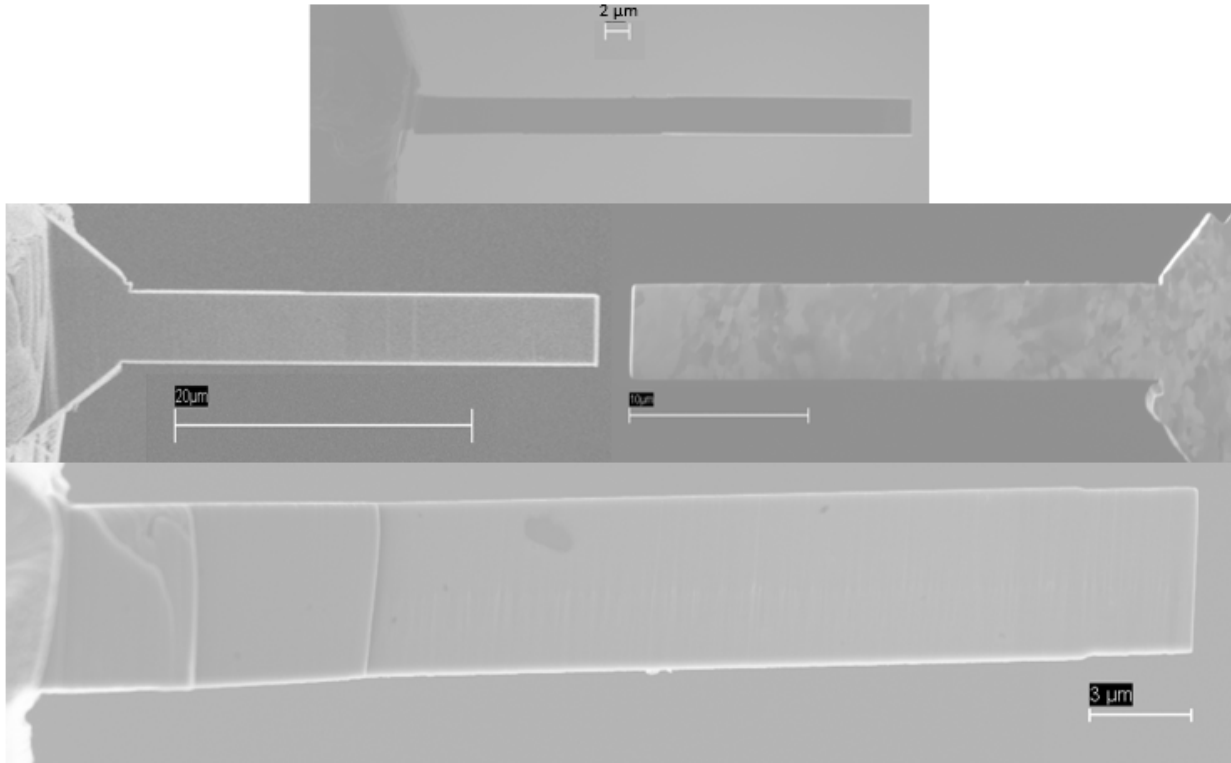
Figure 3.2.3c FIB images showing the final micro fatigue bars. At the top is the single crystal copper, middle left single crystal PM 2000, middle right ECAP Cu, and bottom HPT PM 2000.
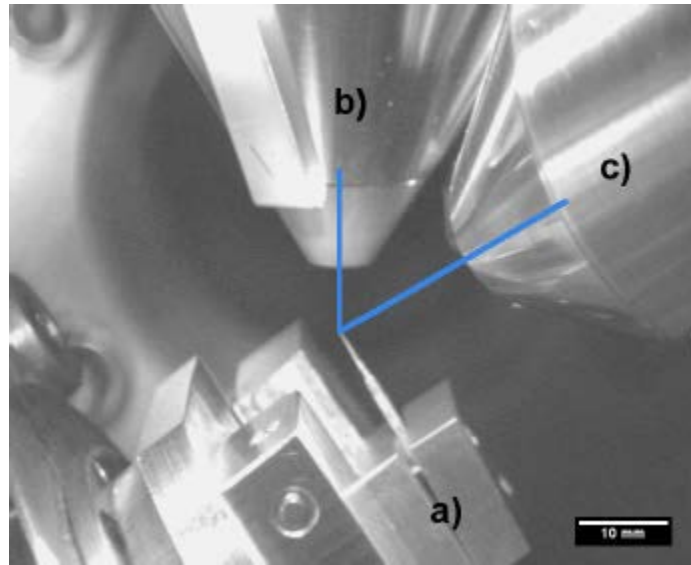
Figure 3.2.3d An IR camera image of the inside of the Zeiss dual SEM/FIB workstation while a micro fatigue bar is being cut showing (a) the sample holder tilted 54° for cutting, (b) the electron beam pole piece for SEM, and (c) the Ga^+ FIB offset from the electron beam by 54°

3.2.4 Cyclic Loading

Sample loading was performed in situ using an Advanced Surface Mechanics (ASMEC) Universal Nanomechanical Tester (UNAT) SEM II mounted inside of a Zeiss Stereoscan SEM 440. The ASMEC UNAT SEM II allows for a maximum displacement of 200 μm and a maximum load of 200 mN in both push and pull directions which is well in excess of what was needed for all bending tests. The full specifications for the instrument are given below in Table 3.2.4. The ASMEC UNAT SEM II is mounted on the chamber wall of the SEM and the moving capabilities of the SEM stage were used for aligning the micro fatigue bars with the tungsten gripper which was threaded onto the measuring head of the ASMEC UNAT SEM II with sensors and actuator. The system has a stiff mechanical Z stage for moving the head, and for the tests in this report the head was set to 5 mm since that is the working distance of the SEM in order to obtain good alignment and SEM pictures before, during, and after testing. In order to move the gripper into place, there is a feed through flange with a mechanically driven crank to move the gripper by hand from the side wall of the chamber towards the center of the chamber. The set up for performing in situ testing can be seen in Figure 3.2.4a.

Table 3.2.4 Specifications of ASMEC UNAT SEM II

Type	UNAT-SEM II
Maximum test force	± 200 mN (push and pull)
Maximum displacement	± 200 µm at 20 mN; ± 150 µm at 200 mN
Digital force resolution	≤ 0.02 µN
Digital displacement resolution	≤ 0.001 nm
RMS noise level force	≤ 0.5 µN
RMS noise level displacement	≤ 0.5 nm
X and Y-stage travel range	12 mm
X and Y-stage positioning accuracy	≤ 50 nm
X and Y-stage resolution of positioning system	1 nm
Z-stage travel range	15 mm (25 mm optional)
Z-stage positioning accuracy	≤ 0.1 µm
Z-stage resolution of positioning system	50 nm

Figure 3.2.4a The ASMEC UNAT SEM II mounted on the chamber wall of the Zeiss Stereoscan SEM 440. (a) is the SEM electron gun, (b) is the xyz moveable SEM sample stage, (c) is the moveable indenter plate of the ASMEC UNAT SEM II, and (d) is indenter head tip

The ASMEC UNAT SEM II software was easily adjustable for handling cyclic loading as seen in Figure 3.2.4b. 120 load-displacement data points were recorded for each cycle. Good alignment between sample and gripper without prior contact to testing with the possibility of adjusting bending length if desired is essential and can be seen in Figure 3.2.4c. All cyclic

loading was performed under closed loop displacement control with R = -1 with a sinusoidal displacement at a frequency of f = 0.033 s⁻¹ as shown in Figure 3.2.4d. Video synchronization was used to take real time videos of the first and last cycles of tests at each amplitude for all four micro fatigue bars. A representative nominal ±2.3 µm loading cycle for the ECAP Cu fatigue bar can also be seen in Figure 3.2.4c.
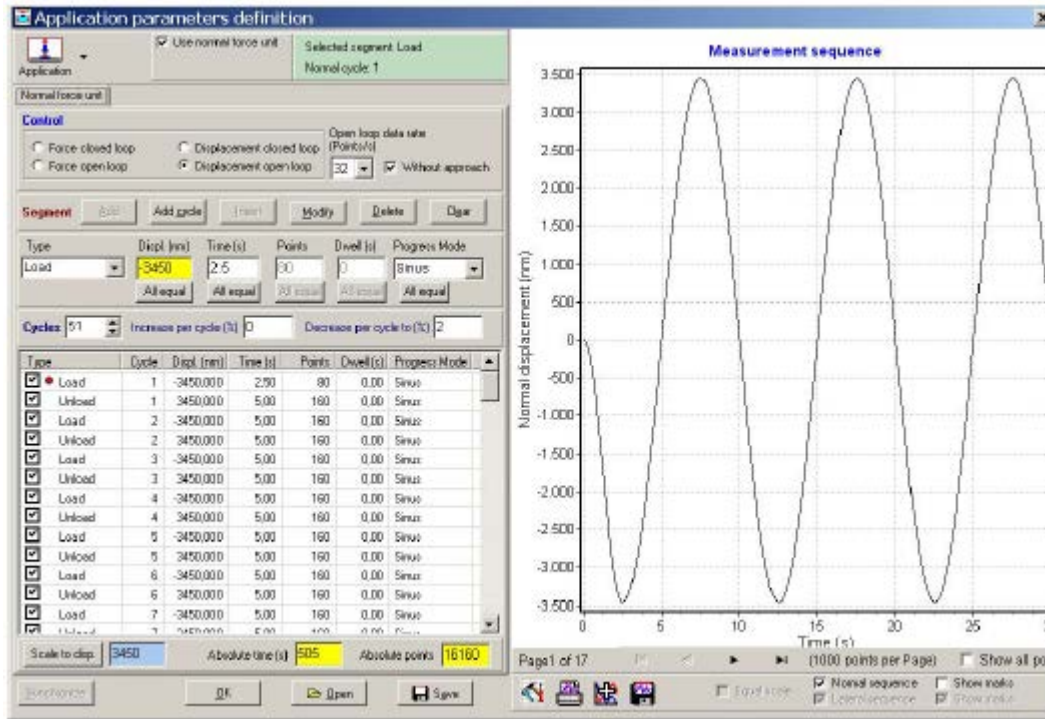
Figure 3.2.4b An example of the ASMEC UNAT SEM II software interface configured for cyclic loading with import parameters such as cycle time, number of data points per cycle, displacement, dwell time, and shape of displacement curve pictured.
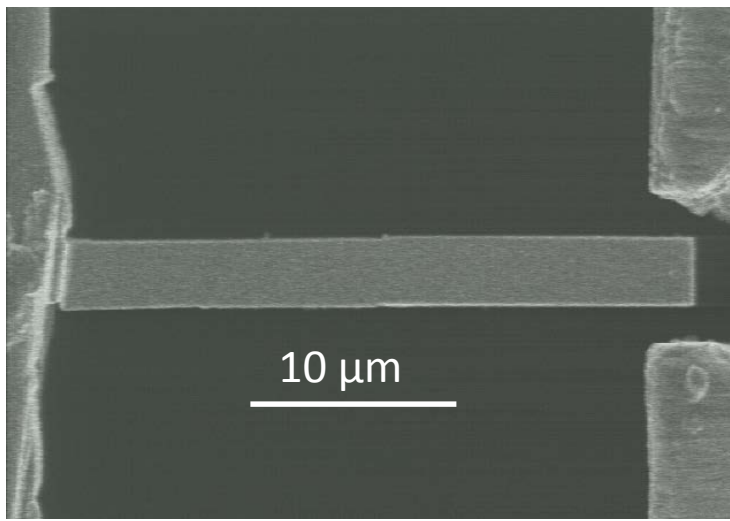
Figure 3.2.4c Aligned bending sample and gripper before loading
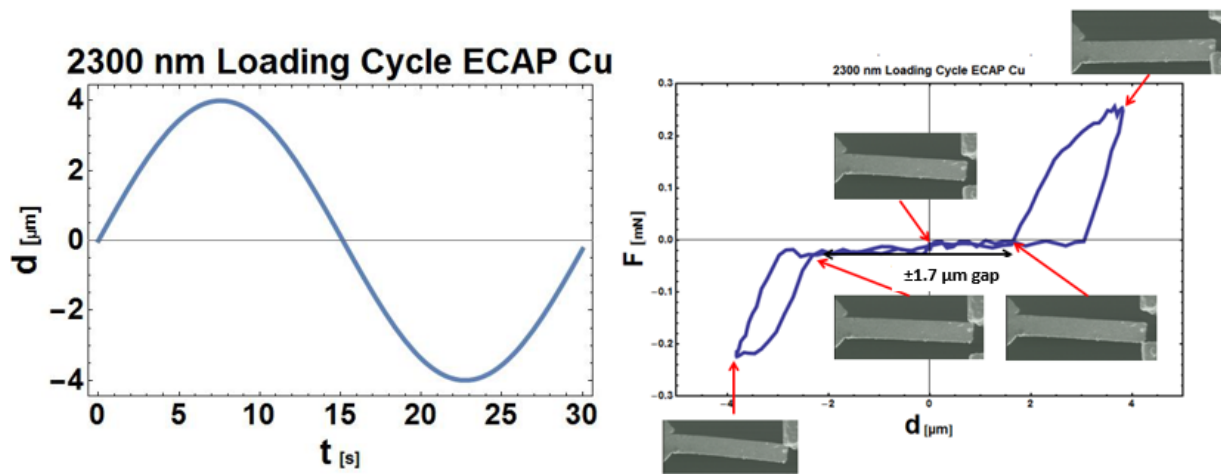
Figure 3.2.4c Representative displacement versus time graph for a single bending cycle, left, and measured load versus displacement data. The insets show SEM images taken in situ during the loading cycle to depict the contact at certain points along the cycle.

Tables 3.2.4 a through d below give the details of the nominal displacements and number of cyclic load cycles at each nominal displacement performed for each of the four micro fatigue bars. In general, the testing of each bar began with very small total displacements with a focus on obtaining at least 100 completely elastic cycles. After the initial step, the displacement was increased to the point where yielding occurred. Subsequently, approximately 100 yielding cycles were performed. After this, cycling occurred at higher displacements beyond yielding, also often in approximate 100 cycle batches for each larger displacement. This was done in order to assess the cyclic stability of the bars at each

displacement and do a quantitative assessment of mechanical properties on a cycle by cycle basis while also allowing for a cyclic stress-strain curve to be obtained by taking the data points at the tips of the stable cycles. Before an assessment of mechanical properties was performed, gap corrections for the points at which no contact between the gripper and sample occurred were performed in order to obtain cyclic loading curves that mirror those of macroscopic fatigue tests. A schematic representation of this correction for one cycle can be seen in Figure 3.2.4d.
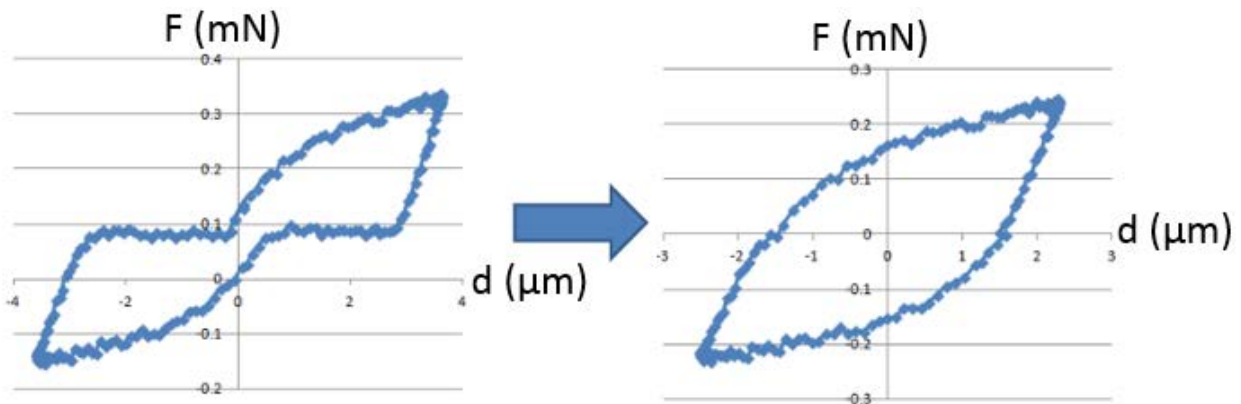
Figure 3.2.4d A schematic representation of a gap correction for one cyclic loading cycle. During non-contact points, zero force occurs. Each hysteresis loop was also centered with respect to displacement by taking the average of its minimum and maximum displacement values at each half cycle and either adding or subtracting that average value from all points.

Table 3.2.4a Cyclic Loading Schedule of the Single Crystal Copper Fatigue Bar

Nominal Displacement Amplitude (nm)	Number of Cycles
500	104
750	1
1000	1
1250	1
1500	103
2500	102

Table 3.2.4b Cyclic Loading Schedule of the ECAP Copper Fatigue Bar

Nominal Displacement Amplitude (nm)	Number of Cycles
350	104
750	1
1000	1
1250	1
1400	1
1600	102
1800	102
2100	102
2300	102
2500	101

Table 3.2.4c Cyclic Loading Schedule of the Single Crystal PM 2000 Fatigue Bar

Nominal Displacement Amplitude (nm)	Number of Cycles
300	100
800	1
1000	1
1200	102
1700	102
2200	102
2500	100

Table 3.2.4d Cyclic Loading Schedule of the HPT PM 2000 Fatigue Bar

Nominal Displacement Amplitude (nm)	Number of Cycles
300	103
600	1
900	1
1200	1
1500	1
1800	1
2100	1
2400	1
2700	1
3300	1
3600	20*

*fatigue fracture occurred after the 20th cycle

3.2.5 Mechanical Properties Analysis

The gap corrected load-displacement curves were then converted to stress-strain curves in order to extract mechanical properties as a function of cycle number and amplitude. This process can be explained through Figure 3.2.5a and the equations below. The linear elastic loading portions of each cycle were fit to determine elastic modulus values. For cycles with plastic deformation, the first point which deviated from linear elastic loading was taken to be the yield strength. The maximum stress values for each cycle were recorded as well as the maximum strain values and their associated stresses from stable hysteresis loops in order to generate cyclic stress strain curves for each of the four micro fatigue bars. In addition the energy dissipation of each loading cycle was calculated by performing trapezoidal integration of the area within the stress strain curve.
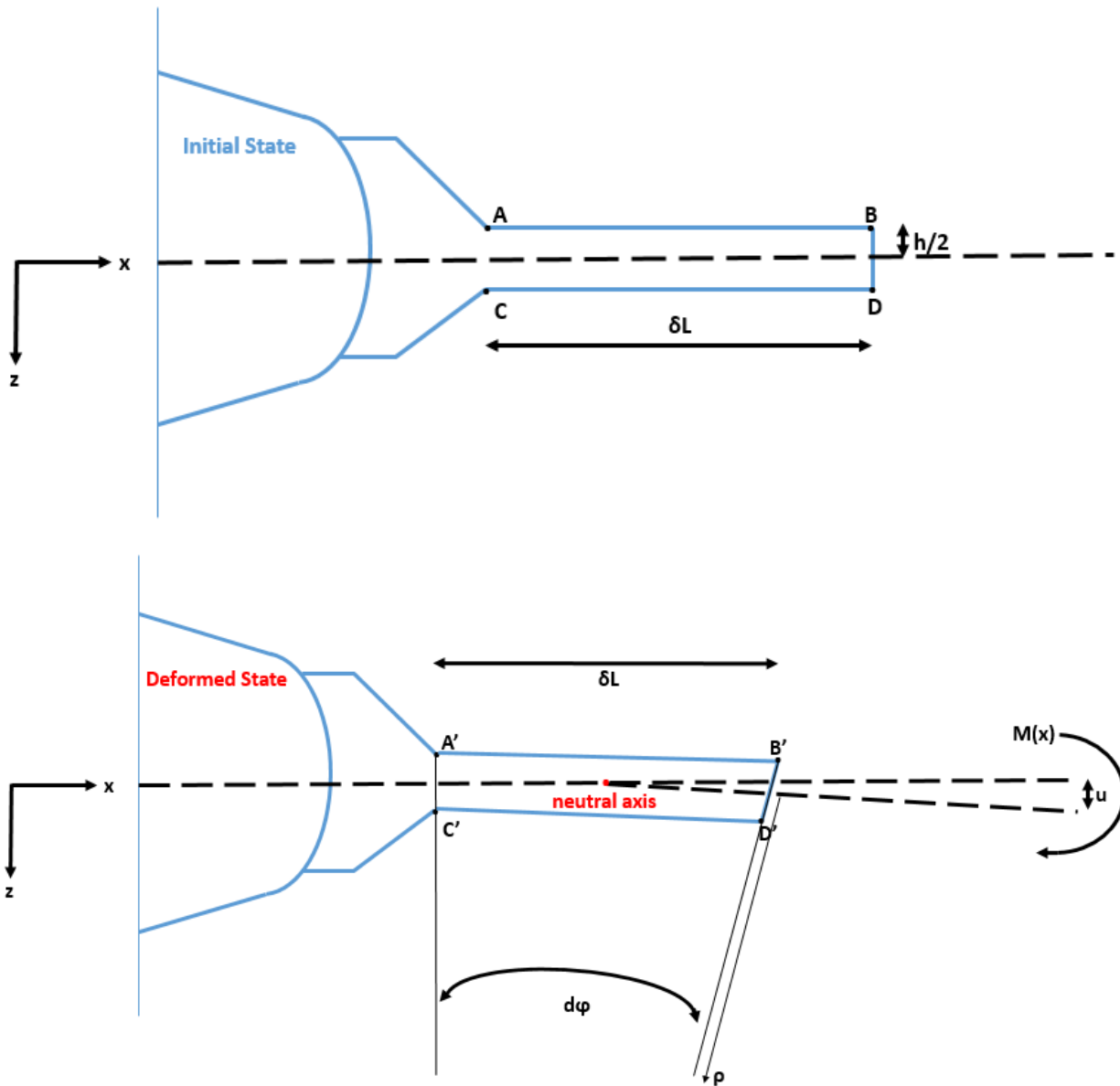
Figure 3.2.5a Sketch of a micro fatigue bar in its initial state and deformed state. After bending, the length of the neutral axis remains the same. The edges formed by the segments AB and CD experience tensile and compressive stresses as seen when they become segments A'B' and C'D' in the deformed state. A'B' is longer than the original length δL, but C'D' is shorter. The displacement of the ASMEC UNAT SEM II is represented by u and the distance from the neutral axis to the edge represented by h/2, $d\phi$ is the bend angle, and ρ is the radius of curvature. From these parameters, the strain at point A/A' in the y direction can be calculated as shown below.

In linear elastic beam theory and during our fatigue bend tests, it is assumed that pure bending occurs and that a linear stress distribution occurs along the length of the bar. However, in reality plastic deformation will cause very complicated stress-strain states to occur. Beginning with these assumptions the strain at the root at the outer edge can be derived from basic principles as follows:

$$\varepsilon = \frac{\Delta l}{l_o} = \frac{l - l_o}{l_o} = \frac{A'B' - AB}{AB} \tag{3.1}$$

where Δl is the change in length and l_o is the original length of the bar and the rest are length segments shown in Figure 3.2.5a. The length of the top edge of the beam in the deformed state can be obtained from its curvature, κ.

$$\kappa = \frac{1}{\rho} \tag{3.2}$$

which the inverse of its radius of curvature. As seen in Figure 3.2.5a, the radius of curvature is related to the bend angle and length of the bar by:

$$\tan(d\phi) = \frac{\delta L}{\rho} \tag{3.3}$$

The length of the outer edge in the deformed state is

$$A'B' = \left(\rho + \frac{h}{2}\right) \tan(d\phi) \tag{3.4}$$

where h/2 is the distance from the neutral axis to the edge. After substituting for the radius of curvature (3.3 into 3.4) a more useful equation arrives:

$$A'B' = \left(\frac{\delta L}{\tan(d\phi)} + \frac{h}{2}\right) \tan(d\phi) = \delta L + \frac{h}{2}\tan(d\phi) = \left(1 + \frac{h}{2\rho}\right)\delta L \tag{3.5}$$

Next, substituting into 3.1 gives:

$$\varepsilon = \frac{\left(1 + \frac{h}{2\rho}\right)\delta L - \delta L}{\delta L} = \frac{h}{2\rho} \tag{3.6}$$

Let it also be noted that the bend angle is related to the displacement recorded by the micromechanical system by:

$$\tan(d\phi) = \frac{u}{l_b} \tag{3.7}$$

where l_b is the bending length of the bar meaning the distance between the root of the bar and the point at which the bar is clamped by the gripper. By substituting for ρ and $\tan(d\phi)$, the final equation for strain at the root of the bar at the edge of the bar is:

$$\varepsilon = \frac{u\,h}{2\,\delta L\,l_b}$$
(3.8)

where u is the displacement recorded, h/2 is half of the thickness of the bar, δL is the length of the bar, and l_b is the previously described bending length of the bar.

When a linear stress distribution along the length of the bar is assumed, the stress at the root on the edge of the bar arrives much more directly. Fundamentally, it is related to the bending moment along the neutral axis and moment of inertia as follows:

$$\sigma = \frac{M}{I}\frac{h}{2} = \frac{F\,l_b}{\frac{b\,h^3}{12}}\cdot\frac{h}{2} = \frac{6F l_b}{b\,h^2}$$
(3.9)

3.2.6 Microstructural Evolution

The microstructural evolution of both PM 2000 fatigue bars and the ECAP Cu fatigue bar was monitored in order to determine if any grain coarsening or changes in grain orientation would occur as a result of the various stages of cyclic deformation by performing EBSD scans of the bars in their initial state and after various levels of deformation. For the single crystal PM 2000 bar, this was done after its 2200 nm and 2500 nm nominal displacement amplitude stages. Unfortunately, for the HPT PM 2000 bar, the grain size was too small for clear identification by EBSD. However, an upper bound on the initial grain size could be taken as shown in Figure 3.2.6b. For the ECAP Cu bar this was done after the 1600 nm, 1800 nm, 2100 nm, and 2500 nm nominal displacement amplitude stages. Initial microstructural investigations of the polycrystalline materials via FIB imaging and EBSD can be seen below in Figure 3.2.6a and Figure 3.2.6b. The ECAP Cu has an approximate average initial grain size of 195 ± 53 nm. A bimodal grain distribution can be seen with smaller subgrains and areas of larger grains. This has been reported and described in detail by Valiev [116, 117].
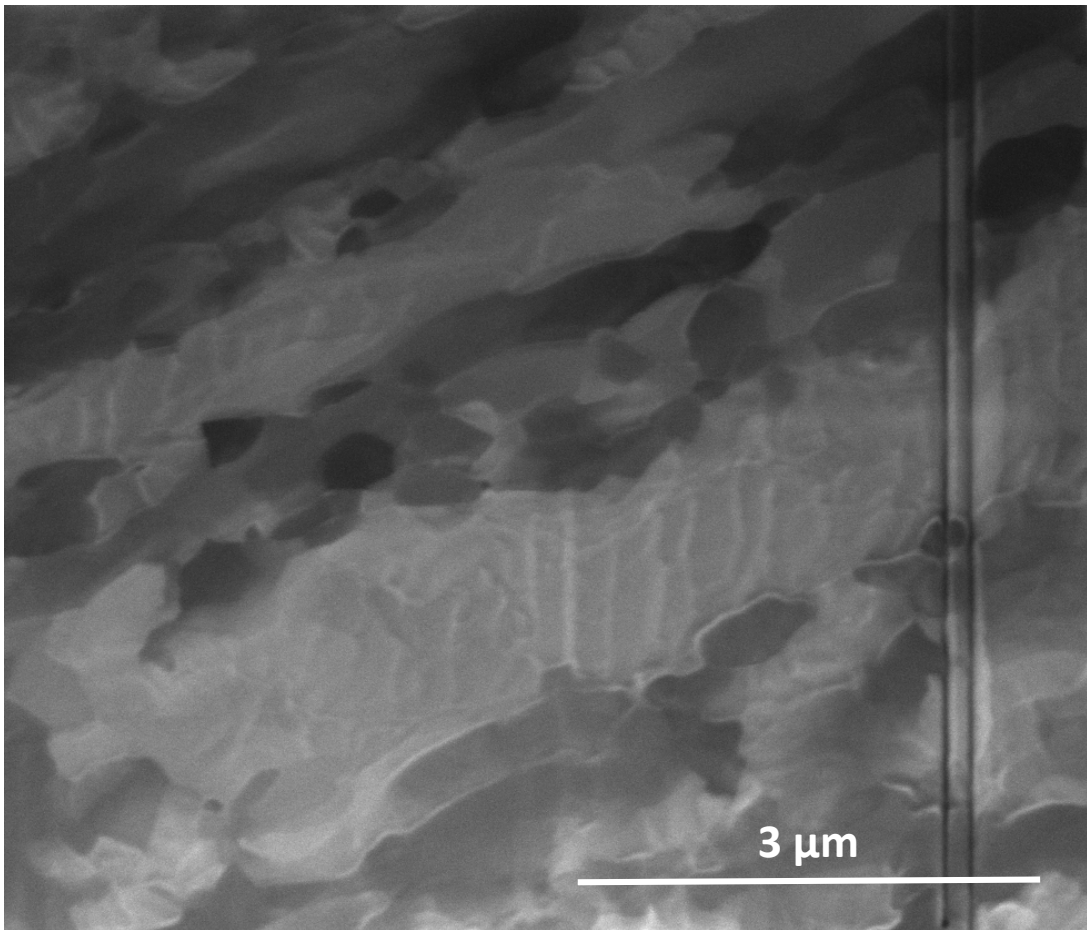
Figure 3.2.6a Initial microstructure of ECAP Cu measured by FIB imaging used to make one of the four micro fatigue samples. The grain size was measured to be 195 ± 53 nm, and a bimodal grain distribution is apparent.
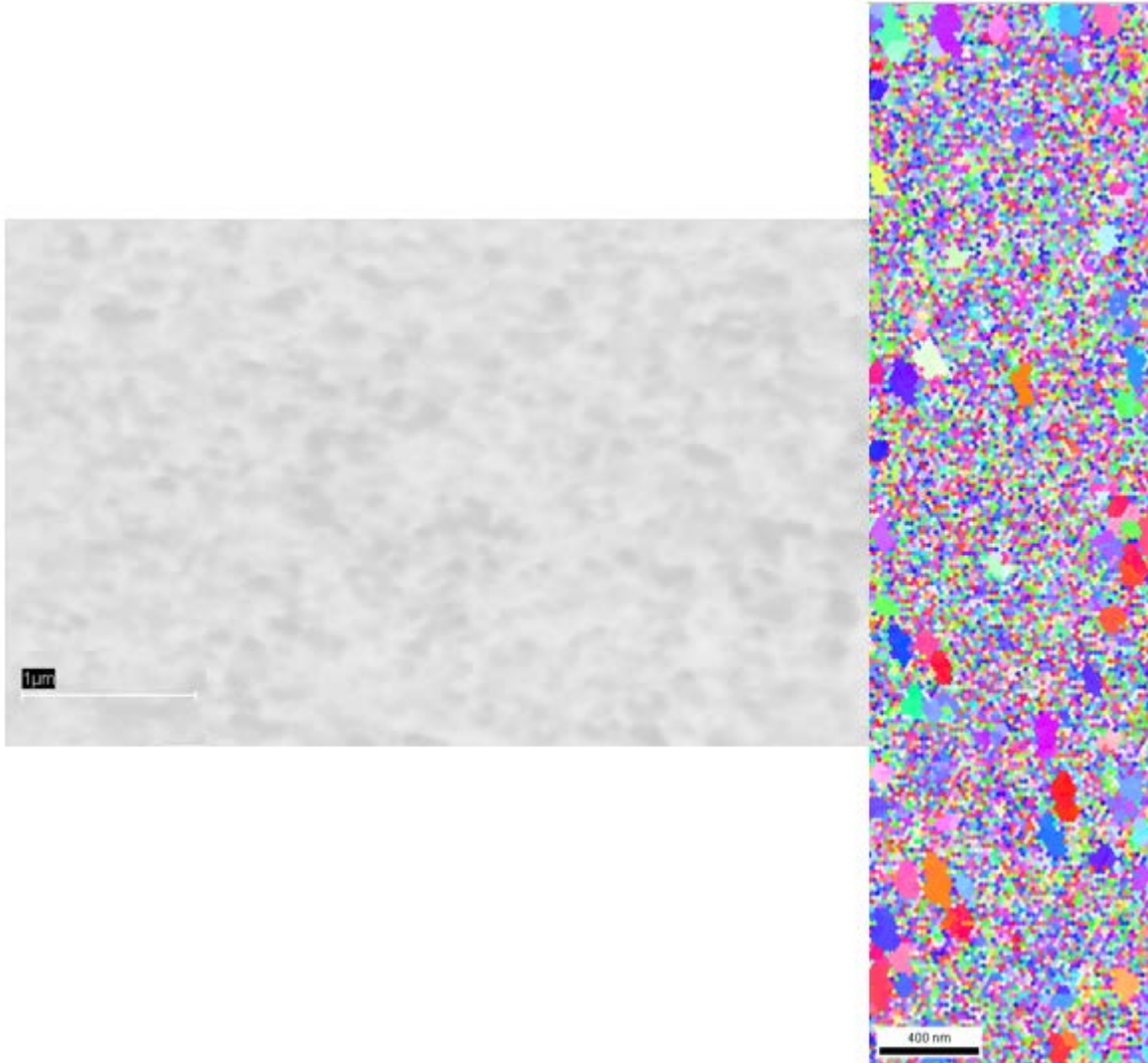
Figure 3.2.6b Initial microstructure of HPT PM 2000 after 26 turns which was used to fabricate a micro fatigue bar. A FIB image of the grains can be seen on the left and an EBSD scan can be seen on the right. The visible grains by EBSD can be taken to constitute an upper limit on the grain size of this specimen to be 86 ± 24 nm.

4. Results and Discussion

4.1 Cu-Nb Alloys

4.1.1 HPT Processing

During HPT processing of the Cu-Nb alloys, torque vs. time data were recorded for all tests. When a constant torque level has been reached, the sample is assumed to be saturated meaning no further hardening will occur and the microstructure has reached a steady state. Figure 4.1.1 shows the torque vs. number of turns data for three representative RT tests. As expected, the powder mixture containing more copper reaches a higher torque, 176 Nm compared to 125 Nm, during processing because the amount of niobium increases the sample's hardness significantly. We see that steady states are reached after about 10 turns. Some tests were purposely stopped before this occurred like the 75Cu-25Nb example shown in order to study the hardness increase and HPT effects. The oscillation of the graph can be attributed to roughness of the HPT anvils that are not perfectly round and should not be attributed to microstructural changes.
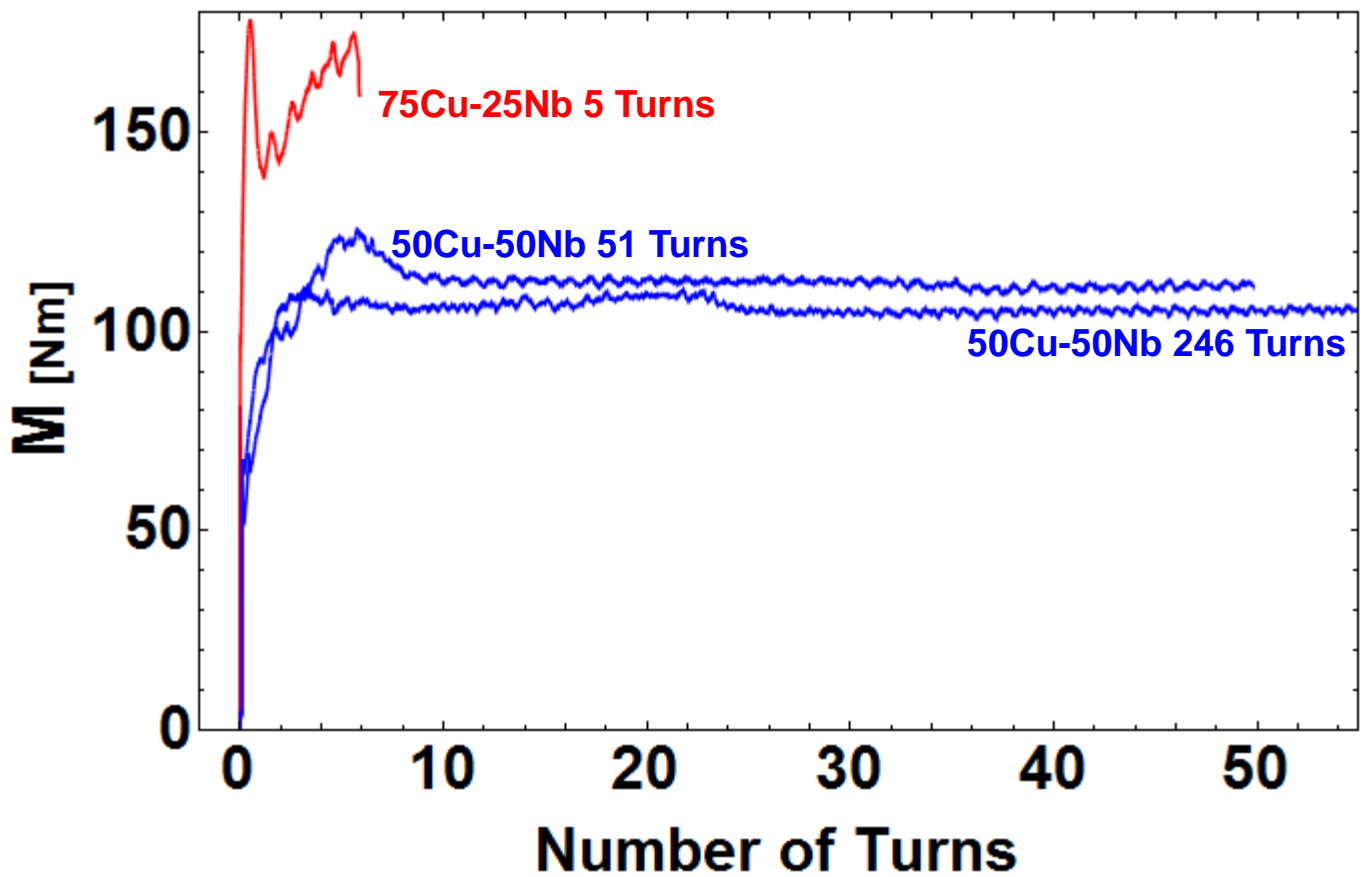
Figure 4.1.1 Diagram displaying torque versus number of turns graphs of Cu-Nb alloys that were processed with different powder compositions for different numbers of revolutions.

4.1.2 Microhardness

For an examination of materials properties and homogeneity all samples were examined by performing Vickers hardness radially across the disks as previously described in sections 3.1.4 and 3.1.5. The samples have been divided into 3 bins: 50-50 compositions that have been ball milled for 17 hours and then underwent at least 10 revolutions of HPT, the single sample with a 75-25 composition ball milled for 40 hours that underwent 5 revolutions, and 50-50 compositions ball milled for 17 hours that underwent 5 or less revolutions in the HPT at various temperatures. The first set contains hardness profiles that are highly irregular. These disks became extremely brittle and often flaked apart when mounted. Possible causes could be attributed to contamination from the stainless steel balls getting mixed into the powders. Optical micrographs can be seen in Figure 4.1.2a and a radial hardness plot can be seen in Figure 4.1.2b.
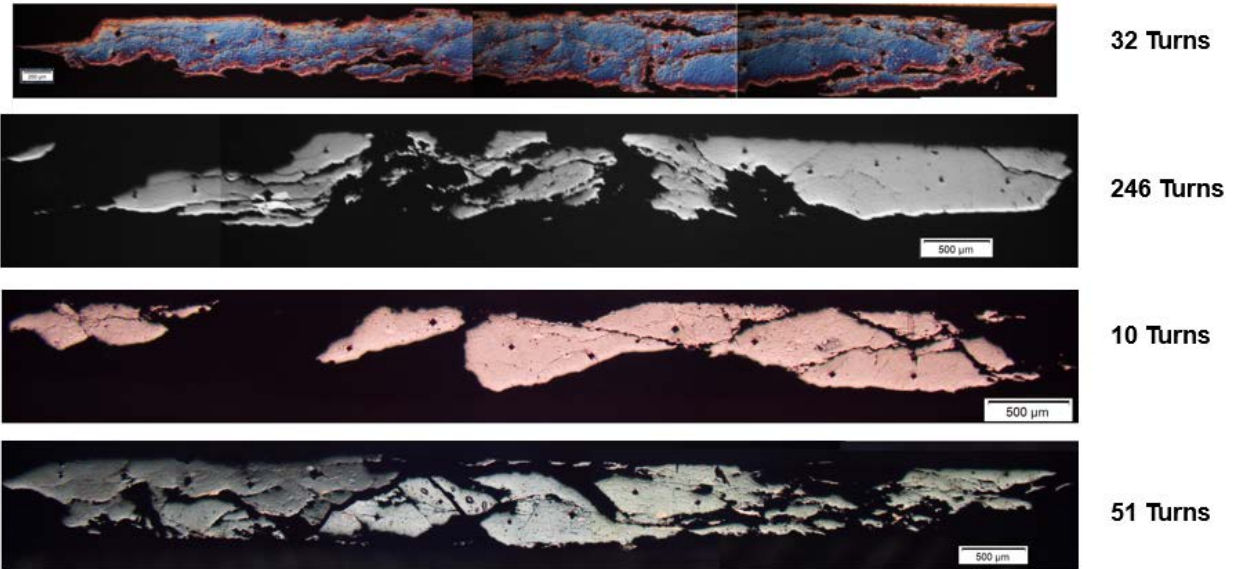
Figure 4.1.2a Optical micrographs of 50-50 Cu-Nb alloys ball milled for 17 hours that were processed by 10 or more revolutions at RT. The disks have become very brittle.
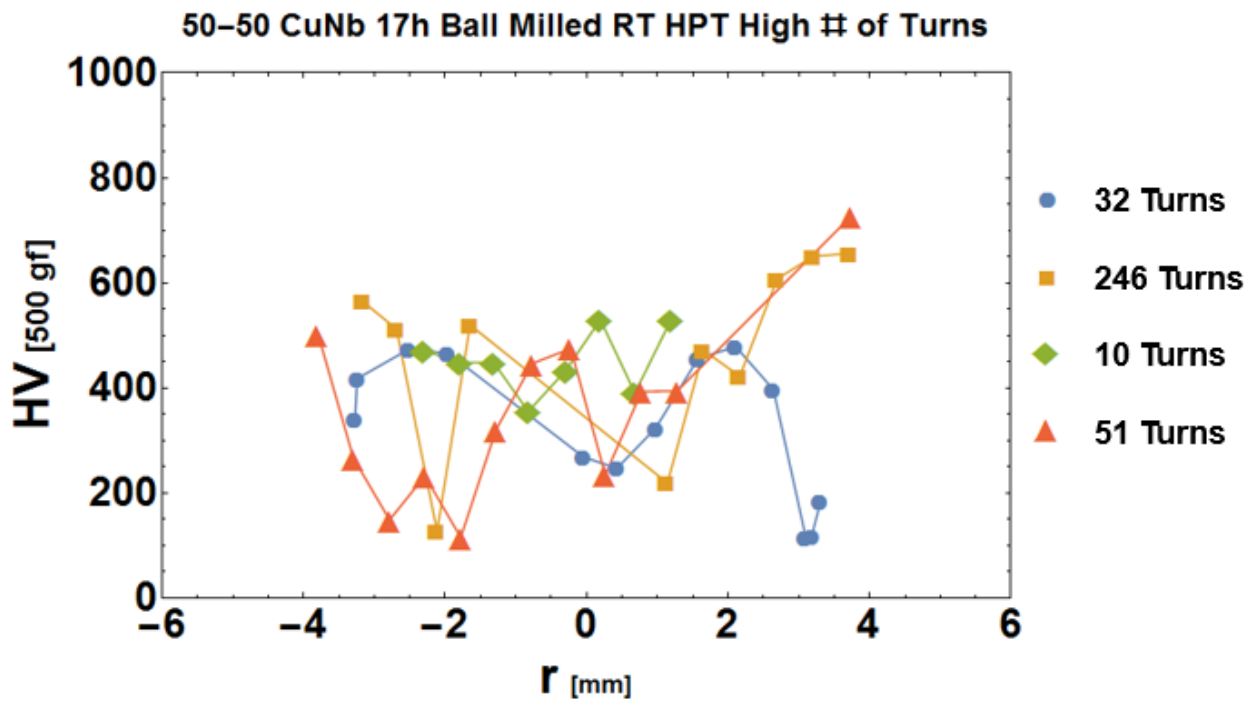

Figure 4.1.2b Hardness profiles of 50-50 Cu-Nb alloys ball milled for 17 hours that were processed by 10 or more revolutions at RT. The hardness profiles are highly irregular due to the disks becoming extremely brittle at this stage.

The single sample with a 75-25 composition ball milled for 40 hours that underwent 5 revolutions is once again very brittle. However, it maintains a hardness profile around 200 HV between ±4 mm. Then, the hardness jumps up to about 500 HV outside of this radial distance. Deformation at the edges during the HPT process is much more intense than at the center during stages below saturation where more shear occurs at larger radial distances. This could explain the 300 HV difference. The optical micrograph and radial hardness profile for this sample can be seen in Figures 4.1.2c and 4.1.2d.

Figure 4.1.2c Optical micrograph of 75-25 Cu-Nb composition ball milled for 40 hours that underwent 5 HPT revolutions. Again the center appears very brittle and a significant amount of material has flaked away.
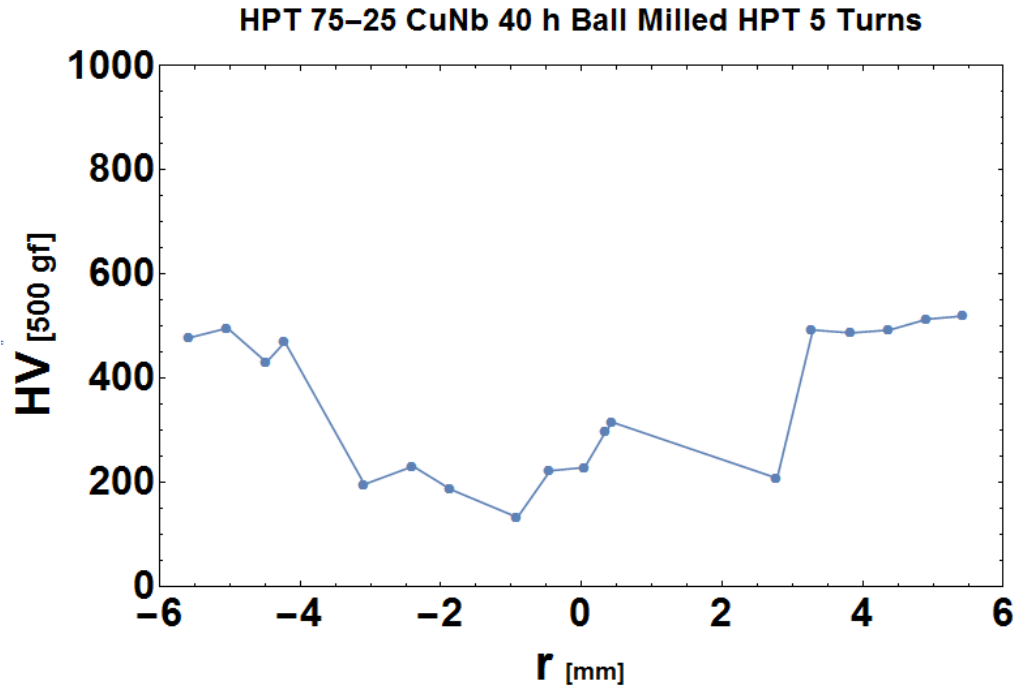
Figure 4.2.1d Hardness profile of 75-25 Cu-Nb composition ball milled for 40 hours that underwent 5 HPT revolutions. Regions between 4 and 6 mm from the center of the disk appear to have a steady hardness of 500 HV, whereas the central region has a hardness of 200 HV. This difference can be attributed to more shear occurring at the edges because the material never reached a steady-state saturated microstructure.

The 50-50 compositions ball milled for 17 hours that underwent 5 or less revolutions in the HPT at various temperatures appear much more cohesive as seen by the optical micrographs in Figure 4.2.1e. The hardness profiles can be seen in Figure 4.2.1f. The hardness profiles appear to be relatively constant for all HPT tests performed at elevated temperatures. However, there is an increase in hardness with temperature. The average hardness of the 170 ℃ sample is 462 HV, the 200 ℃ is 530 HV, and the 250 ℃ is 600 HV. Perhaps the elevated temperature increased deformation pathways and allows the Cu-Nb to reach saturation much faster as a function of increasing temperature. We see that the one turn test performed at RT still remains unsaturated. This can be seen by the dip from 500 HV at the edges farther than two or 3 mm away from the center down to 300 HV at the center. Once again, this can be attributed to more initial shear occurring at the edge of the sample due to higher torque there than in the center.
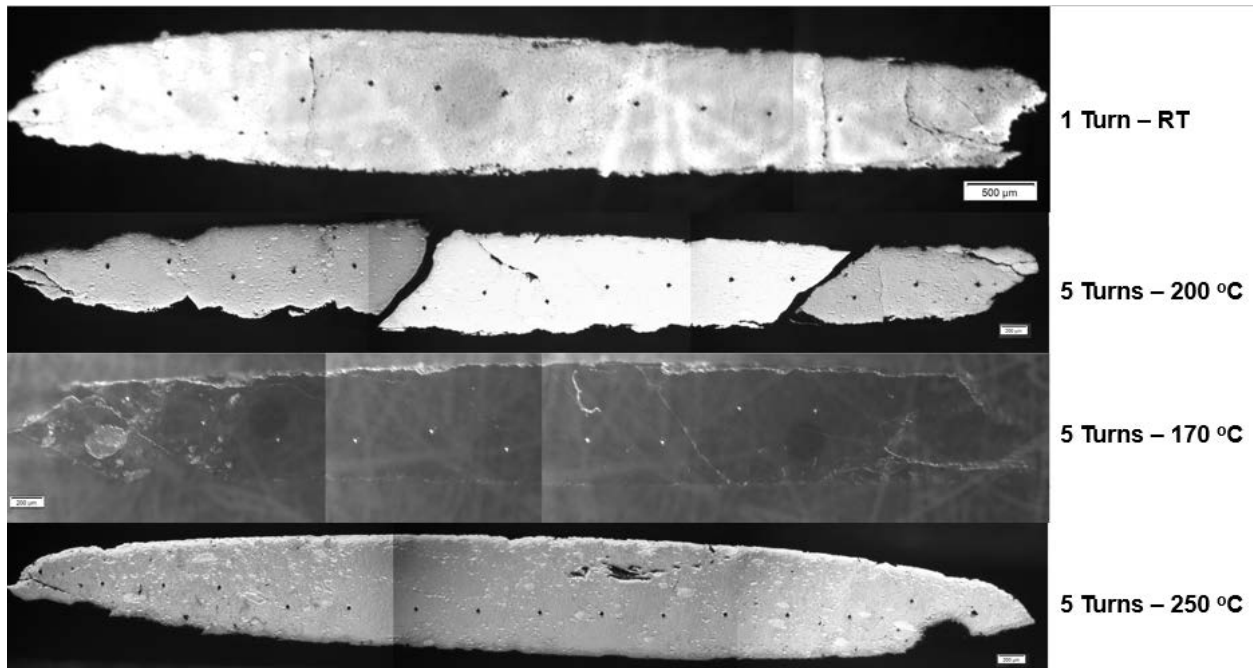
Figure 4.2.1e Optical micrographs of 50-50 compositions ball milled for 17 hours that underwent 5 or less revolutions in the HPT at various temperatures as noted in the figure. These disks appear much more cohesive. Fracture only occurred in the one disk where HPT was performed at 200 °C.
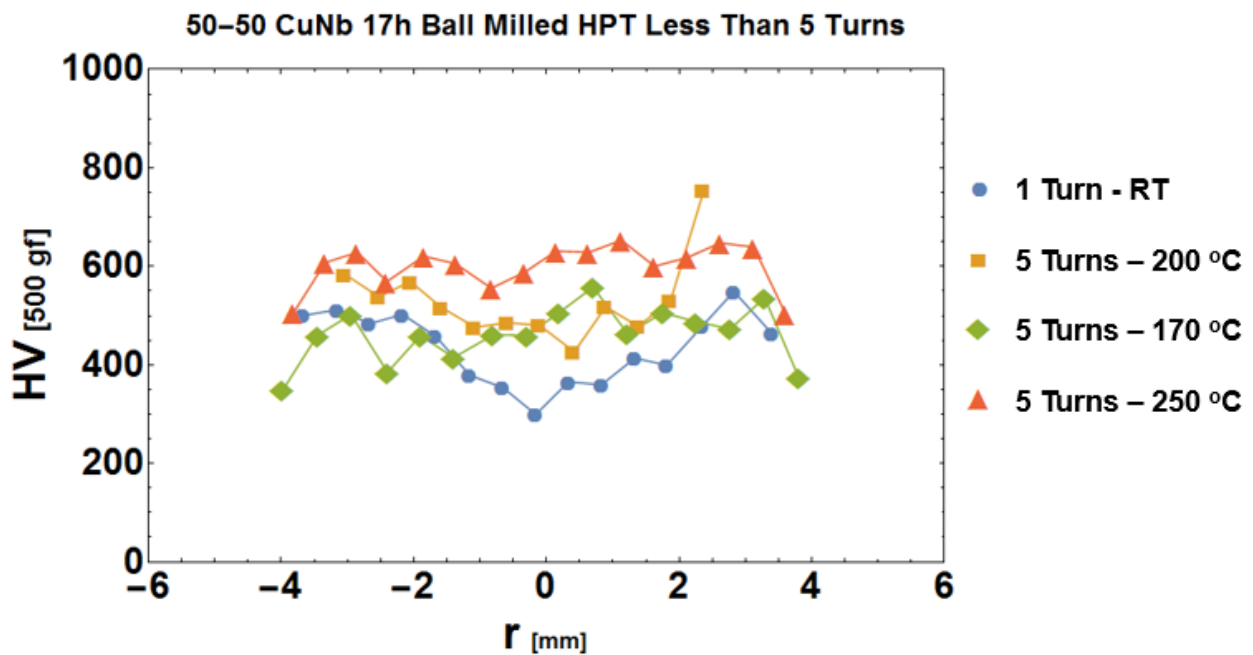
Figure 4.2.1f Hardness profiles of 50-50 Cu-Nb alloys ball milled for 17 hours that were processed by 5 or less revolutions at various temperatures.

4.2 Microfatigue Bend Bars

4.2.1 Single Crystal Copper
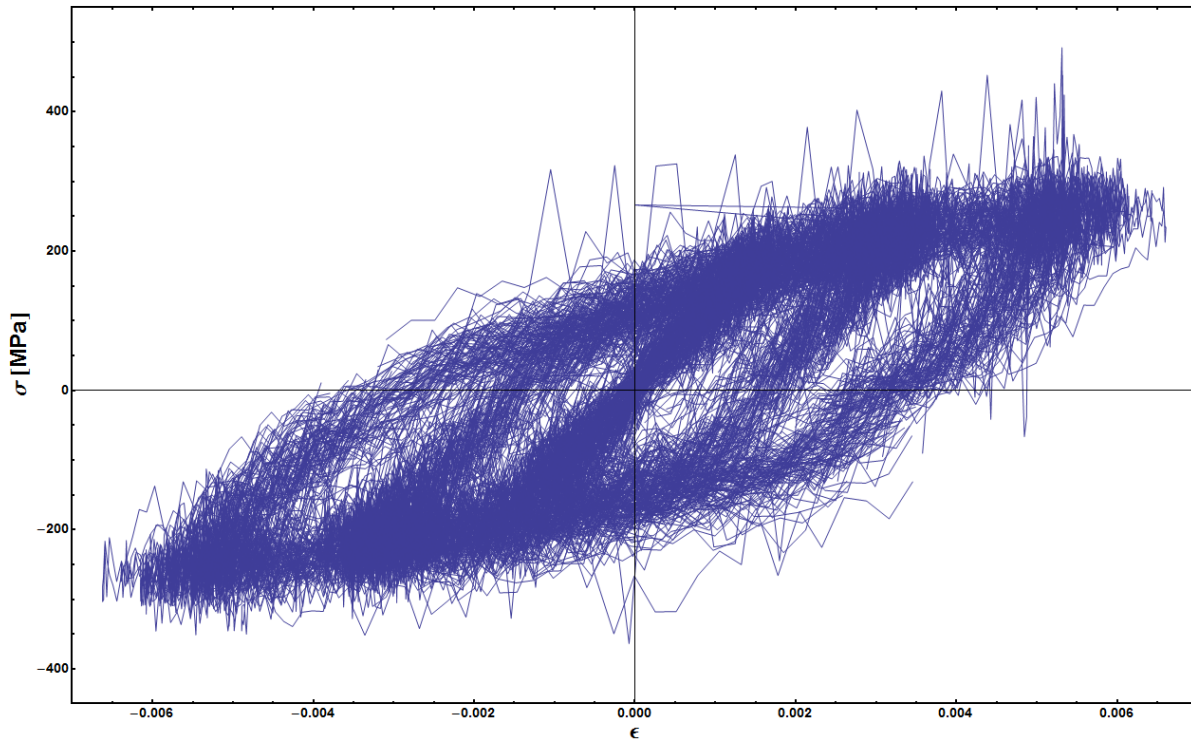
Figure 4.2.1a Stress-strain curves of all cycles for the single crystal micro fatigue bar reported in Table 3.2.4a

Elastic Region

As noted in Table 3.2.4a, there were 104 cycles performed at a nominal displacement of 500 nm. All of these cycles were deemed to be purely in the elastic deformation regime. After measurements of the bending length during these cycles were made as well as previously described corrections, the stress-strain curves for these cycles can be seen in Figure 4.2.1b. These curves were fit to a linear regression where the slope can be taken as the elastic modulus. This value is 114 GPa, which is well in agreement with the accepted literature value (110-128 GPa) reported in Table 2.1.
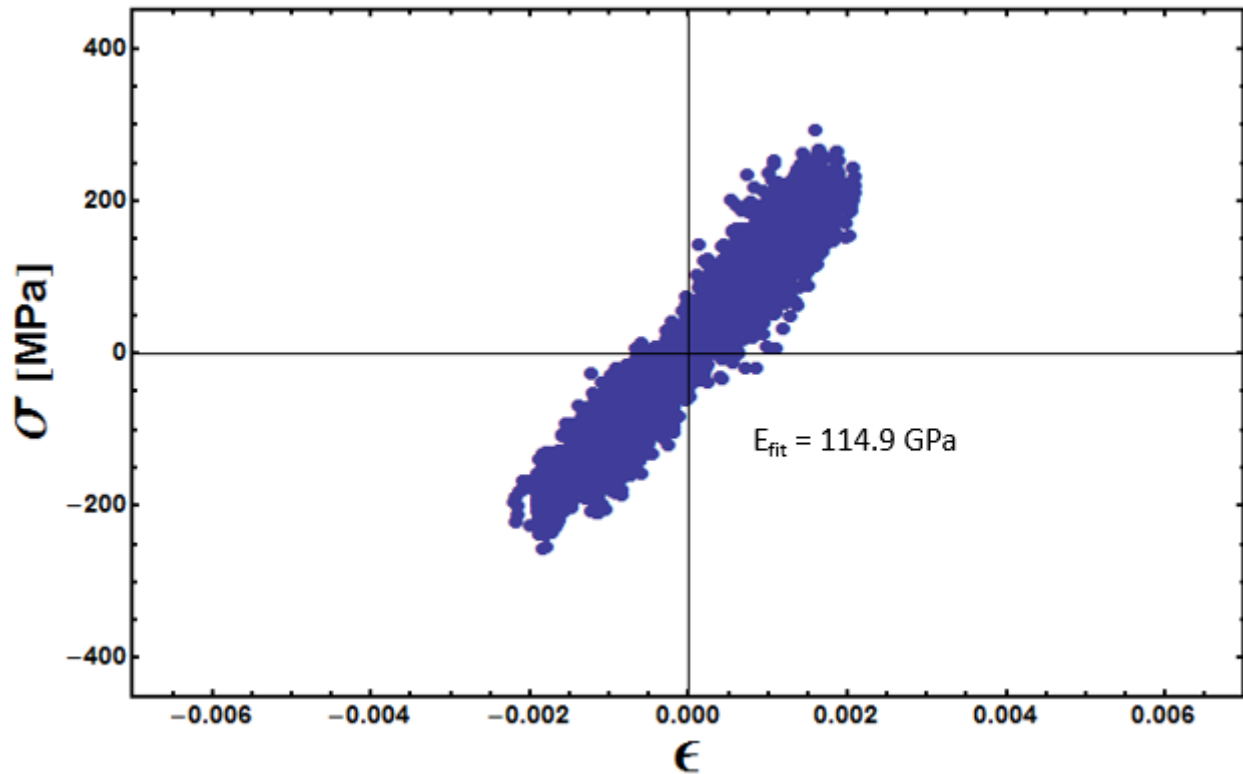
Figure 4.2.1b Purely elastic cyclic loading of the single crystal copper micro fatigue bar.

The 103 cycles performed at 1500 nm nominal displacement were deemed to be "yielding cycles" at which point in time a clear yielding point was established. However, after post-processing, the stress-strain curves for nominal displacements between 750 nm and 1250 nm also showed evidence of plastic deformation and were evaluated for yield points as well. Yield points were measured every half cycle and their magnitudes were plotted as a function of cycle number for each amplitude (Figure 4.2.1d) to determine cyclic stability as well as versus amplitude (Figure 4.2.1e). The same was done for elastic moduli and maximum stress at every half cycle (Figure 4.2.1c). In addition the maximum strain values of every cycle were taken from stable cycles at each amplitude and combined with the purely elastic cycles to produce a cyclic stress-strain curve (Figure 4.2.1f). Finally, the energy dissipated per cycle was plotted as a function of cycle number and amplitude (Figures 4.2.1 g and h).
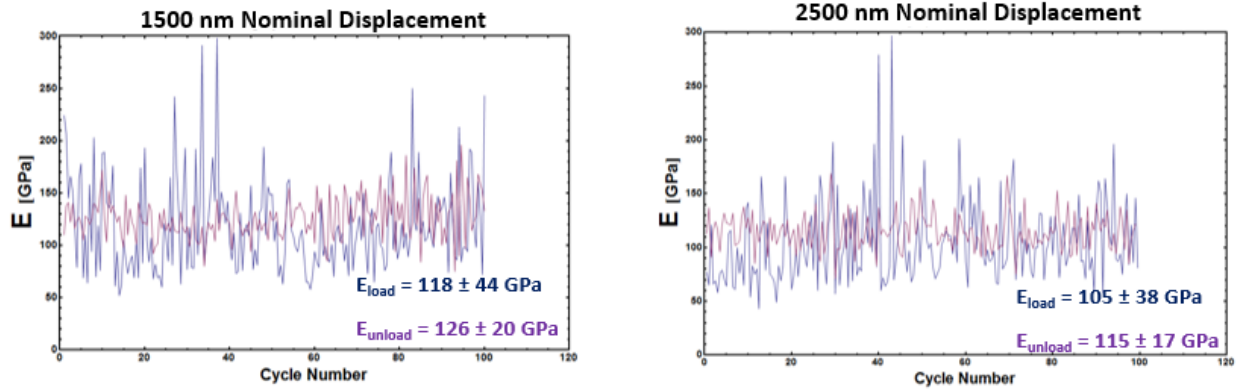
Figure 4.2.1c Elastic moduli as a function of cycle number for 1500 nm and 2500 nm nominal displacements. Both the loading and unloading moduli agree with literature values. There appears to be cyclic stability with respect to elastic modulus with the exception of a few irregular cycles (~ cycle numbers 30 and 35 for 1500 nm nominal displacement and ~ cycle number 40 for 2500 nm nominal displacement).
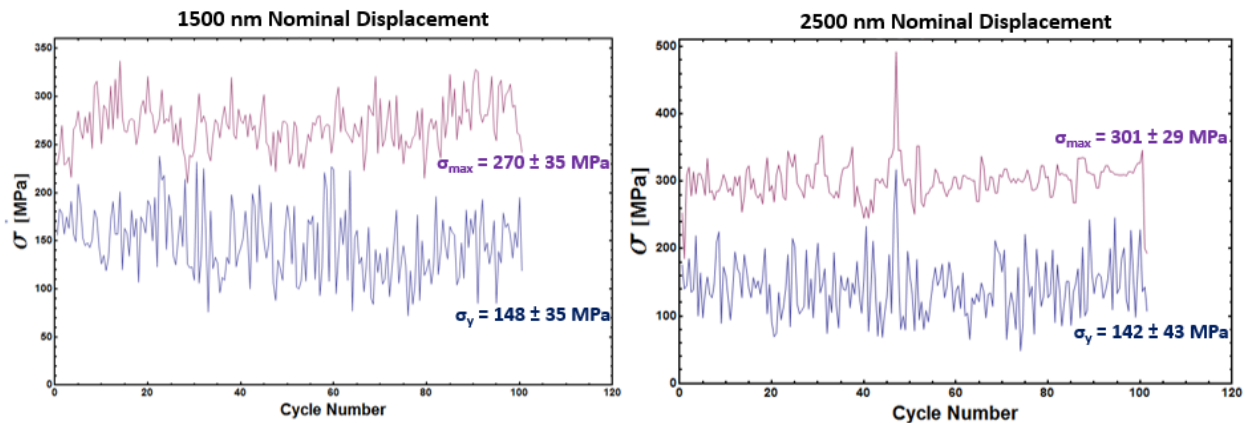
Figure 4.2.1d Cyclic stability of the single crystal copper micro fatigue bar occurs for nominal displacements up to 2500 nm. The yield strength values remain constant between 140 and 150 MPa whereas the added micron of nominal displacement increases the maximum stress by 30 MPa.

97
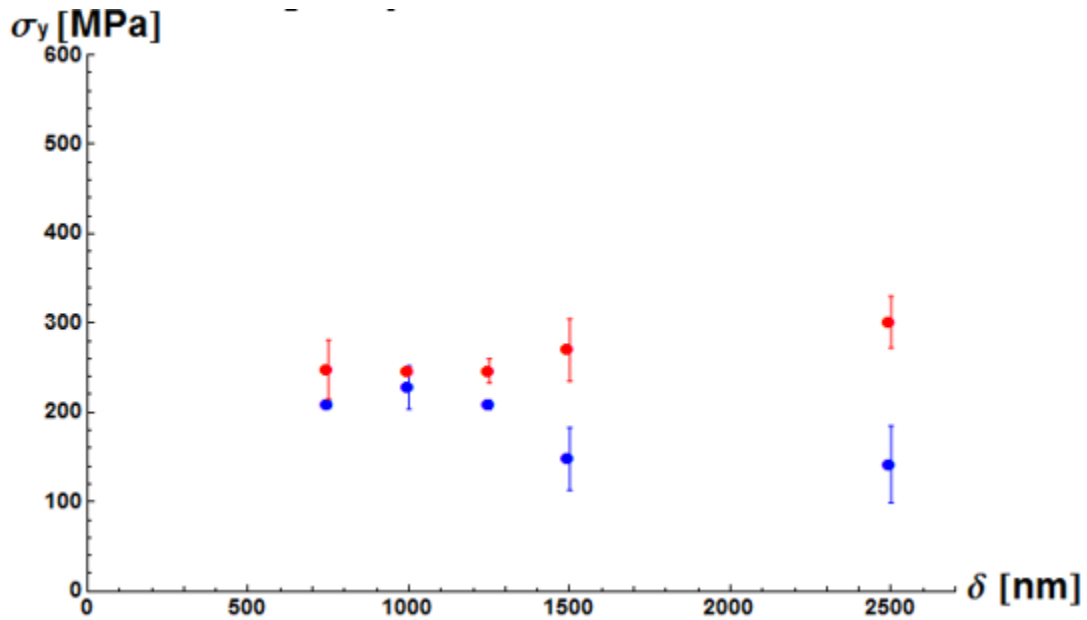
Figure 4.2.1e Stress evolution of the single crystal copper micro fatigue bar as a function of increasing amplitude. When the yield points for lower amplitudes, less than 1500 nm nominal displacement are considered, 60 MPa of softening in yield strength over the course of testing occurs, and practically all occurs when increasing the amplitude from 1250 nm to 1500 nm displacement. Maximum stress values incur a gradual increase of 30 MPa over this sample amplitude range.
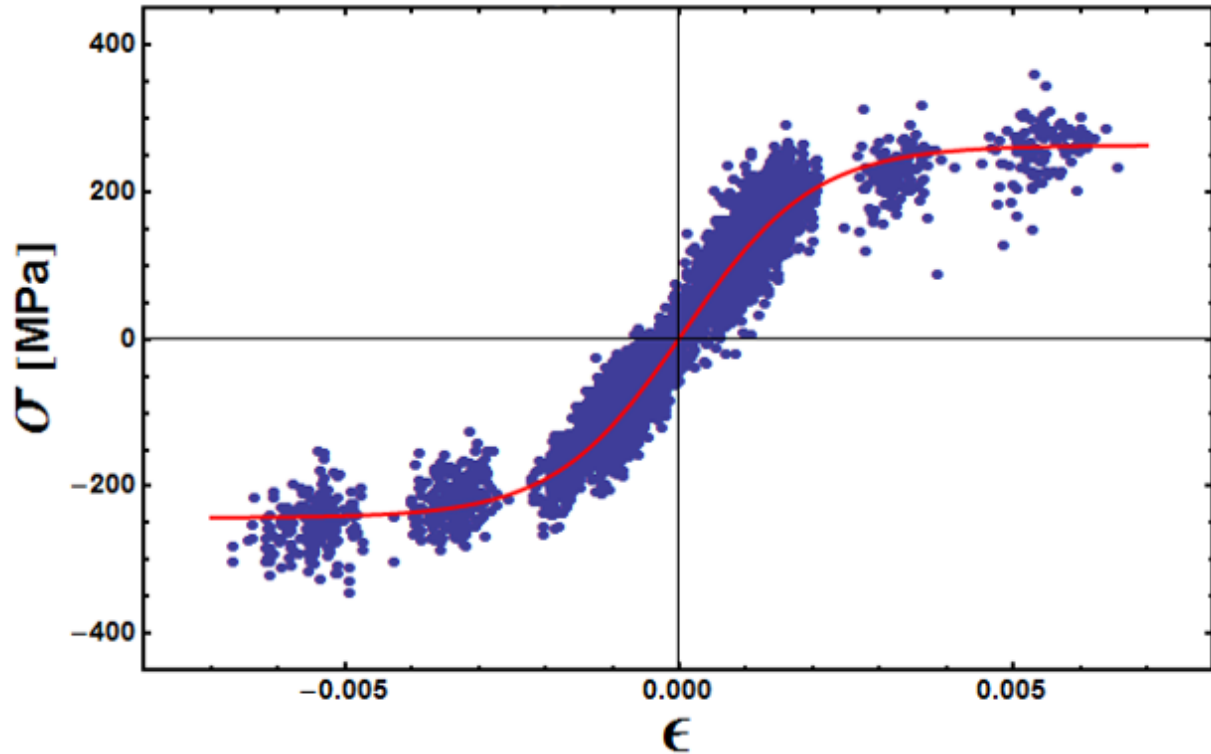
Figure 4.2.1f The cyclic stress-strain curve for the single crystal micro fatigue bar indicative of the cyclic stability seen in Figure 4.2.1a. There is no evidence of and cyclically induced work hardening or work softening as a function of plastic strain amplitude for $\varepsilon_{pl} < 7$ x 10^{-3}. This is in agreement with the plateau region described by Mughrabi in [108]. However, the plateau region for this micro fatigue bar is bounded by $1.5 < \varepsilon_{pl} < 7$ x 10^{-3}. The plateau is not reached until higher plastic strain amplitudes that the value of 6 x 10^{-5} reported in [108].
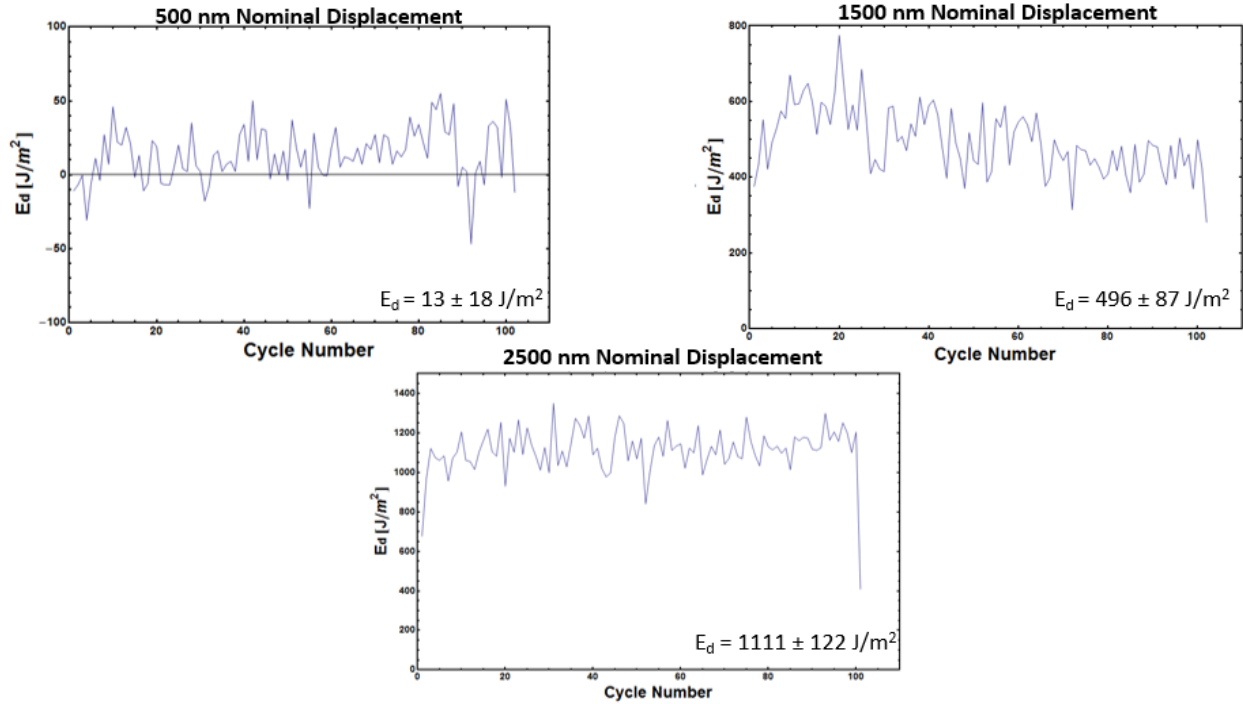
Figure 4.2.1g Cyclic evolution of the energy dissipated per cycle at three nominal displacements. The first, 500 nm, on the upper left is in the purely elastic regime as evidenced by the fact that no energy is dissipated during cycling. In the upper left, 1500 nm nominal displacement, the energy dissipated per cycle peaks at cycle number 20 and very gradually decreases. Cyclic stability of the energy dissipated per cycle occurs for the largest amount of plastic deformation, 2500 nm nominal displacement.
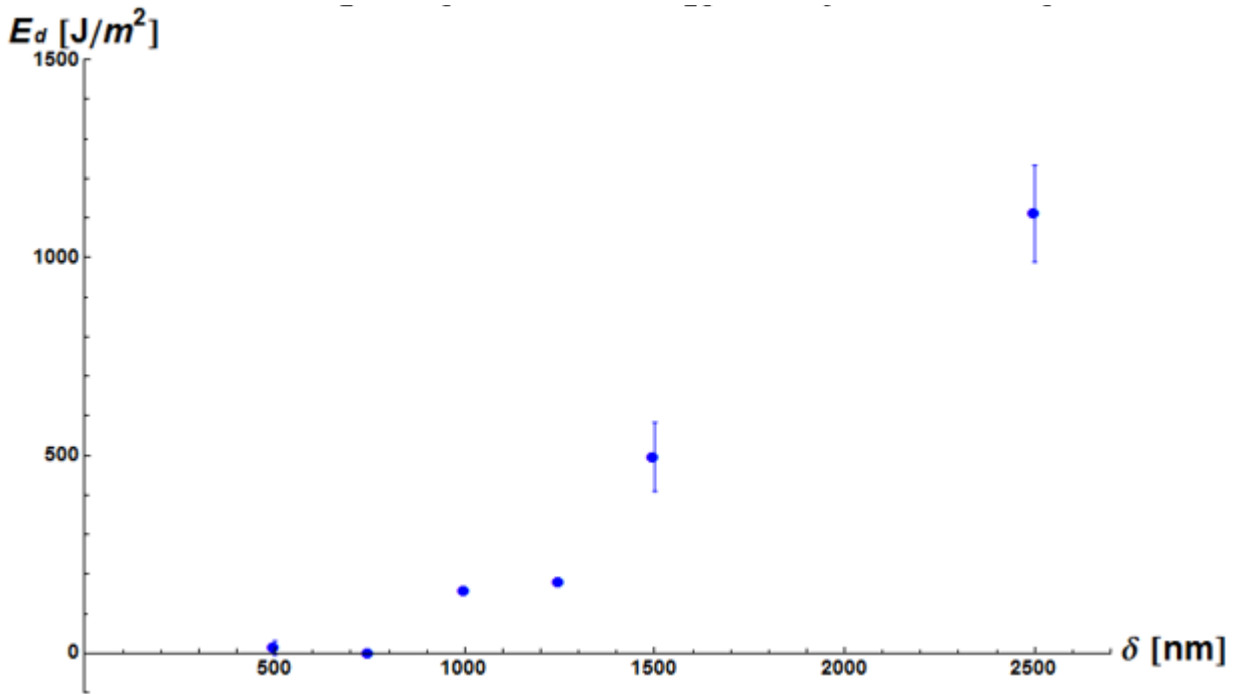
Figure 4.2.1h The energy dissipated per cycle as a function of displacement amplitude. It is evident that no energy is released until displacement amplitudes are greater than 750 nm, equivalent to strain amplitudes of 1.5×10^{-3}. A relatively constant amount of energy is dissipated between displacement amplitudes of 1250 and 1500 nm comparable to strain amplitudes of 2×10^{-3}.

4.2.2 ECAP Copper
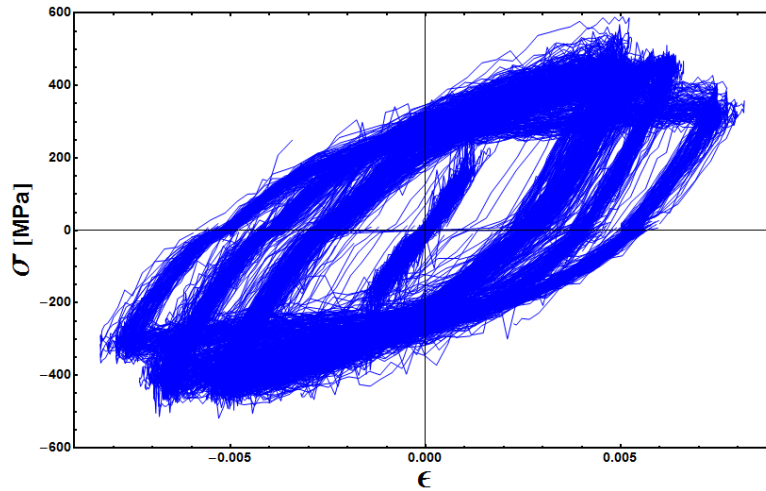
Figure 4.2.2a Stress-strain curves of all cycles for the ECAP copper micro fatigue bar reported in Table 3.2.4b

As noted in Table 3.2.4b, there were 104 cycles performed at a nominal displacement of 350 nm. All of these cycles were deemed to be purely in the elastic deformation regime. After measurements of the bending length during these cycles were made as well as previously described corrections, the stress-strain curves for these cycles can be seen in Figure 4.2.2b. These curves were fit to a linear regression where the slope can be taken as the elastic modulus. This value is 142 GPa.
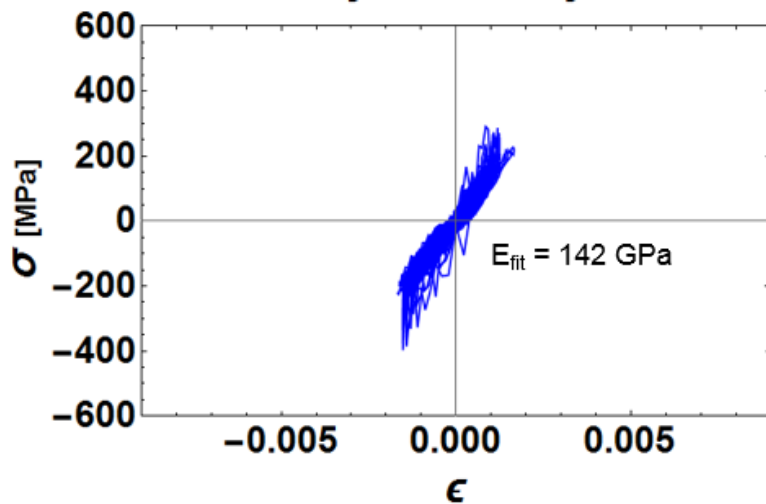
Figure 4.2.2b Purely elastic cyclic loading of the ECAP copper micro fatigue bar.

The 102 cycles performed at 1600 nm nominal displacement were deemed to be "yielding cycles" at which point in time a clear yielding point was established. However, after post-processing, the stress-strain curves for nominal displacements between 750 nm and 1400 nm also showed evidence of plastic deformation and were evaluated for yield points as well. Yield points were measured every half cycle and their magnitudes were plotted as a function of cycle number for each amplitude (Figure 4.2.2d) to determine cyclic stability as well as versus amplitude (Figure 4.2.2e). The same was done for elastic moduli and maximum stress at every half cycle (Figure 4.2.2c). In addition the maximum strain values of every cycle were taken from stable cycles at each amplitude and combined with the purely elastic cycles to produce a cyclic stress-strain curve (Figure 4.2.2f). Finally, the energy dissipated per cycle was plotted as a function of cycle number and amplitude (Figure 4.2.2 g).
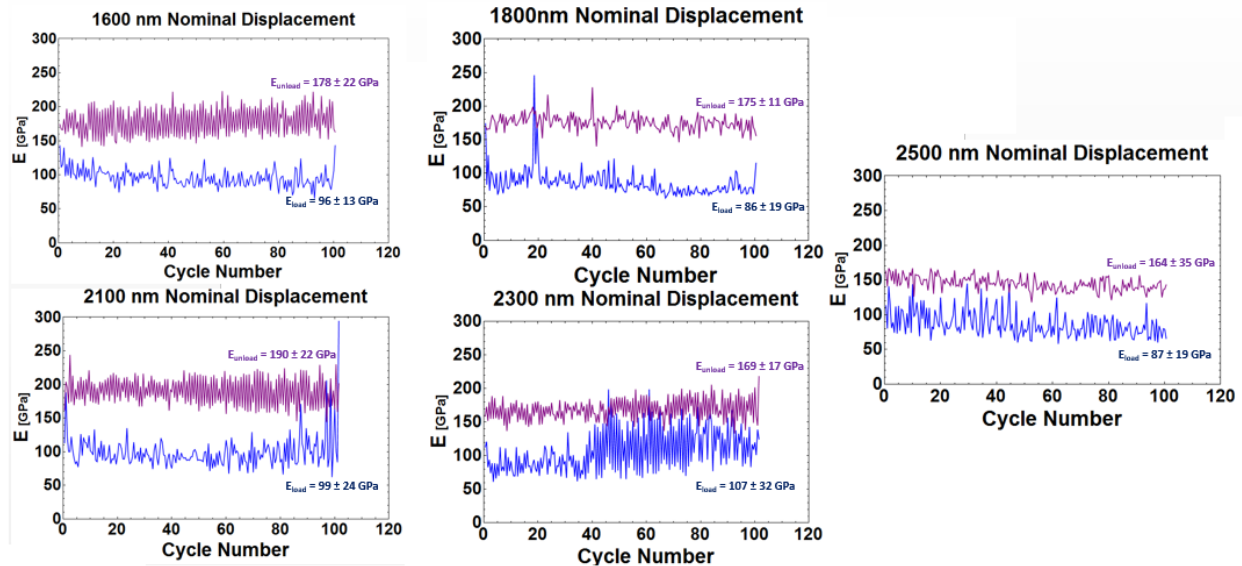
Figure 4.2.2c Elastic moduli as a function of cycle number for various displacement amplitudes. Note that the linear elastic unloading portions are always greater than the loading portions. Cyclic stability occurs at all amplitudes. Averaging all measurements gives a value of 135 GPa, which is reasonable for UFG copper.
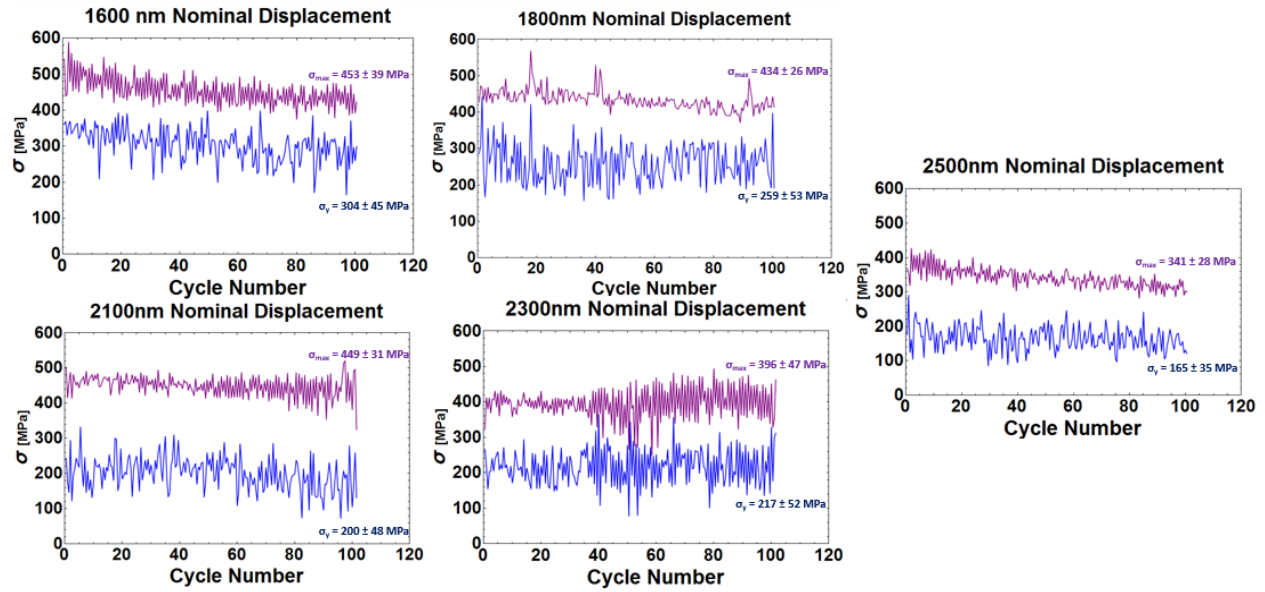
Figure 4.2.2d The yield strength and maximum stress values for the ECAP copper micro fatigue bar at various amplitudes. Gradual softening occurs at nominal displacements of 1600 nm for both yield and maximum stresses but only for maximum stress at 2500 nm. In between both stress values remain cyclically stable.
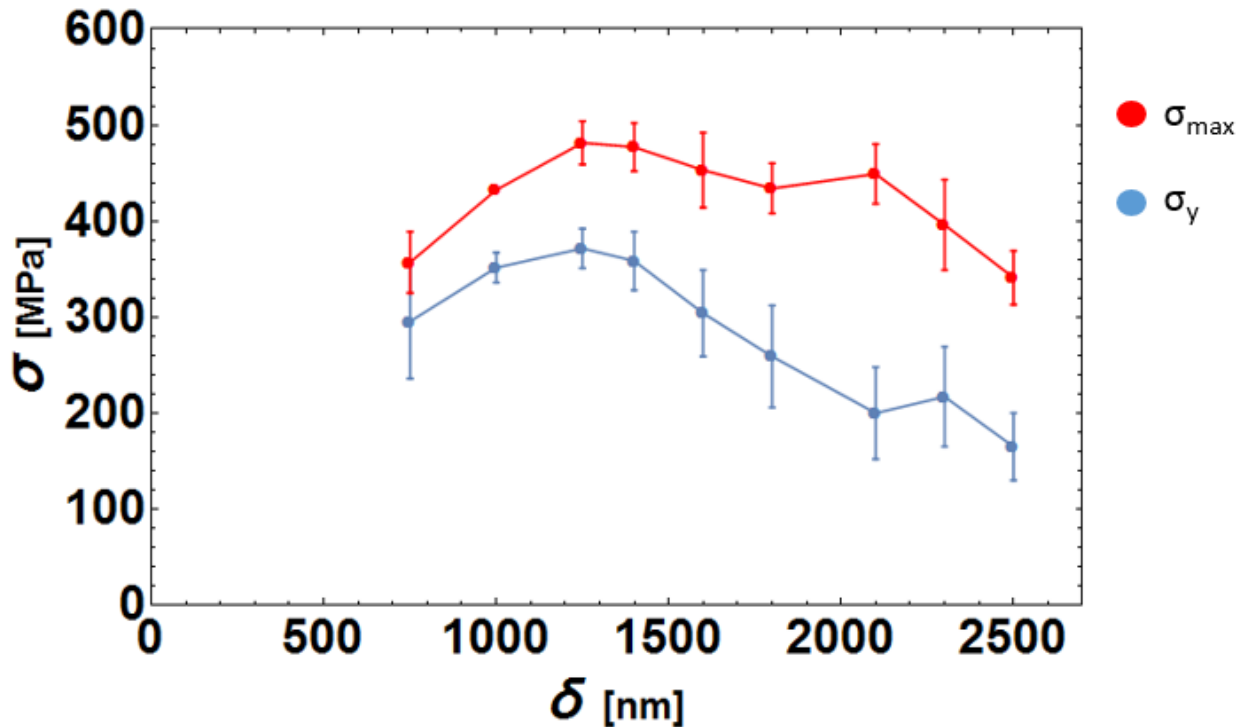
Figure 4.2.2e Stress evolution of the ECAP copper micro fatigue bar as a function of increasing amplitude. There appears to be an initial hardening regime with stress increases of about 200 MPa at smaller plastic amplitudes up to 1250 nm nominal displacement at which point the material becomes saturated with defects and then softening occurs to the extent where the ECAP copper's yield strength has been compromised past 1600 nm nominal displacement. The yield strength of the ECAP copper measured by macroscopic tensile tests for this sample was measured to be 334 ± 8 MPa. The 1600 nm nominal displacement yield point values agree with this to within one standard deviation.
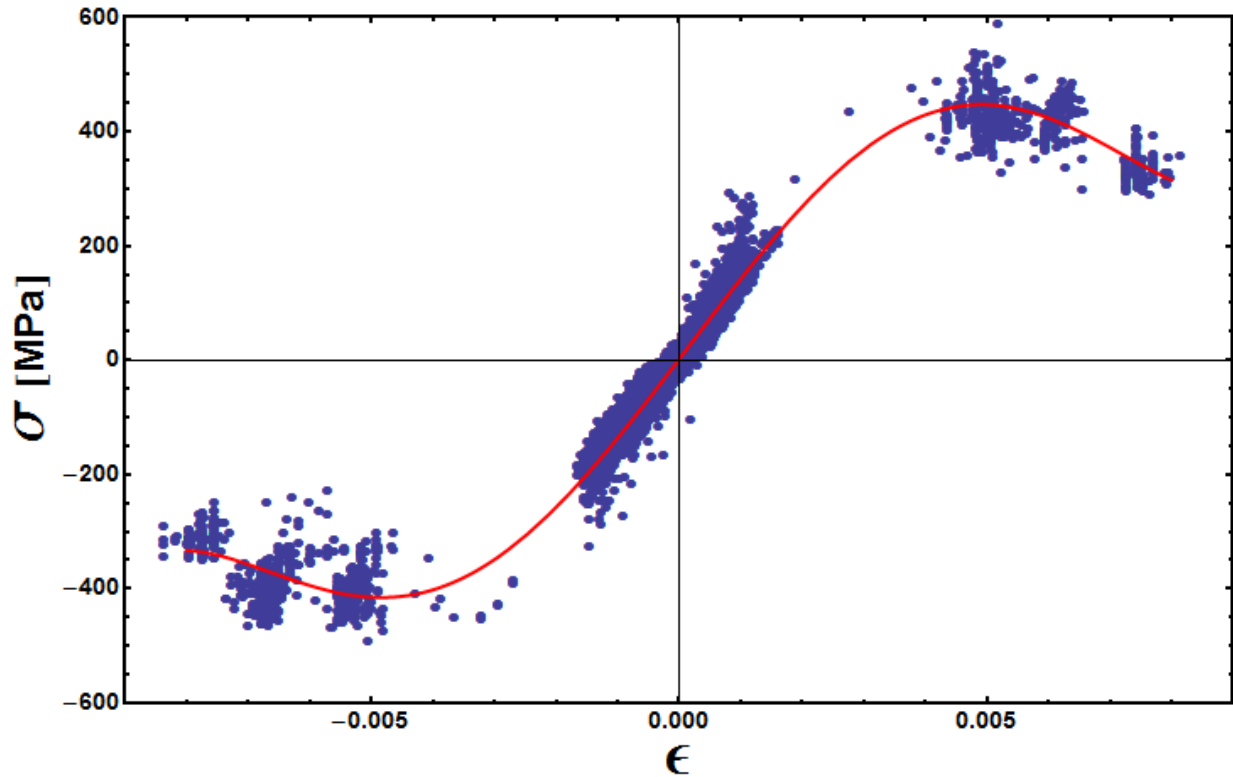
Figure 4.2.2f The cyclic stress strain curve of the ECAP Cu fatigue bar. A peak stress of 450 MPa occurs at a strain of 5 x 10^{-3}. At strains below this value, it is believed that cyclic hardening takes place, whereas for strains below this value, cyclic softening takes place.

$E_{d\,2500\,nm} = 1972 \pm 120\ J/m^2$
$E_{d\,2100\,nm} = 1924 \pm 157\ J/m^2$

$E_{d\,2300\,nm}$

$E_{d\,1600\,nm} = 1272 \pm 89\ J/m^2$
$E_{d\,1800\,nm} = 1185 \pm 141\ J/m^2$

$E_{d\,350\,nm} = 6 \pm 6\ J/m^2$
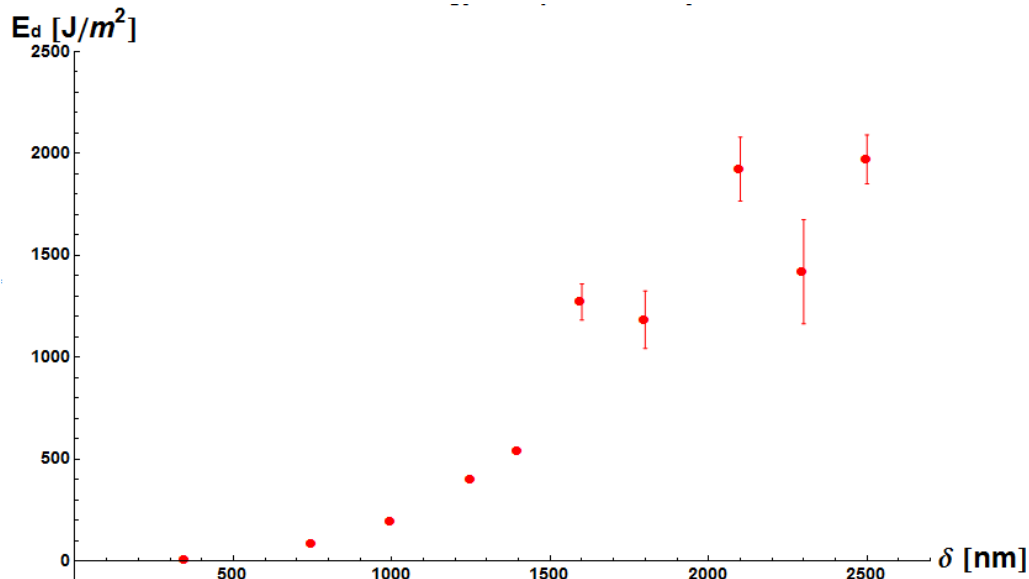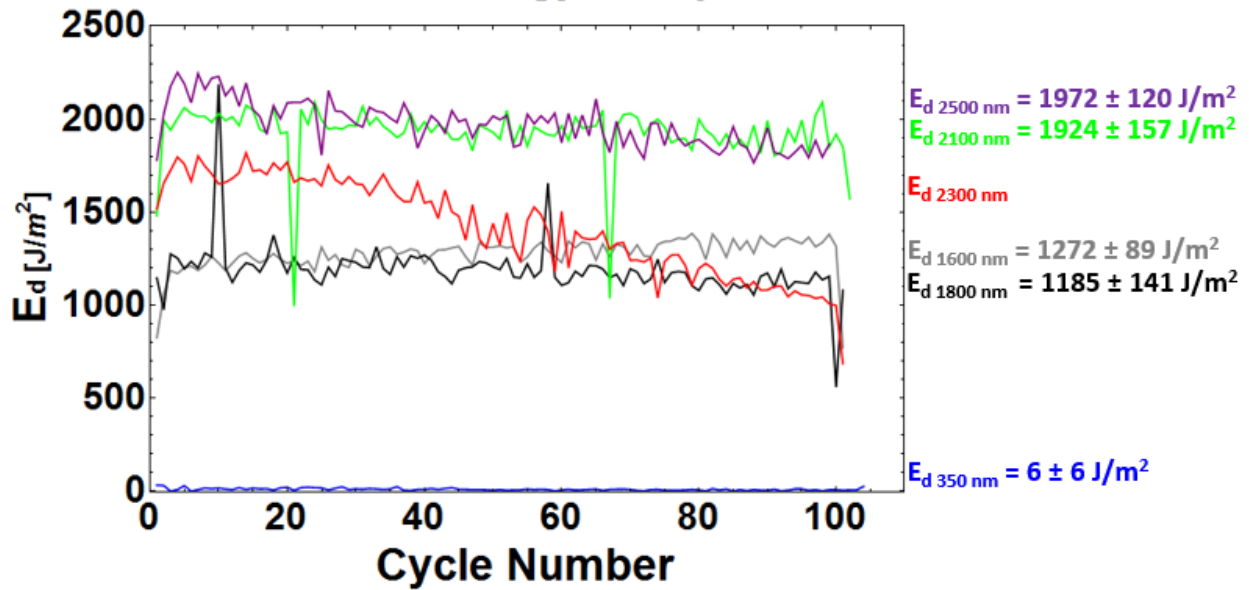
Figure 4.2.2g Energy dissipated per cycle for the ECAP copper micro fatigue bar. We see that at 350 nm nominal displacement no energy is dispersed, but relative cyclic stability occurs at 1600 nm and 1800 nm displacements. A slight drop in the energy dispersed occurs for 1800 nm, while for 1600 nm a slight increase occurs, both approximately 100-200 J/m². Cyclic stability again occurs at 2100 nm, but at 2300 nm we see a dramatic drop in the energy dissipated per cycle after 20 cycles. However, when the displacement was then ramped up to 2500 nm, the energy dissipated per cycle was restored back to its value at 2100 nm.

During cyclic loading of the ECAP copper fatigue bar, the Bauschinger effect had become very exaggerated for nominal displacements of 1800 nm or larger, meaning cycles that reached

$\varepsilon_{pl} \geq 7 \times 10^{-3}$. An example of the most extreme case of this can be seen in Figure 4.2.2h. The ratios of σ_y'/σ_y for this cycle is 0.48.
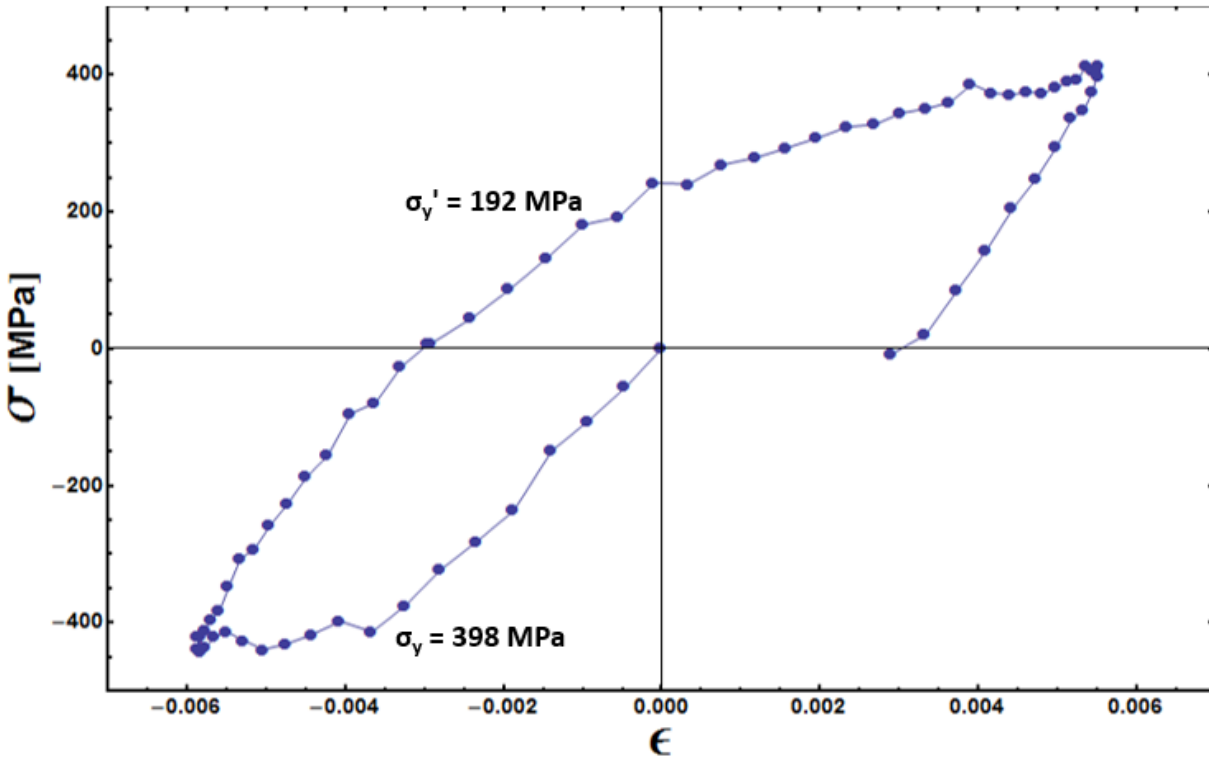
Figure 4.2.2h The most extreme case of the Bauschinger effect observed for an 1800 nm nominal displacement cycle for the ECAP copper micro fatigue bar. The ratio of σ_y'/σ_y for this cycle is 0.48.

Microstructural Evolution

EBSD scans were taken at the base of the ECAP fatigue bar before testing and after approximately 100 cycles at 1600 nm, 1800 nm, 2100 nm, and 2500 nm respectively in order to study the microstructural changes over the course of cycling at various amplitudes. There was no clear evidence of grain coarsening as previously reported in literature for macroscopic fatigue testing of similar material. However, it appears as if some of the grain orientations have changed. This can be seen in Figure 4.2.2i. When looking at the orange ovular grain and its neighbors, this grain appears to maintain its initial orientation up to fatiguing past the 1800 nm displacement cycles, but then changes orientation slightly after

the 2100 nm displacement cycles and has severely changed orientation as seen by the bright pink after the 2500 nm displacement stage. Increased deformation on the fatigue bar surface as well as oxidation and a focus of zooming in on the root sections of the bar account for the differences in image quality.
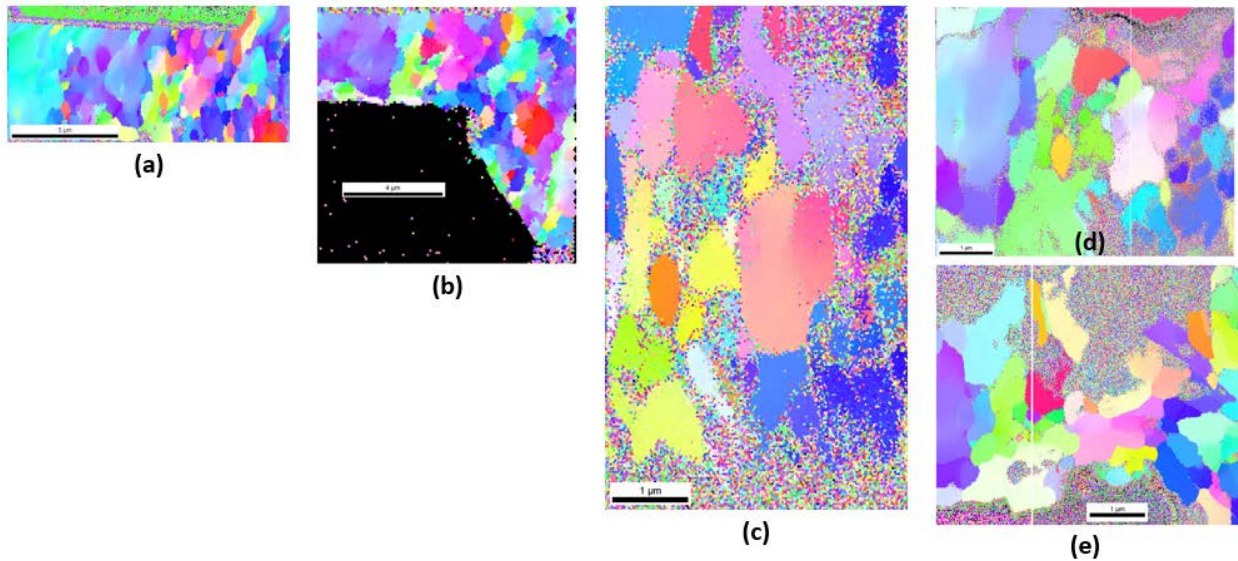

Figure 4.2.2i EBSD scan IPF maps of the ECAP Cu fatigue bar (a) before testing, (b) after 100 1600 nm cycles, (c) after 100 1800 nm displacement cycles, (d) after 100 2100 nm displacement cycles, and (e) after 100 2500 nm displacement cycles. A region of interest at the bottom of the bar at its root was chosen and the microstructural evolution of this portion of the bar was followed closely. Grain coursening is not evident. However, grain orientation changes due appear to occur after 100 1800 nm displacement cycles.

Post deformation SEM micrographs reveal areas near the base of the bar that have been highly deformed after the 2100 nm nominal displacement cycling. A 1 μm crack can be seen running along the top of the bar from the edge as well as down along the width of the bar. Multiple 45° striations in this region can also be seen (Figure 4.2.2j)
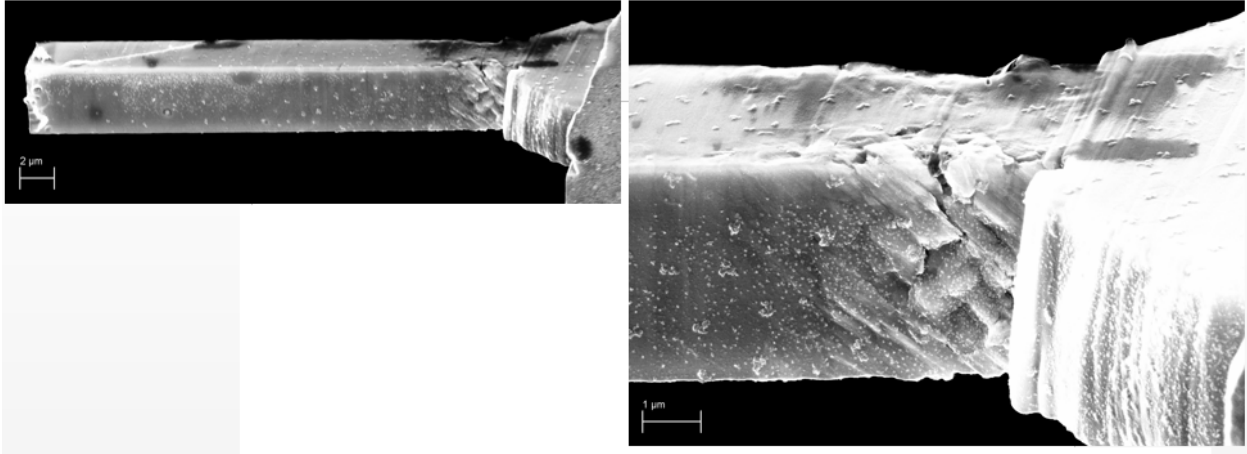
Figure 4.2.2j SEM micrograph of the ECAP Cu fatigue bar after completing the 2100 nm nominal displacement cycling stage.

4.2.3 Copper Comparison

A comparison of the single crystal and ECAP copper micro fatigue bars shows that the energy dispersed per cycle is higher for the ECAP bar at every amplitude. This is approximately 300 J/m^2 higher at 1250 nm displacement amplitudes but quickly increases to 1000-1300 J/m^2 for amplitudes larger than 1500 nm, $\varepsilon_{pl} > 4 \times 10^{-3}$. This can be seen in Figure 4.2.3a. In addition, the ECAP Cu bar undergoes an increased hardening rate compared to the single crystal Cu bar for strains between 1×10^{-3} and 3×10^{-3}. It continues to harden while the single crystal bar has already reached its plateau regime, but at a strain of 5×10^{-3}, the ECAP cyclic stress-strain curve has reached its peak stress value and rapidly undergoes cyclic softening at higher strains (Figure 4.2.3b). Although the orientation of the single crystal bar is unknown, it is of note that the ECAP Cu bar has a higher initial yield point and its maximum stress values are always higher than the single crystal bar when the two bars undergo the same amount of strain.
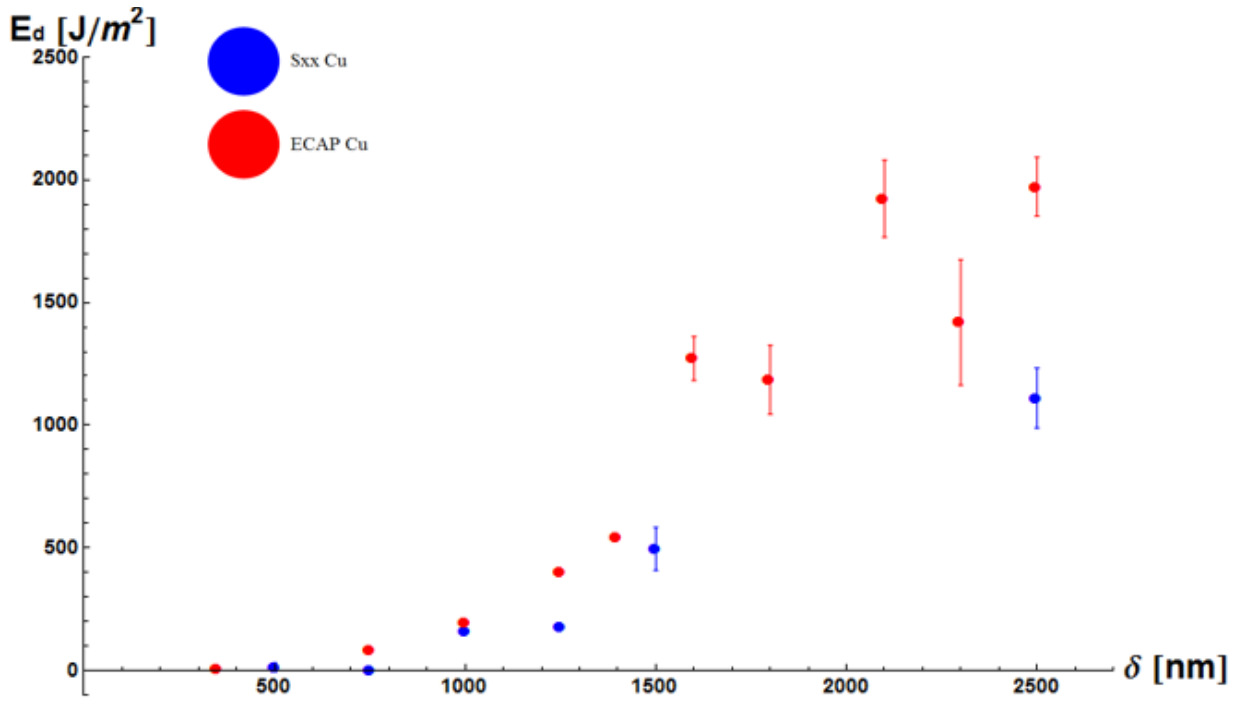
Figure 4.2.3a A comparison of the energy dissipation per cycle between the ECAP and single crystal fatigue bars. More energy is dissipated per cycle in the ECAP copper.
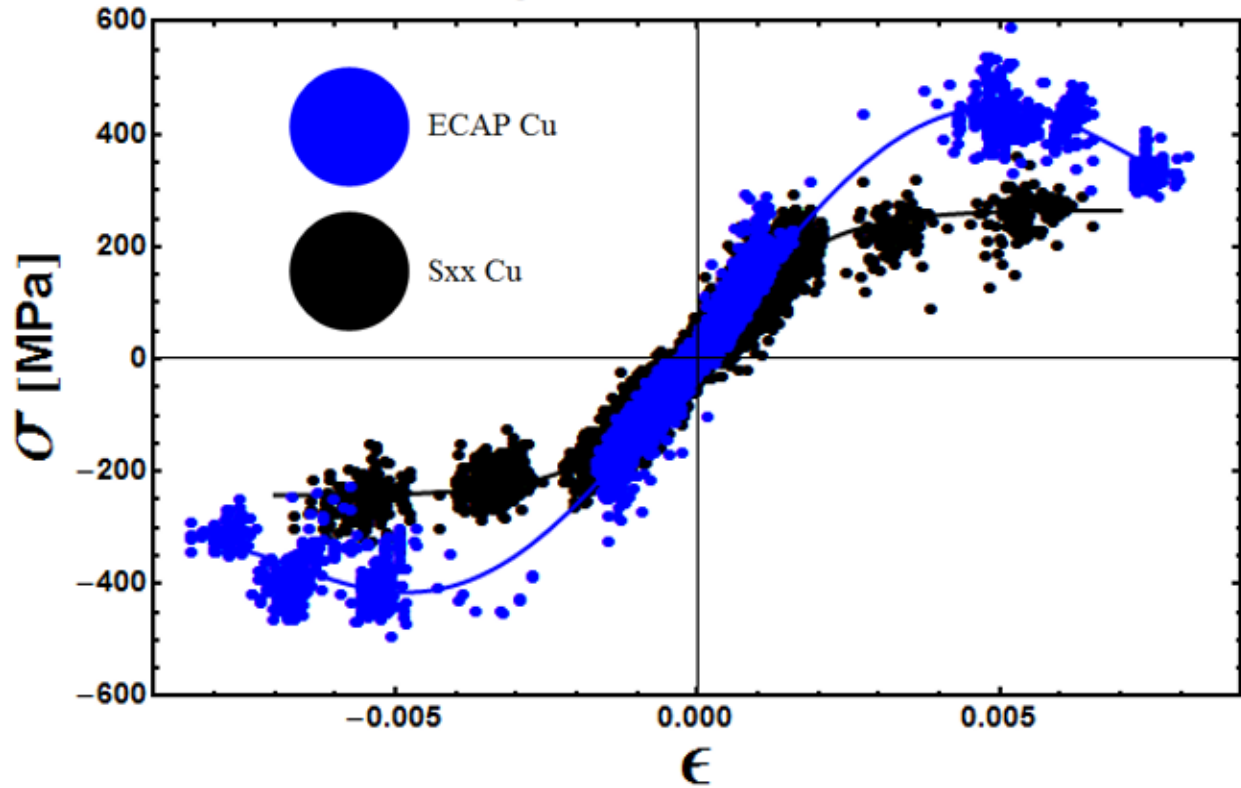
Figure 4.2.3b The cyclic stress-strain curve for the ECAP copper bar reaches a higher maximum stress, has a higher cyclic yield strength, and undergoes a longer period of hardening than the single crystal copper bar. However, it does undergo cyclic softening for strains larger than 5×10^{-3} and does not have a stable plateau regime like the single crystal bar.

4.2.4 Single Crystal PM 2000
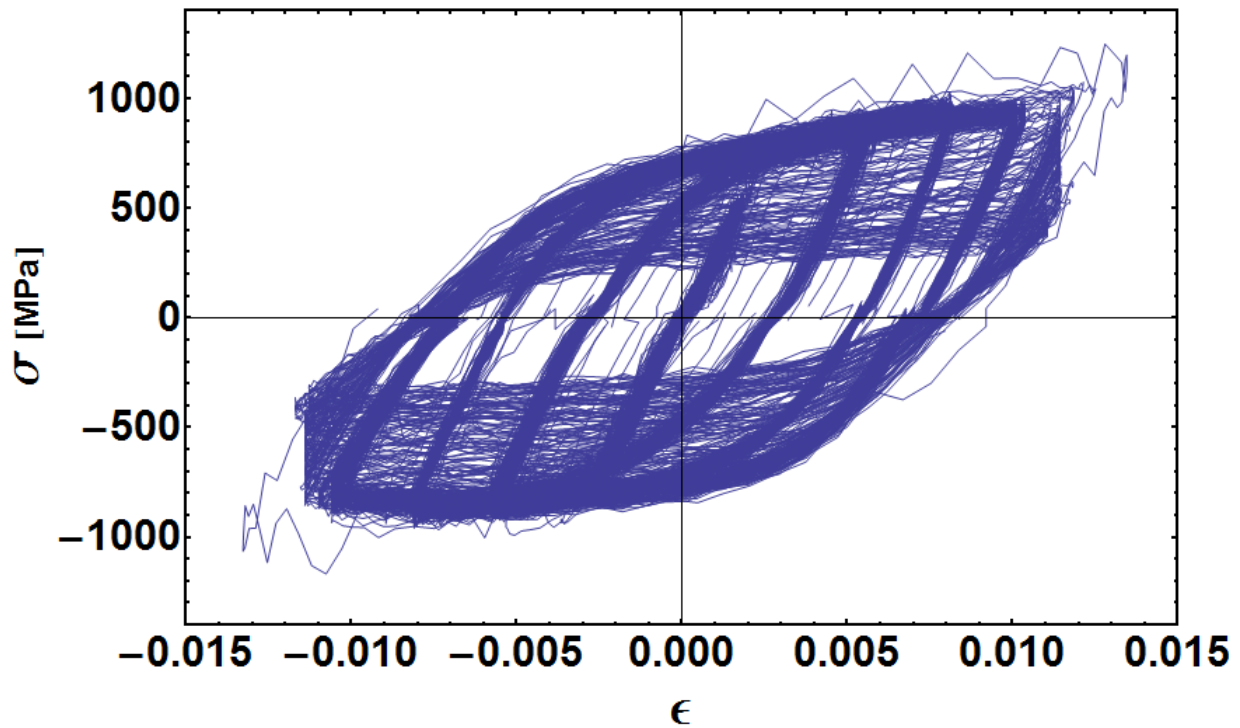
Figure 4.2.4a Stress-strain curves of all cycles for the single crystal PM 2000 micro fatigue bar reported in Table 3.2.4c

As noted in Table 3.2.4c, there were 100 cycles performed at a nominal displacement of 300 nm. All of these cycles were deemed to be purely in the elastic deformation regime. After measurements of the bending length during these cycles were made as well as previously described corrections, the stress-strain curves for these cycles can be seen in Figure 4.2.4b. These curves were fit to a linear regression where the slope can be taken as the elastic modulus. This value is 286 GPa, which is 1.66 times larger than the upper estimate of the reported literature value of 173 GPa.
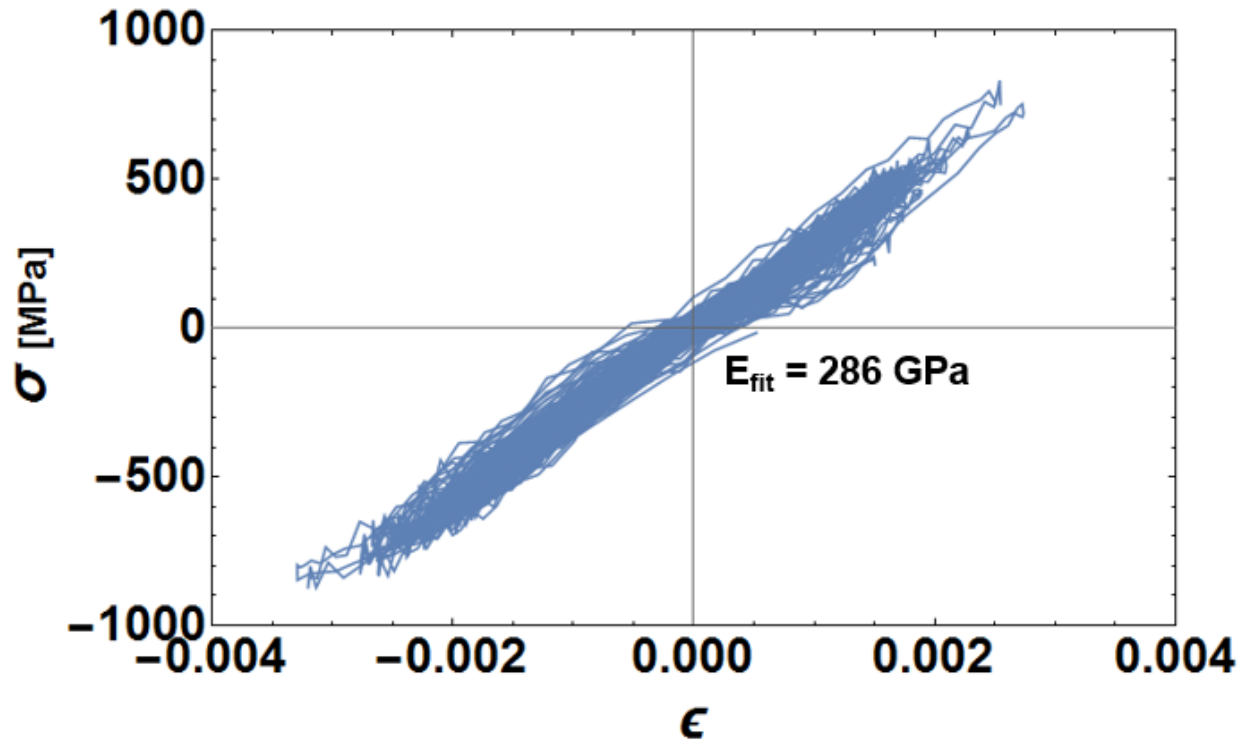
Figure 4.2.4b Purely elastic cyclic loading of the single crystal PM 2000 micro fatigue bar.

The 102 cycles performed at 1200 nm nominal displacement were deemed to be "yielding cycles" at which point in time a clear yielding point was established. However, after post-processing, the stress-strain curves for nominal displacements between 800 nm and 1000 nm also showed evidence of plastic deformation and were evaluated for yield points as well. Yield points were measured every half cycle and their magnitudes were plotted as a function of cycle number for each amplitude (Figure 4.2.4d) to determine cyclic stability as well as versus amplitude (Figure 4.2.4e). The same was done for elastic moduli and maximum stress at every half cycle (Figure 4.2.4c). In addition the maximum strain values of every cycle were taken from stable cycles at each amplitude and combined with the purely elastic cycles to produce a cyclic stress-strain curve (Figure 4.2.4f). Finally, the energy dissipated per cycle was plotted as a function of cycle number and amplitude (Figure 4.2.4 g).

Let it be noted that for the single crystal PM 2000 micro fatigue bar, its mechanical properties were completely compromised during the last 100 cycles at 2500 nm nominal displacement, equivalent to a maximum strain of 0.012, whereas all other displacement amplitudes

remained cyclically stable. Therefore, all properties associated with this last loading with the most severe amount of plastic deformation have been separated in order to highlight their affects. The data for these cycles can be seen in Figure 4.2.4h.
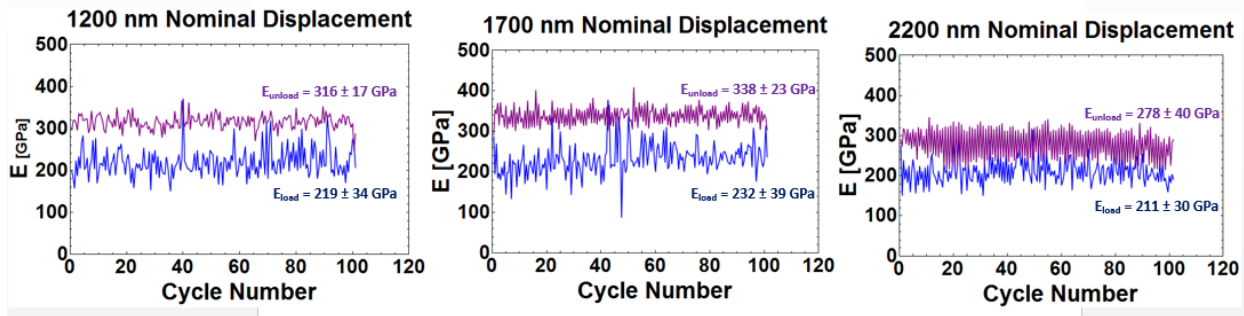

Figure 4.2.4c The elastic modulus values for the single crystal PM 2000 fatigue bar remain cyclically stable for displacement amplitudes between 1200 nm and 2200 nm, equivalent to strains between 8×10^{-3} and 0.01. However, similar to the ECAP Cu bar, the unloading moduli are always larger than the loading moduli. This can be attributed to the fact that at larger deflections more plastic strain occurs that is neglected in the geometrical analytical calculation for strain at the root of the fatigue bar. In this case, for the single crystal PM 2000 bar, all values are larger than the accepted literature value. However, if only the linear elastic loading values are taken and averaged, they come out to 221 GPa, which is close to the generic values accepted for stainless steels.
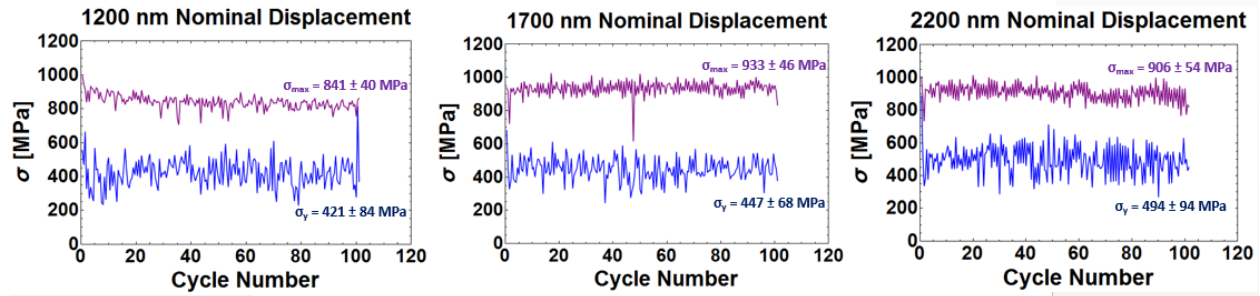
Figure 4.2.4d The yield strength and maximum strength of the single crystal PM 2000 fatigue bar is cyclically stable for displacement amplitudes between 1200 nm and 2200 nm, equivalent to strains between 8 x 10^{-3} and 0.01. The yield strength values obtained by cyclic fatigue studies are within one to two standard deviations of the reported values from PLANSEE of the bulk mechanical tensile strength of 525 MPa. There is a gradual increase in yield strength of approximately 70 MPa as strain amplitude is increased. Maximum stress values increase by approximately 65-90 MPa over this increase in strain range as well.
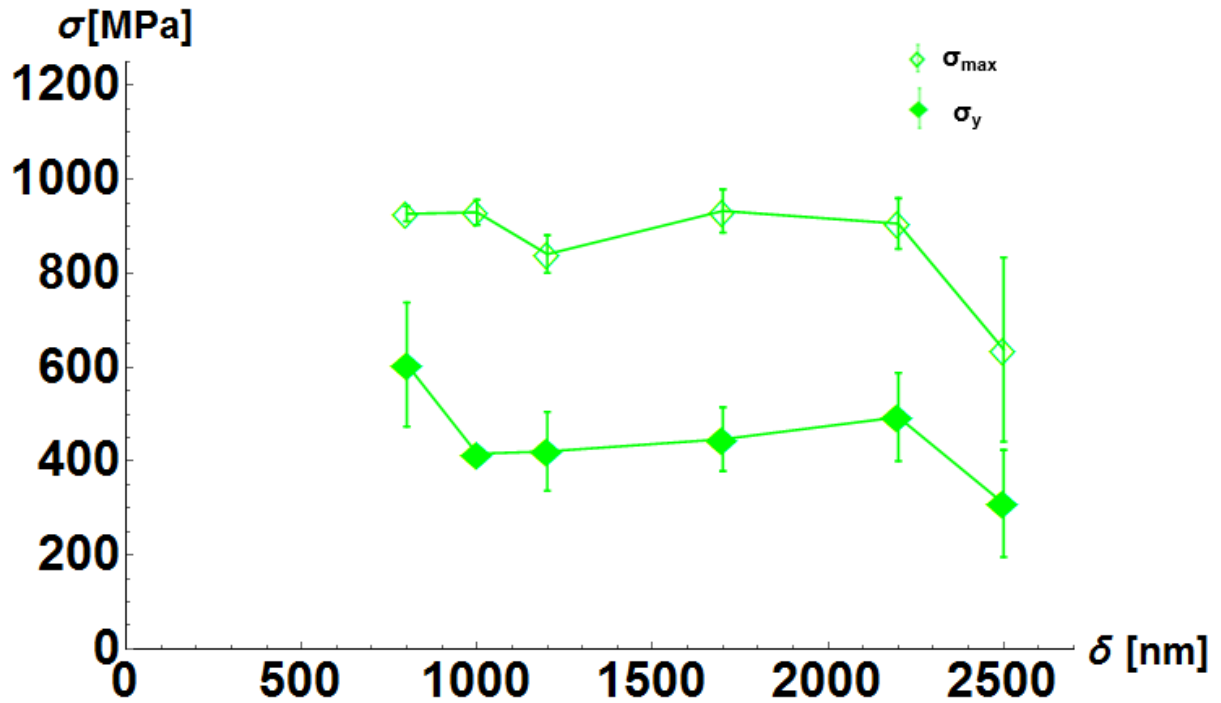
Figure 4.2.4e Stress evolution of the single crystal PM 2000 micro fatigue bar as a function of increasing displacement amplitude. There appears to be a rapid loss of yield strength if the value at 800 nm nominal displacement of 606 MPa is taken as the true yield point. Then, there is a drop of 150 MPa to a stable plateau regime between strains of 5×10^{-3} and 0.01. As previously mentioned, at strains greater than 0.01, dramatic softening occurs. Maximum stress values appear to be relatively constant around 900 MPa for cyclic loading at strains below 0.01.
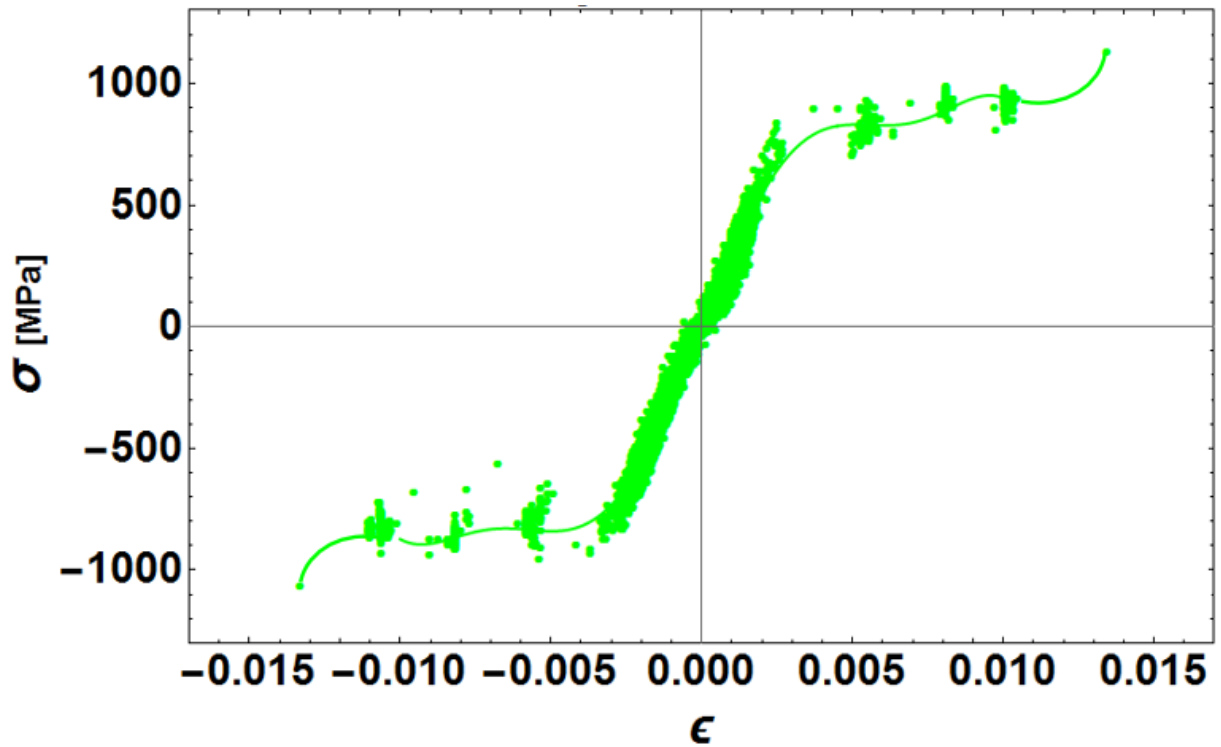
Figure 4.2.4f The cyclic stress-strain curve for the single crystal PM 2000 bar. Linear elastic loading occurs at strain amplitudes less than 3 x 10^{-3}, a stable plateau region exists for strain amplitudes between 3 x 10^{-3} and .01, and for strain amplitudes larger than .01 stress again increases. The cyclic yield point occurs much higher, 700-800 MPa, than the bulk mechanical monotonic yield value of 525 MPa.
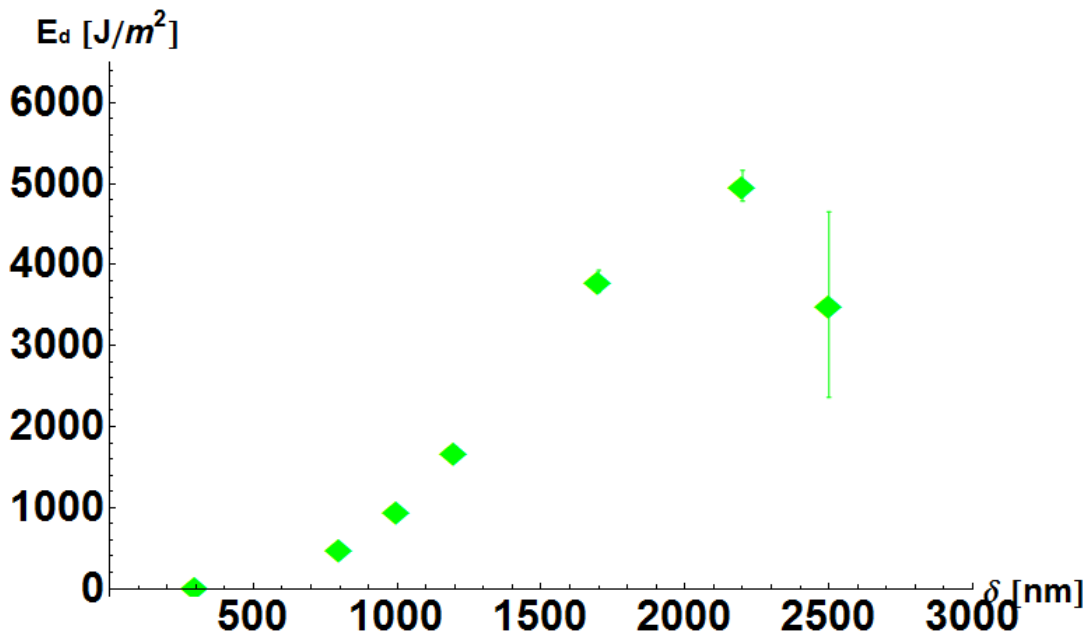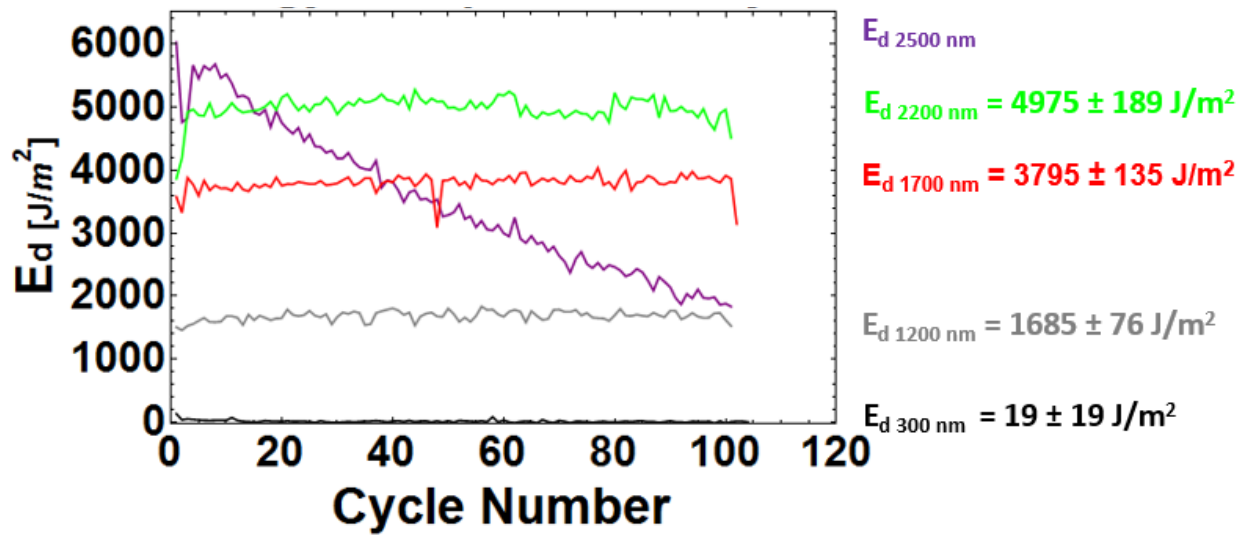
Figure 4.2.4g Energy dissipated per cycle for the single crystal PM 2000 micro fatigue bar. We see that at 300 nm nominal displacement no energy is dispersed. After this point, plastic deformation plays a role and becomes increasingly evident as the amount of energy dissipated per cycle rapidly increases between nominal displacements of 800 nm and 2200 nm. However, after this, as strain amplitudes increase more beyond .01, the energy dissipated per cycle has already reached its peak value, cyclic stability no longer exists, cyclic softening begins, and the energy dissipated per cycle decreases.
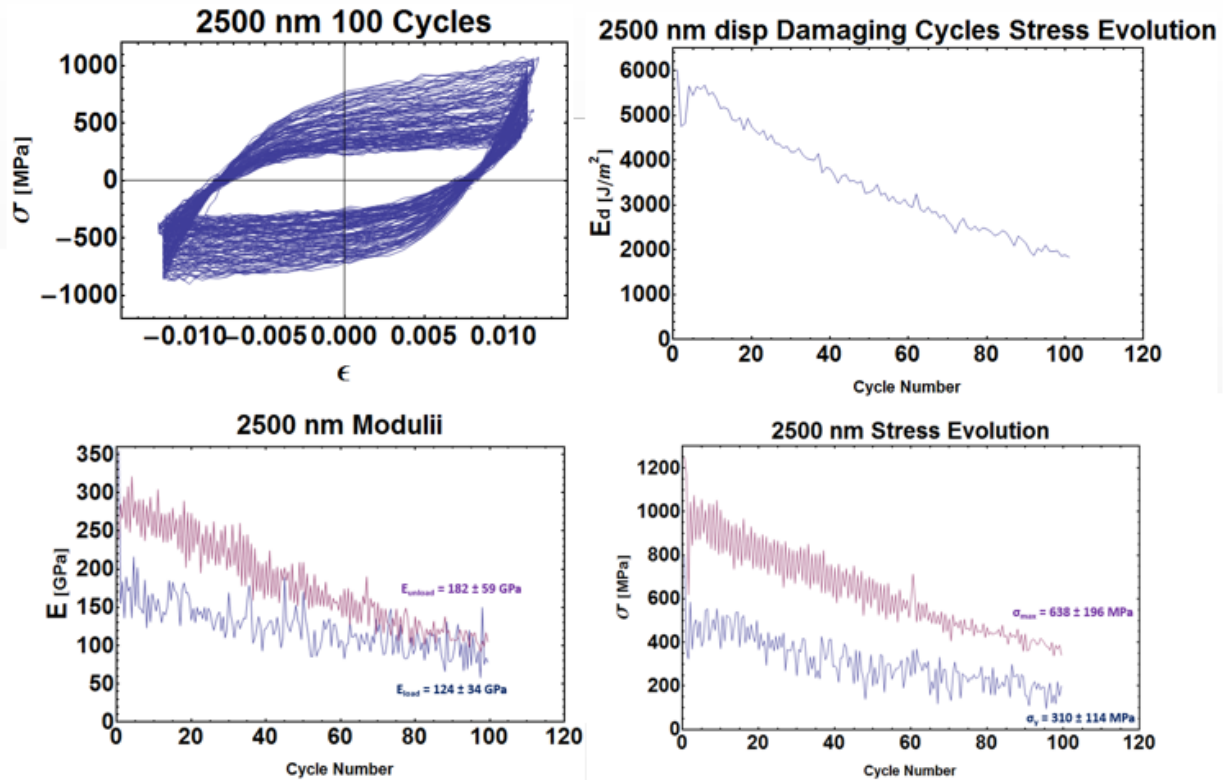
Figure 4.2.4h The mechanical properties of the single crystal PM 2000 fatigue bar have been severely compromised at a nominal displacement of 2500 nm, equivalent to a strain amplitude of 0.012. We can see after 100 cycles that the yield strength has dropped to approximately 22% of its original value, from 450 MPa down to 100 MPa. The maximum stress has also dropped drastically from 1000 MPa to 340 MPa. The energy dissipated per cycle follows a similar trend, dropping from 6000 J/m^2 to 2000 J/m^2. This severe cyclic softening can be evidenced at the upper left in the stress-strain hysteresis loops.

SEM micrographs reveal that cracks that initiated after the 2200 nm nominal displacement cycling stages have propagated completely across the bar after the final cycling at 2500 nm nominal displacement (Figure 4.2.4i). This evolution is directly correlated to the mechanical behavior shown in Figure 4.2.4h.
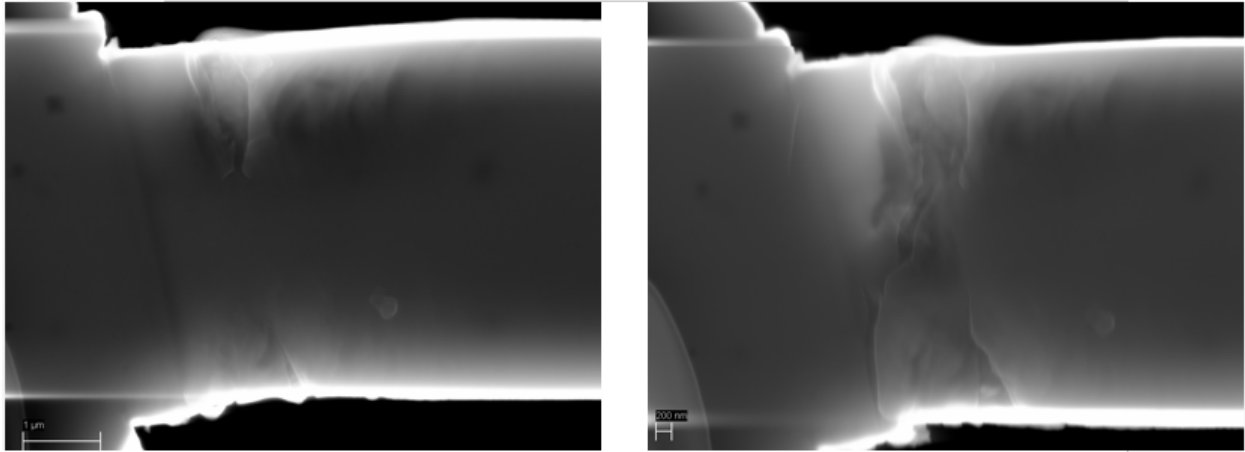
Figure 4.2.4i SEM micrographs depicting crack growth across the top of the single crystal PM 2000 fatigue bar very close to the root. On the left, cracks seem to be emerging from the top and bottom edges after 100 cycles at 2200 nm nominal displacement. On the right, after 100 cycles at 2500 nm nominal displacement, these cracks have propagated completely through the length of the top of the bar.

4.2.5 HPT PM 2000

HPT Processing

The HPT PM 2000 material was processed by taking a rounded 8 mm diameter disk of 2 mm thickness and subjecting it to 26 turns at a nominal pressure of 7.6 GPa. A constant torque value was obtained, so this material is considered to be completely saturated where its microstructure has reached a steady state. The torque versus time curve can be seen in Figure 4.2.5a. An optical micrograph of the resulting disk can be seen in Figure 4.2.5b. This saturation was further assessed by performing Vickers microhardness across the radial profile of the disk. This hardness profile was relatively constant around 600-650 HV as seen in Figure 4.2.5c.
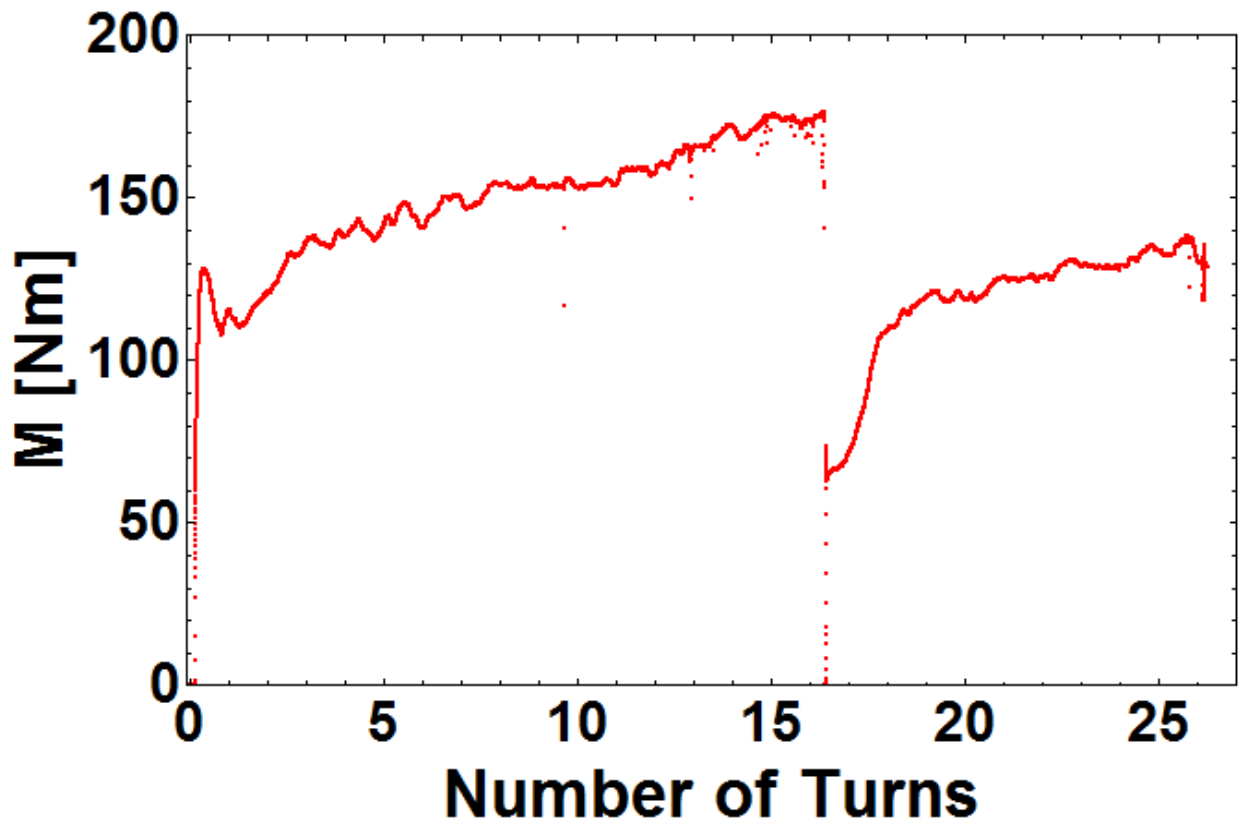
Figure 4.2.5a Diagram displaying torque versus number of turns for the HPT PM 2000 fatigue sample. The jump at 16 turns occurs due to misalignment between the anvils. The test had to be reset and started again.

Figure 4.2.5b Optical micrograph of the HPT PM 2000 disk

Microhardness
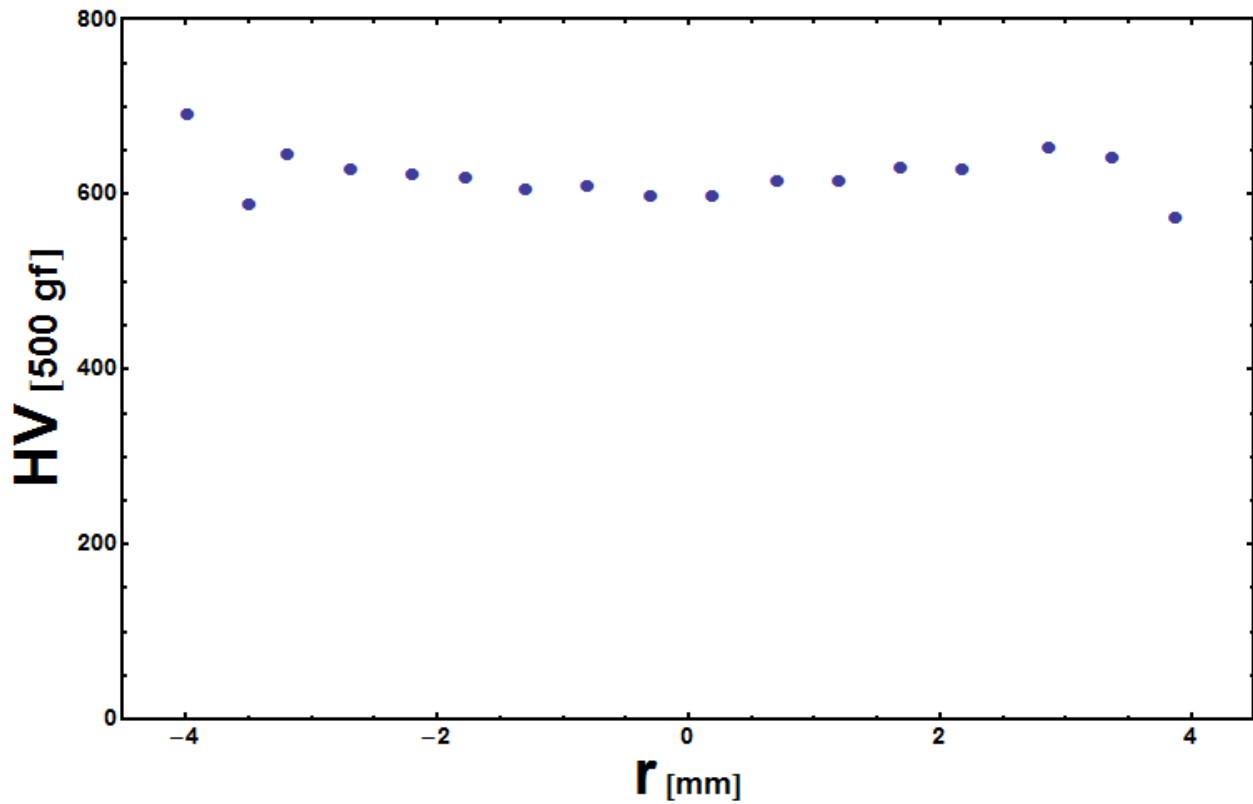
Figure 4.2.5c Vickers radial hardness profile of the above HPT PM 2000 disk indicating that the microstructure is completely saturated because it is stable between 600-650 HV across the entire length of the disk.

Microfatigue
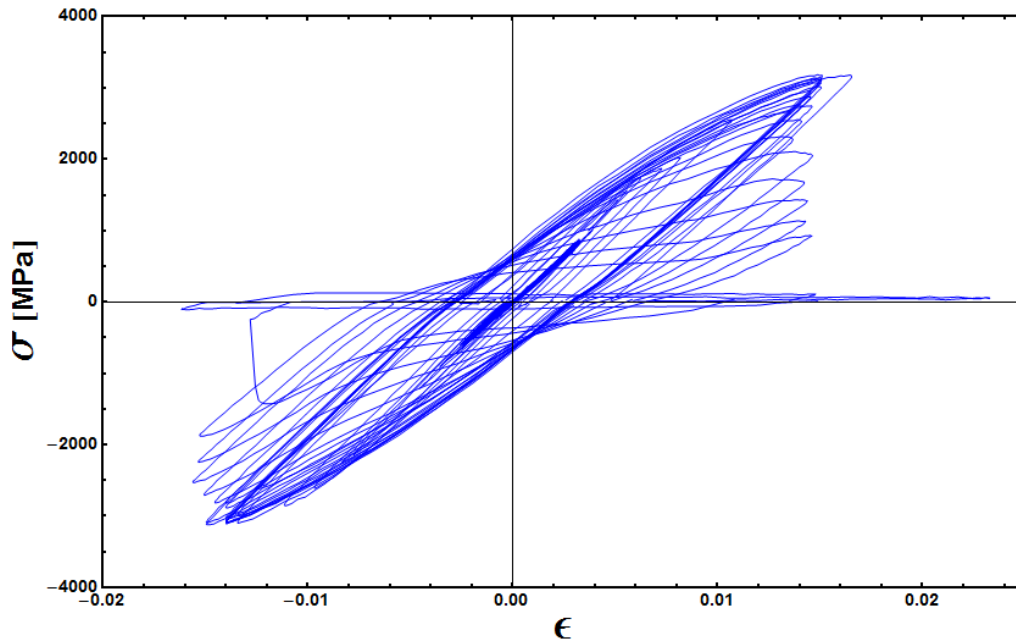
Figure 4.2.5d Stress-strain curves of all cycles for the HPT PM 2000 micro fatigue bar reported in Table 3.2.4d

As noted in Table 3.2.4d, there were 103 cycles performed at a nominal displacement of 300 nm. All of these cycles were deemed to be purely in the elastic deformation regime. After measurements of the bending length during these cycles were made as well as previously described corrections, the stress-strain curves for these cycles can be seen in Figure 4.2.5e. These curves were fit to a linear regression where the slope can be taken as the elastic modulus. This value is 252 GPa which is in good agreement with the value of 286 GPa measured for the single crystal PM 2000 fatigue bar. However, it is much larger than the literature value of 173 GPa. It can be seen that these cycles are purely elastic based on the fact that almost no energy is dissipated per cycle as can be seen in Figure 4.2.5f.
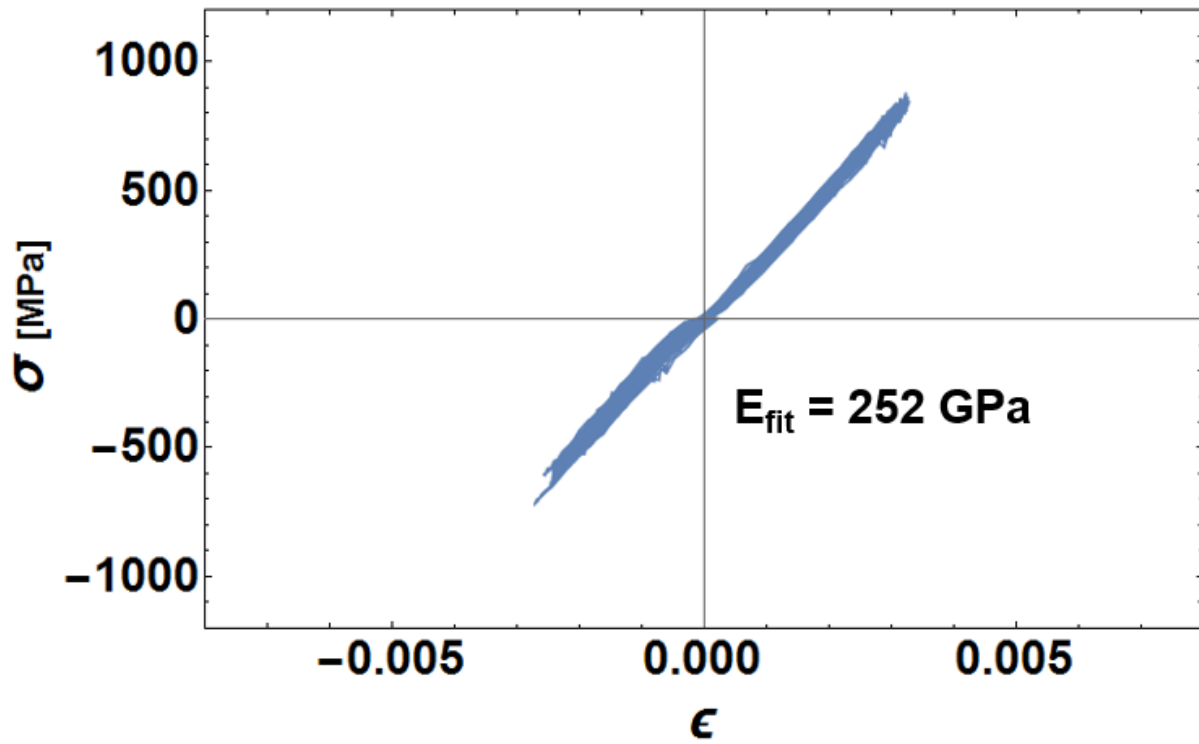
Figure 4.2.5e Purely elastic cyclic loading of the HPT PM 2000 micro fatigue bar.
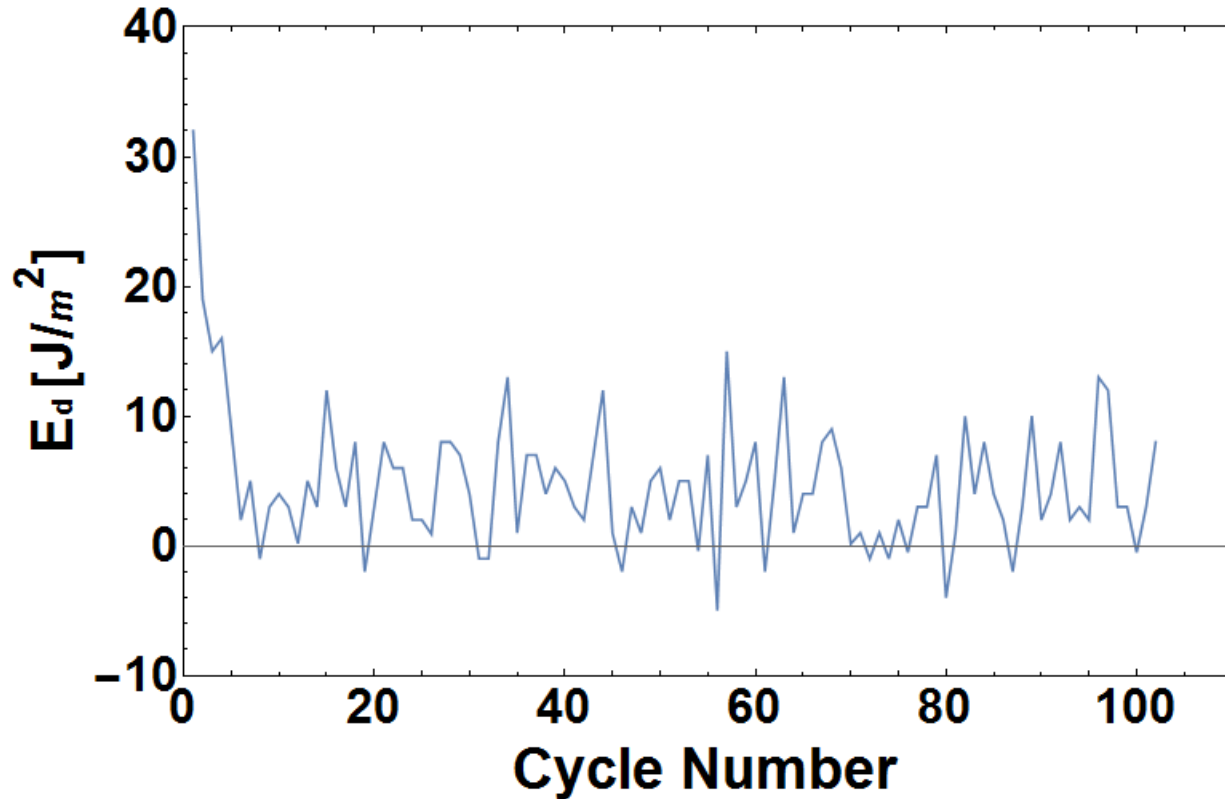
Figure 4.2.5f The energy dissipated per cycle during the 100 elastic loading cycles at 300 nm nominal displacement for the HPT PM 2000 fatigue bar. On average 5 ± 5 J/m² of energy are released per cycle, evidence that these cycles are in the elastic regime.

The HPT PM 2000 fatigue bar was highly strengthened compared to its single crystal counterpart, so a yield point was not clearly noticed during testing. During post analysis, yield points were determined for all cycles with nominal displacements larger than 1200 nm. These yield points and the maximum stress points were plotted versus nominal displacement amplitude as can be seen in Figure 4.2.5g. During the final 20 cycles at 3600 nm nominal displacement yield points were measured every half cycle as well as maximum stress points, elastic moduli, and the energy dissipated per cycle and their magnitudes were plotted as a function of cycle number for each amplitude (Figure 4.2.5h). In addition the maximum strain values of every cycle were taken from stable cycles at each amplitude and combined with the purely elastic cycles to produce a cyclic stress-strain curve (Figure 4.2.5i). Finally, the energy dissipated per cycle was plotted as a function of amplitude (Figure 4.2.5j).
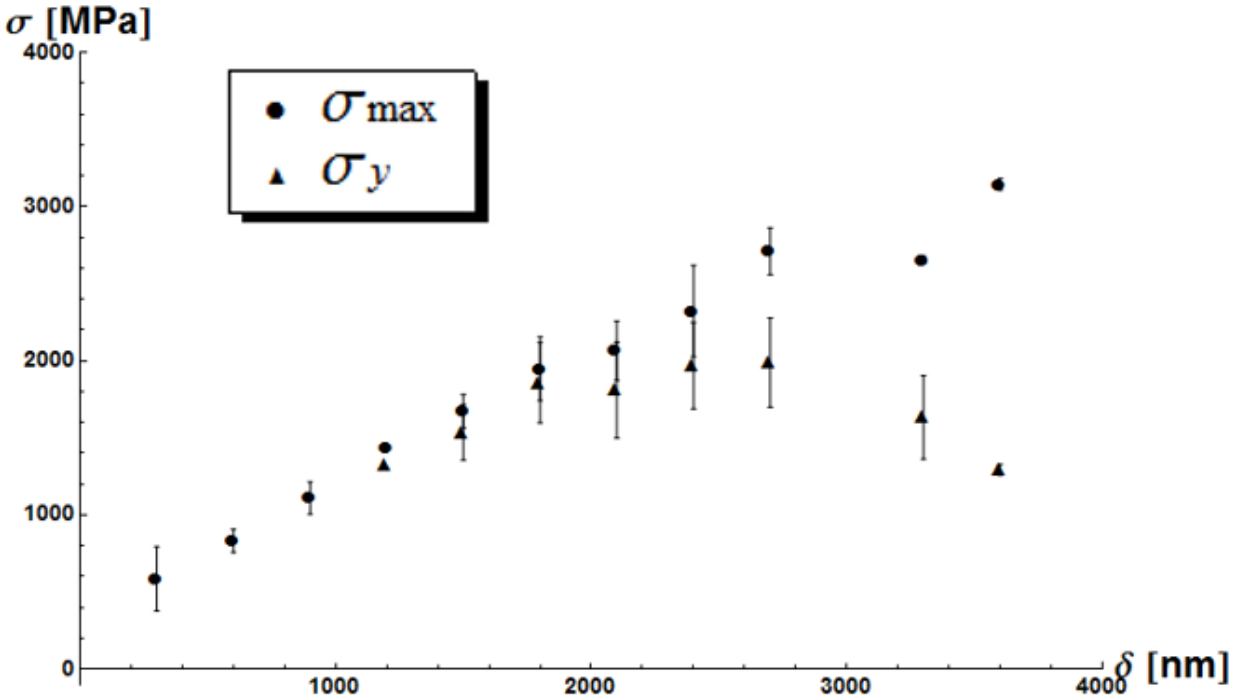
Figure 4.2.5g The stress evolution of the PM 2000 fatigue bar as a function of nominal displacement amplitudes. Monotonic hardening is evident in the continual increase of the maximum stress values throughout the entire range of amplitudes. However, cyclic loading causes the initial yield point to increase up to a maximum value at 1800 nm nominal displacement. Here it has reached a stable plateau out to nominal displacements of 2700 nm and then softening occurs at higher amplitudes.
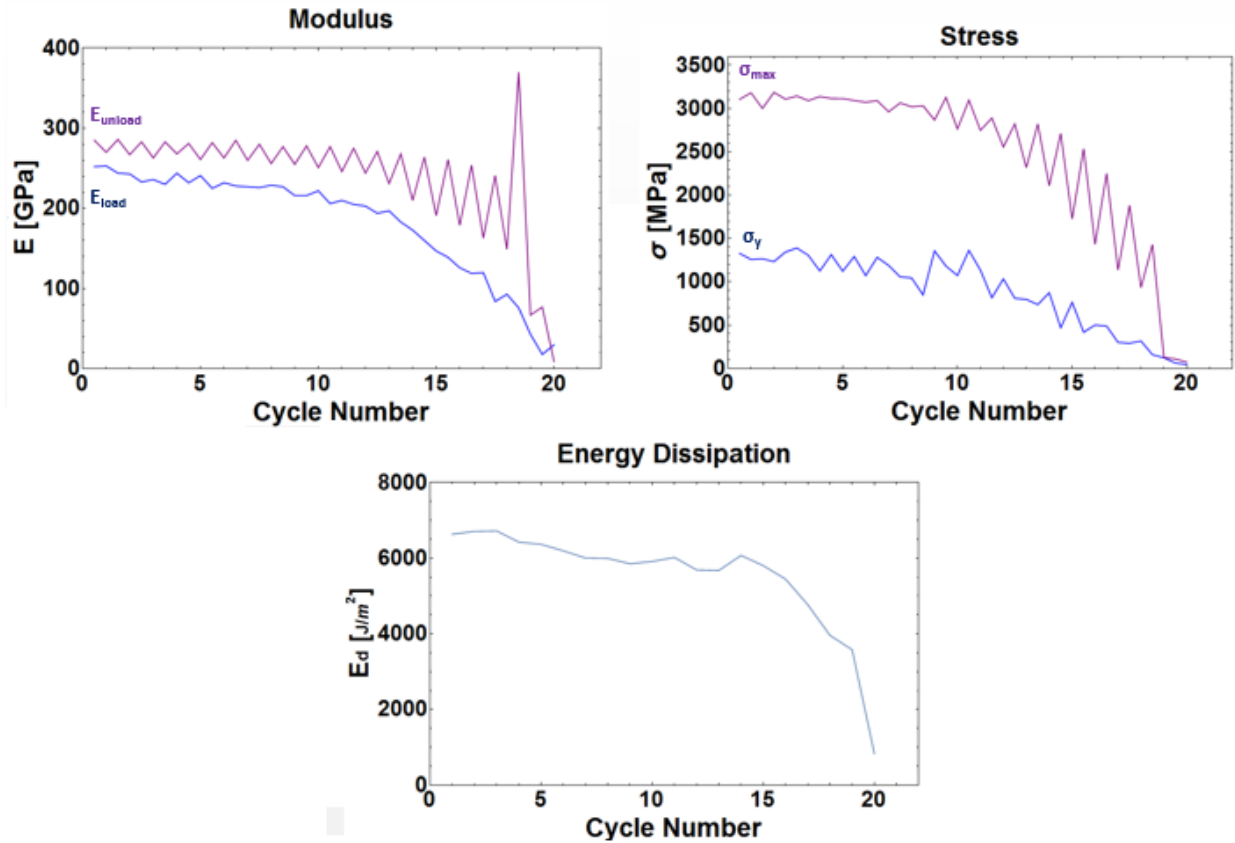
**Figure 4.2.5h** The cyclic evolution of the mechanical properties of the HPT PM 2000 fatigue bar at 3600 nm nominal displacement equivalent to a strain amplitude of ~0.014. Rapid cyclic softening after approximately 10 cycles occurs in route to failure on the 20th cycle. The elastic modulus also diminishes after the first 12 cycles, and the energy dissipated per cycle after the 14th cycle.
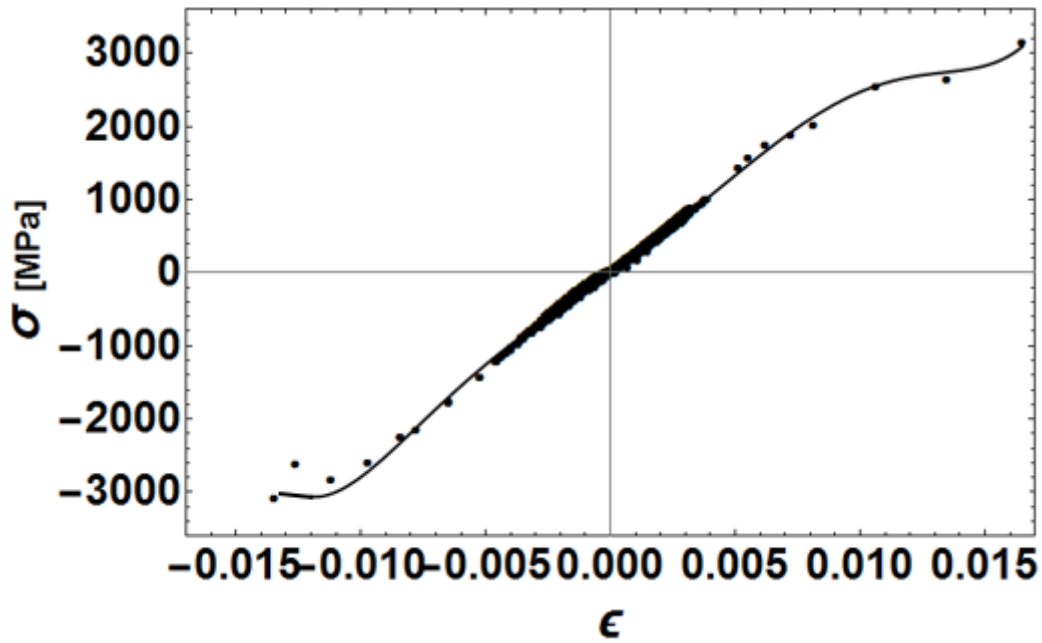
Figure 4.2.5i The cyclic stress-strain curve for the HPT PM 2000 fatigue bar shows linear elastic for strains less than 8 x 10^{-3} with a cyclic yield strength close to 3 GPa. There is little to no cyclic ductility after this point. There is a small plateau after yielding, 0.01 to 0.013, but fracture occurs at strains between 0.013 and 0.016.
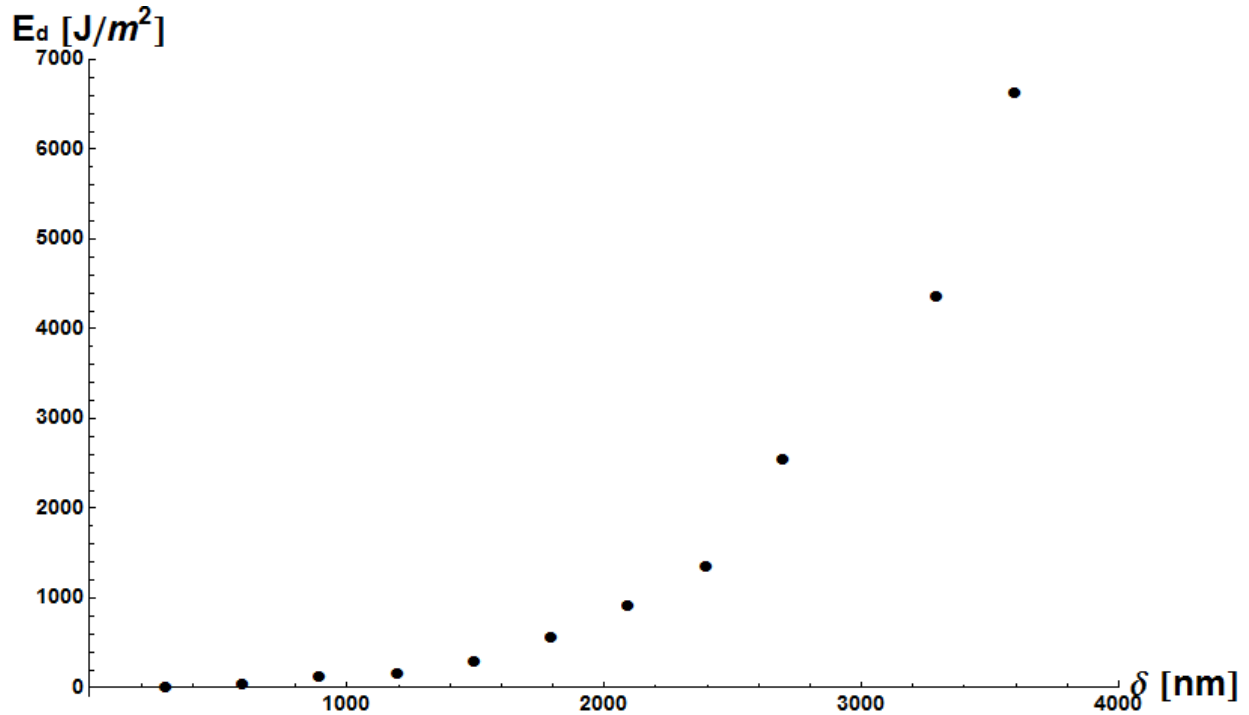
Figure 4.2.5j The energy dissipated per cycle for the HPT PM 2000 fatigue bar follows an exponential increase throughout the entire range of displacements.

The HPT PM 2000 fatigue bar was the only one to be driven to complete failure. An SEM micrograph showing the fractured fatigue bar can be seen in Figure 4.2.5k.
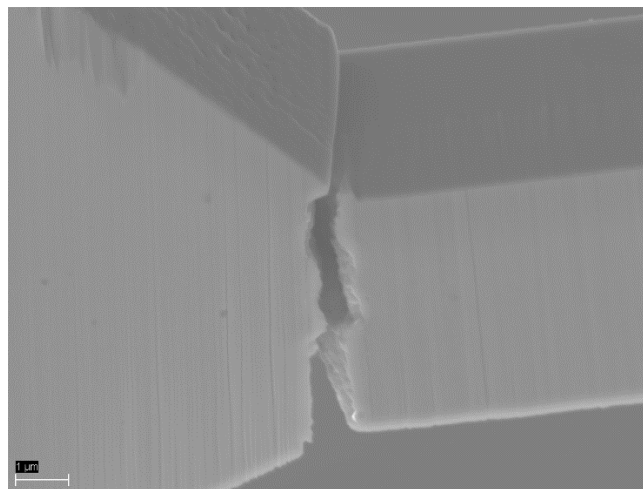
Figure 4.2.5k SEM micrograph of the fractured HPT PM 2000 fatigue bar. The fracture occurred exactly along the base of the bar as the crack propagated through the thickness of the bar.

4.2.6 PM 2000 Comparison

Because the HPT processing generates an UFG structure, this has an inherent strengthening effect. This is evidenced in the much higher yield stress and maximum stress values endured by the HPT PM 2000 fatigue bar compared to the single crystal fatigue bar that can be seen in Figure 4.2.6a below. It is also of note that there is more internal energy released per cycle in the single crystal fatigue bar than the HPT fatigue bar as seen in Figure 4.2.6b. The HPT PM 2000 bar has a much greater amount of work hardening in its cyclic stress-strain curve compared to the single crystal bar as seen in Figure 4.2.6c.
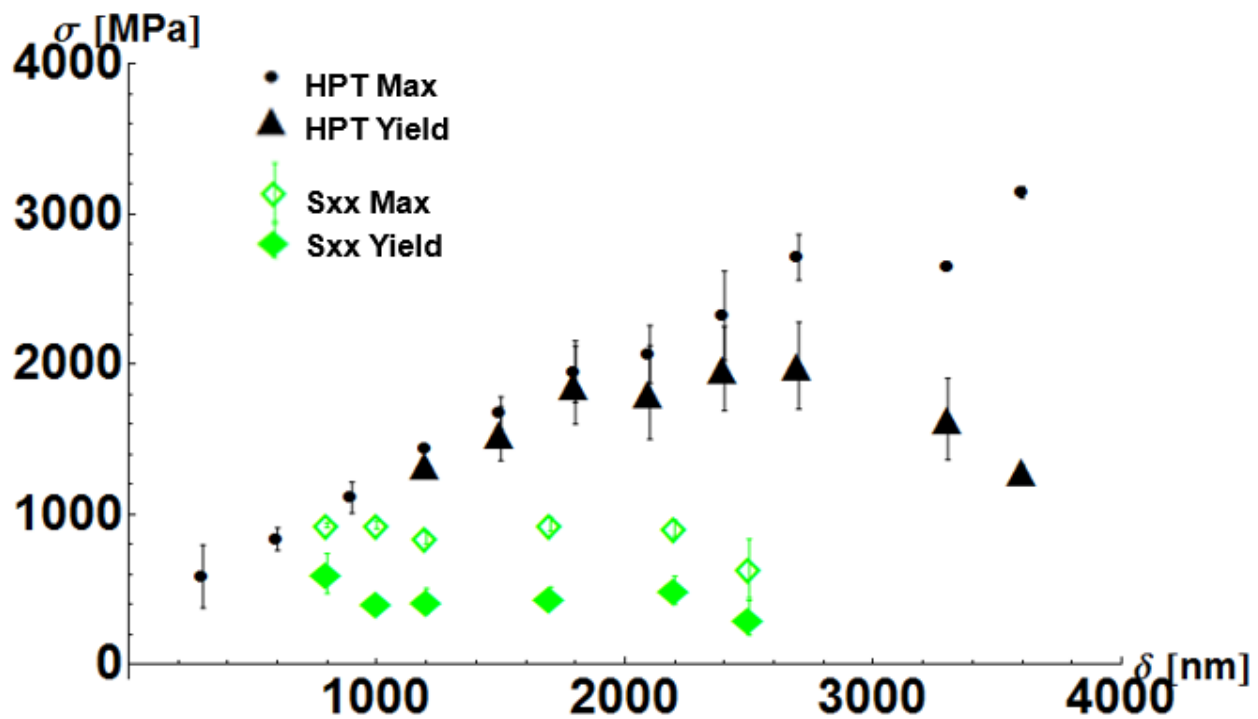
Figure 4.2.6a Stress comparisons of the single crystal and HPT PM 2000 fatigue bars show that the HPT processing has strengthened the material by a factor of about 2-3 when evaluating the yield points at nominal displacements between 1600 nm and 2600 nm. The stresses in the single crystal bar quickly reach a stable plateau, whereas the yield stresses in the HPT bar undergo an initial increase, then a stable plateau region, and finally softening. The plateau for maximum stress values occurs at a higher amplitude than that for yield, 2700

nm nominal displacement versus 1800 nm nominal displacement for yielding. However, after 3200 nm nominal displacement, the maximum stress again increases.
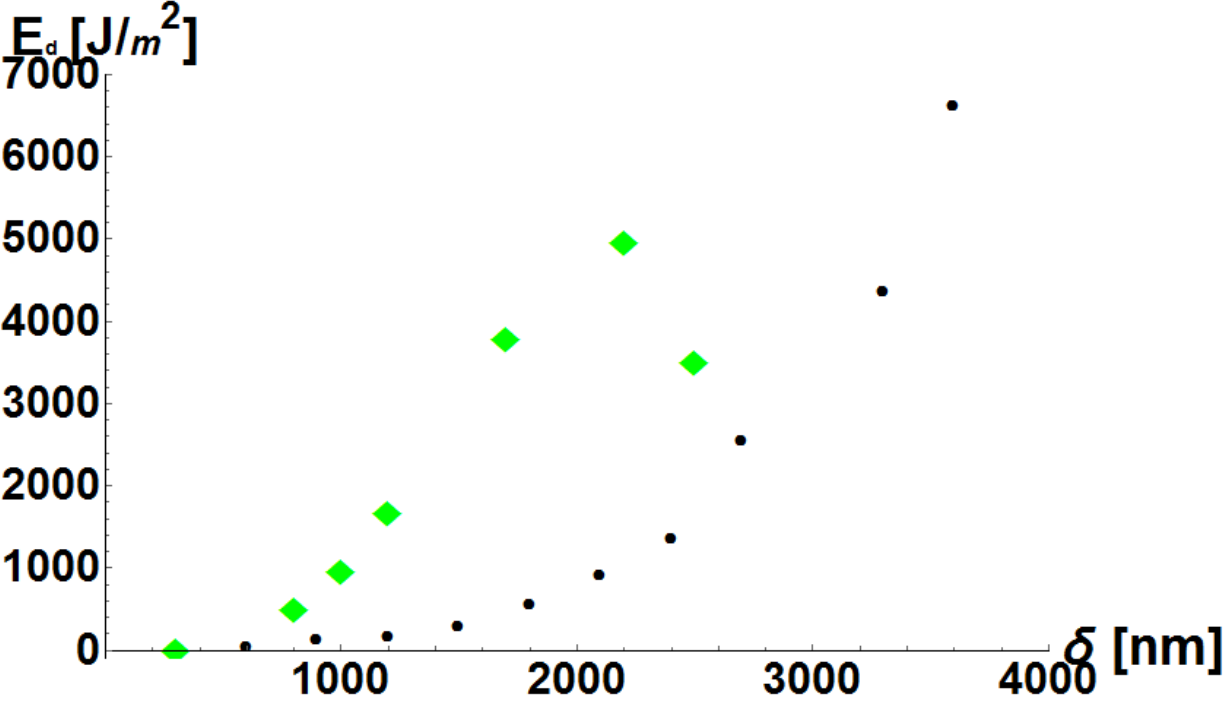
Figure 4.2.6b The energy dissipation per cycle of the single crystal PM 2000 bar (green) and HPT PM2000 bar (black).
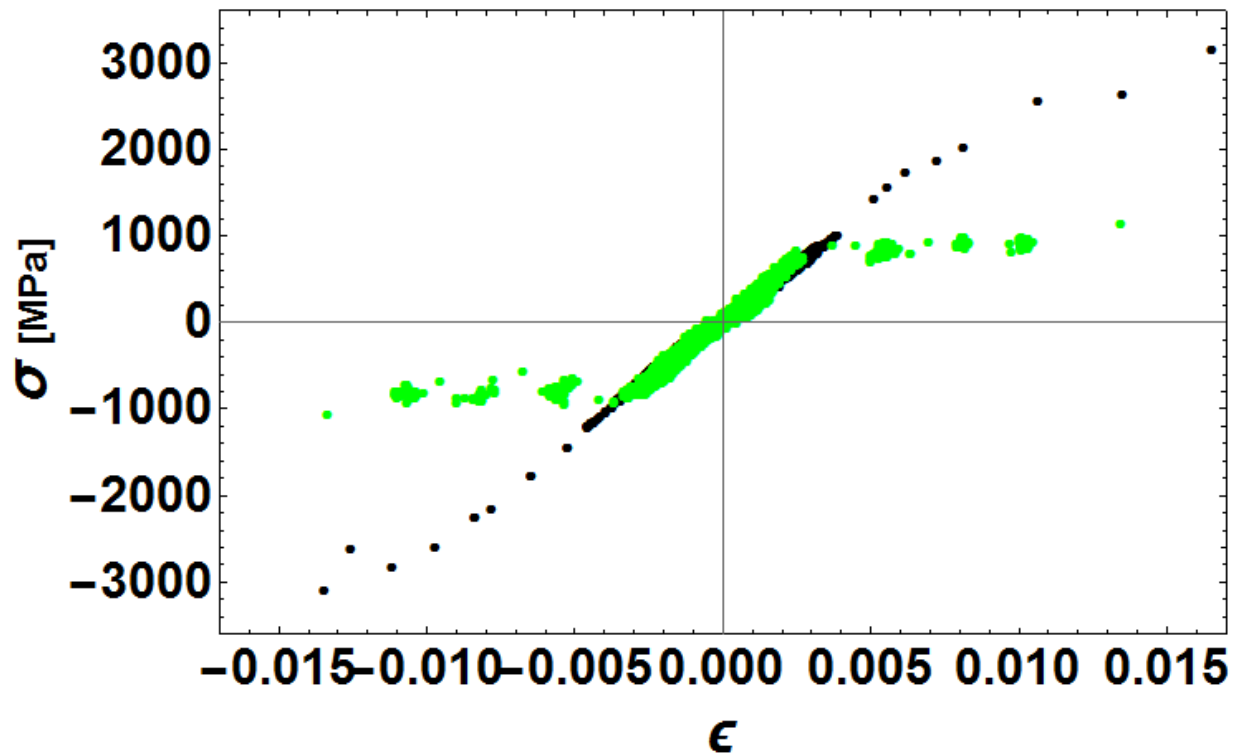
Figure 4.2.6c Cyclic stress-strain curves of the single crystal PM 2000, green, and HPT PM 2000, black. The single crystal bar immediately reaches a stable stress plateau after yielding, whereas the HPT bar undergoes a small work-hardening stage, strains 7 x 10^{-3} to 0.01, and then failure occurs at strains around 0.015. The HPT bar is 1 to 2 GPa stronger than the single crystal bar.

5. Summary and Outlook on Future Work

As demonstrated, material fabrication via SPD techniques, specifically ECAP and HPT techniques, on highly complex nanostructured alloys and subsequent in situ micro fatigue testing of these alloys provides a feasible method for studying the cyclic evolution of their mechanical properties. In depth investigations of ECAP Cu and HPT PM 2000 and the cyclic evolution of their elastic modulus, yield strength, energy dissipated per cycle, and cyclic stress-strain curves as well as a comparison to their single crystal counterparts and bulk mechanical testing was achieved. The nanostructured alloys undergo periods of hardening and softening as their plastic strain amplitudes are increased whereas the single crystal materials reach a steady-state stress plateau and remain stable there. The first two regimes evidenced by Mughrabi in macroscopic fatigue [108, 111] were also seen in the micro fatigue tests displayed here. However, grain coarsening effects remain inconclusive although there appears to be some evidence of changes in the grain orientations of grains near the bases of the fatigue bars.

Further analysis in the form of STEM and TEM are planned in order to more deeply investigate the crack propagation and microstructures of the fatigued nanostructured alloys at UC Berkeley using a Quanta Dual Beam FIB/SEM with STEM capability and to manufacture FIB foils of the deformed regions to look at with the TEM at Lawrence Berkeley Lab at NCEM.

Optimization of this testing technique for further investigations on nuclear materials could be conducted to investigate the effect of neutron irradiation and different dose rates on the

evolution of the material's mechanical properties during cyclic loading as well as its fatigue life. In this case, a reduction of sample size is at a premium for safe handing as well as for extracting the most amount of statistics out of a limited sample volume.

From a basic materials science perspective, the investigation of micro fatigue bars of various sizes with various crystal structures and nanostructures employing this in situ fatigue testing technique could be employed to investigate intrinsic and extrinsic size effects and determine a method for linking this technique to macroscopic fatigue testing and determining if and how bulk mechanical properties can be obtained.

Bibliography

[1] M.D. Uchic, D.M. Dimiduk, J. Florando, W.D. Nix. Sample Dimensions Influence Strength and Crystal Plasticity. *Science*, 305(5686): 986-989, 2004.

[2] Zhao, Y. H., Liao, X. Z., Cheng, S., Ma, E. and Zhu, Y. T. (2006), Simultaneously Increasing the Ductility and Strength of Nanostructured Alloys. *Adv. Mater.*, 18: 2280–2283. doi:10.1002/adma.200600310.

[3] Witkin, David, et al. "Al–Mg alloy engineered with bimodal grain size for high strength and increased ductility." *Scripta Materialia* 49.4 (2003): 297-302.

[4] G.D. Smith, J.J. deBarbadillo, J.J. deBarbadillo (Ed.), *et al.*, Structural Applications of Mechanical Alloying, ASM-International, Materials Park, OH (1994), pp. 117–123.

[5] S. Ukai, M. Harada, H. Okada, M. Inoue, S. Nomura, S. Shikakura, K. Asabe, T. Nishida, M. Fujiwara, *J. Nucl. Mater.*, 204 (1993), p. 65

[6] S. Ukai, M. Harada, H. Okada, M. Inoue, S. Nomura, S. Shikakura, T. Nishida, M. Fujiwara. *J. Nucl. Mater.*, 204 (1993), p. 74

[7] S. Ukai, T. Nishida, H. Okada, T. Okuda, M. Fujiwara, K. Asabe, *J. Nucl. Sci. Tech.*, 34 (1997), p. 256

[8] S. Ukai, T. Yoshitake, S. Mizuta, Y. Matsudaira, S. Hagi, T. Kobayashi, *J. Nucl. Sci. Tech.*, 36 (1999), p. 710

[9] I-S. Kim, T. Okuda, C-Y. Kang, J-H. Sung, P.J. Maziasz, R.L. Klueh, K. Miyahara. *Met. Mater.*, 6 (2000), p. 513

[10] D.J. Larson, P.J. Maziasz, I.-S. Kim, K. Miyahara. *Scripta Mater.*, 44 (2001), p. 359

[11] I.-S. Kim, J.D. Hunn, N. Hashimoto, D.J. Larson, P.J. Maziasz, K. Miyahara, E.H. Lee. *J. Nucl. Mater.*, 280 (2000), p. 264

[12] E.A. Kenik, D.T. Hoelzer, P.J. Maziasz, M.K. Miller. *Microsc. Microanal.*, 7 (2001), p. 550

[13] M.K. Miller, E.A. Kenik. *Microsc. Microanal.*, 8 (Suppl 2) (2002), p. 1126CD

[14] M.K. Miller, E.A. Kenik, K.F. Russell, L. Heatherly, D.T. Hoelzer, P.J. Maziasz. *Mat. Sci. Eng. A*, 353 (2003), pp. 140–145

[15] M.K. Miller, D.T. Hoelzer, E.A. Kenik, K.F. Russell. *Microsc. Microanal.*, 9 (Suppl 2) (2003), pp. 44–45

[16] Odette, G. R., and D. T. Hoelzer. "Irradiation-tolerant nanostructured ferritic alloys: Transforming helium from a liability to an asset." *JOM* 62.9 (2010): 84-92.

[17] R.Z Valiev, R.K Islamgaliev, I.V Alexandrov. *Prog. Mater. Sci.*, 45 (2000), p. 103

[18] V.M Segal. *Mater. Sci. Eng. A*, 338 (2002), p. 331

[19] H Jiang, Y.T Zhu, D.P Butt, I.V Alexandrov, T.C Lowe. *Mater. Sci. Eng. A*, 290 (2000), p. 128

[20] A.P Zhilyaev, G.V Nurislamova, B.-K Kim, M.D Baró, J.A Szpunar, T.G Langdon. *Acta. Mater.,* 51 (2003), p. 753

[21] Y Saito, N Tsuji, H Utsunomiya, T Sakai, R.G Hong. *Scripta Mater.*, 39 (1998), p. 1221

[22] N Tsuji, Y Salto, H Utsunomiya, S Tanigawa. *Scripta Mater.*, 40 (1999), p. 795

[23] J.Y Huang, Y.T Zhu, H Jiang, T.C Lowe. *Acta Mater.*, 49 (2001), p. 1497

[24] Y.T Zhu, H Jiang, J Huang, T.C Lowe. *Metall. Mater. Trans. A*, 32 (2001), p. 1559

[25] R.S Mishra, M.W Mahoney, S.X McFadden, N.A Mara, A.K Mukherjee. *Scripta Mater.*, 42 (1999), p. 163

[26] J.-Q Su, T.W Nelson, C.J Sterling. *J. Mater. Res.*, 18 (2003), p. 1757

[27] Gianola, Daniel S., et al. "In situ nanomechanical testing in focused ion beam and scanning electron microscopes." *Review of Scientific Instruments* 82.6 (2011): 063901.

[28] Ukai, Shigeharu, and Masayuki Fujiwara. "Perspective of ODS alloys application in nuclear environments." *Journal of Nuclear Materials* 307 (2002): 749-757.

[29] E. O. Hall. The deformation and ageing of mild steel: Discussion of results. Proceedings of the Physical Society. Section B, 64(9):747, 1951.

[30] NJ Petch. The cleavage strength of polycrystals. *J. Iron Steel Inst.*, 174:25 28, 1953.

[31] Nguyen Q. Chinh, Tivadar Győri, Ruslan Z. Valiev, Péter Szommer, Gábor Varga, Károly Havancsák and Terence G. Langdon (2012). Observations of unique plastic behavior in

micro-pillars of an ultrafine-grained alloy. MRS Communications, 2, pp 75-78. doi:10.1557/mrc.2012.11.

[32] Kiener, Daniel, et al. "Application of small-scale testing for investigation of ion-beam-irradiated materials." *Journal of Materials Research* 27.21 (2012): 2724-2736.

[33] Kiener, Daniel, et al. "Influence of external and internal length scale on the flow stress of copper." *International Journal of Materials Research* 98.11 (2007): 1047-1053.

[34] Kiener, D., et al. "A further step towards an understanding of size-dependent crystal plasticity: In situ tension experiments of miniaturized single-crystal copper samples." *Acta Materialia* 56.3 (2008): 580-592.

[35] Kiener, Daniel, et al. "Determination of mechanical properties of copper at the micron scale." *Advanced Engineering Materials* 8.11 (2006): 1119-1125.

[36] Stölken, J. S., and A. G. Evans. "A microbend test method for measuring the plasticity length scale." *Acta Materialia* 46.14 (1998): 5109-5115.

[37] Motz, C., T. Schöberl, and R. Pippan. "Mechanical properties of micro-sized copper bending beams machined by the focused ion beam technique." *Acta Materialia* 53.15 (2005): 4269-4279.

[38] Demir, Eralp, and Dierk Raabe. "Mechanical and microstructural single-crystal Bauschinger effects: Observation of reversible plasticity in copper during bending." *Acta Materialia* 58.18 (2010): 6055-6063.

[39] Ukai, S., et al. "Tube manufacturing and mechanical properties of oxide dispersion strengthened ferritic steel." *Journal of nuclear materials* 204 (1993): 74-80.

[40] Z Horita, T Fujinami, T.G Langdon. *Mater. Sci. Eng. A*, 318 (2001), p. 34

[41] Y Saito, H Utsunomiya, H Suzuki, T Sakai. *Scripta Mater.*, 42 (2000), p. 1139

[42] Demkowicz, M. J., R. G. Hoagland, and J. P. Hirth. "Interface structure and radiation damage resistance in Cu-Nb multilayer nanocomposites." *Physical review letters* 100.13 (2008): 136102.

[43] Misra, A., et al. "The radiation damage tolerance of ultra-high strength nanolayered composites." *JOM* 59.9 (2007): 62-65.

[44] Mara, Nathan A., and Irene J. Beyerlein. "Review: effect of bimetal interface structure on the mechanical behavior of Cu–Nb fcc–bcc nanolayered composites." *Journal of Materials Science* 49.19 (2014): 6497-6516.

[45] Estrin, Yuri, and Alexei Vinogradov. "Fatigue behaviour of light alloys with ultrafine grain structure produced by severe plastic deformation: an overview." *International Journal of Fatigue* 32.6 (2010): 898-907.

[46] Schwaiger, R., and O. Kraft. "Size effects in the fatigue behavior of thin Ag films." *Acta Materialia* 51.1 (2003): 195-206.

[47] Khatibi, G., et al. "A study of the mechanical and fatigue properties of metallic microwires." *Fatigue & Fracture of Engineering Materials & Structures* 28.8 (2005): 723-733.

[48] Yang, B., et al. "Tensile behaviour of micro-sized copper wires studied using a novel fibre tensile module." *International Journal of Materials Research* 99.7 (2008): 716-724.

[49] Li, Xiaodong, and Bharat Bhushan. "Fatigue studies of nanoscale structures for MEMS/NEMS applications using nanoindentation techniques." *Surface and Coatings Technology* 163 (2003): 521-526.

[50] Cordill, M. J., N. R. Moody, and William W. Gerberich. "Effects of dynamic indentation on the mechanical response of materials." *Journal of Materials Research* 23.06 (2008): 1604-1613.

[51] Radivojević, Miljana, et al. "On the origins of extractive metallurgy: new evidence from Europe." *Journal of Archaeological Science* 37.11 (2010): 2775-2787.

[52] http://www.iceman.it/en/node/277

[53] Emsley, John (2003). *Nature's building blocks: an A-Z guide to the elements*. Oxford University Press. pp. 121–125. ISBN 978-0-19-850340-8.

[54] Edalati, Kaveh, et al. "Softening of high purity aluminum and copper processed by high pressure torsion." *International Journal of Materials Research* 100.12 (2009): 1668-1673.

[55] Renk, O., et al. "Direct evidence for grain boundary motion as the dominant restoration mechanism in the steady-state regime of extremely cold-rolled copper." *Acta materialia* 77 (2014): 401-410.

[56] C. Auer von Welsbach, Leuchtkörper für Incandescentbrenner, *DE*, 39 (1885), p. 162

[57] W. Nernst, Verfahren zur Erzeugung von elektrischem Glühlicht, *DRP*, 104 (1897), p. 872

[58] C. Auer von Welsbach, Aus Osmium bestehende Fäden für elektrische Glühlampen und Verfahren zu ihrer Herstellung**,** *DRP*, 138 (1898), p. 135

[59] W. von Bolton, O. Feuerlein, Die Tantallampe, eine neue Glühlampe der Firma Siemens & Halske AG, *Elektrotechn Z,* 26 (1905), p. 4, 105

[60] A. Just, F. Hanaman, Verfahren zur Herstellung von Glühkörpern aus Wolfram oder Molybdän für elektrische Glühlampen, *DRP*, 154 (1903), p. 262

[61] P.K. Johnson, Tungsten filaments—the first modern PM Product, *Int. J. of Powder Met.*, 44 (2008), p. 4, 43

[62] Coolidge WD. Tungsten and method of making the same for use as filaments of incandescent electric lamps and for other purposes. US Patent 1,082,933 (1913).

[63] C. Agte, J. Vacek, Wolfram und MolybdänAkademie Verlag, Berlin (1959)

[64] F. H. Froes, J. J. deBarbadillo and C. Suryanarayana Structural Applications of Mechanical Alloying Eds. Froes and deBarbadillo, ASM Intl., 1, 1990

[65] Murr, L. E. "Interfacial energetics in the TD-nickel and TD-nichrome systems."*Journal of Materials Science* 9.8 (1974): 1309-1319.

[66] H Jiang, Y.T Zhu, D.P Butt, I.V Alexandrov, T.C Lowe, *Mater. Sci. Eng. A*, 290 (2000), p. 128

[67] V.M Segal, *Mater. Sci. Eng. A*, 338 (2002), p. 331

[68] A.P Zhilyaev, G.V Nurislamova, B.-K Kim, M.D Baró, J.A Szpunar, T.G Langdon, *Acta. Mater.*, 51 (2003), p. 753

[69] Y Saito, N Tsuji, H Utsunomiya, T Sakai, R.G Hong, *Scripta Mater.*, 39 (1998), p. 1221

[70] N Tsuji, Y Salto, H Utsunomiya, S Tanigawa, *Scripta Mater.*, 40 (1999), p. 795

[71] J.Y Huang, Y.T Zhu, H Jiang, T.C Lowe, *Acta Mater.*, 49 (2001), p. 1497

[72] Y.T Zhu, H Jiang, J Huang, T.C Lowe, *Metall. Mater. Trans. A*, 32 (2001), p. 1559

[73] R.S Mishra, M.W Mahoney, S.X McFadden, N.A Mara, A.K Mukherjee, *Scripta Mater.*, 42 (1999), p. 163

[74] J.-Q Su, T.W Nelson, C.J Sterling, *J. Mater. Res.*, 18 (2003), p. 1757

[75] V.V Stolyarov, Y.T Zhu, I.V Alexandrov, T.C Lowe, R.Z Valiev, *Mater. Sci. Eng. A*, 343 (2003), p. 43

[76] Y.S Sato, Y Kurihara, S.H.C Park, H Kokawa, N Tsuji, *Scripta Mater.*, 50 (2004), p. 57

[77] A.P Zhilyaev, J Gubicza, G Nurislamova, Á Révész, S Suriñach, M.D Baró, *et al.*, *Phys. Status Solidi A*, 198 (2003), p. 263

[78] V.V Stolyarov, Y.T Zhu, T.C Lowe, R.Z Valiev, *Nanostruct. Mater.*, 11 (1999), p. 947

[79] O. Richmond and M.L. Devenpeck, 4th US Congress on Appl. Mech., ASME (1967) 1053.

[80] B.I. Smirnov, Dislocation Structure and Strengthening of Crystals (in Russian), Nauka, L., 1981.

[81] P.L. Sue and K.S. Havner, *J. Mech. Phys. Solids*, 32 (6) (1983) 417.

[82] V.M. Segal, V.I. Reznikov, A.E. Drobyshevskiy and V.I. Kopylov, *Russian Metallurgy*, (Engl. Transl.), 1 (1981) 115.

[83] V.M. Segal, Patent of the USSR, No. 575892, 1977.

[84] Y.T. Zhu and T.C. Lowe., *Mat. Sci. and Eng. A* 291 (2000) 46-53.

[85] K. Nakashima, Z. Horita, M. Nemoto, T.G. Langdon, *Acta Mater*. 46 (1998) 1589.

[86] P.B. Prangnell, A. Gholinia, V.M. Markushev, in: T.C. Lowe, R.Z. Valiev (Eds.), Investigations and Applications of Severe Plastic Deformation, Kluwer Academic Pub., Dordrecht, 2000, pp. 65–71

[87] P.W. Bridgeman, Studies in Large Plastic Flow and Fracture, McGraw-Hill, New York, 1952.

[88] Zhilyaev AP, Lee S, Nurislamova GV, Valiev RZ, Langdon TG. *Scr. Mater.* 2001; 44:2753.

[89] A. P. Zhilyaev and T. G. Langdon. Using high-pressure torsion for metal processing: Fundamentals and applications. *Progress in Materials Science*, 53(6):893 _ 979, 2008.

[90] R. Pippan, F.Wetscher, M. Hafok, A. Vorhauer, and I. Sabirov. The limits of refinement by severe plastic deformation. *Advanced Engineering Materials*, 8(11):1046_ 1056, 2006.

[91] E.J. Pavlina, C.J. Van Tyne. *Journal of Materials Engineering and Performance*, December 2008, Volume 17, Issue 6, pp 888-893.

[92] W. A. J. Albert, Uber Treibseile am Harz. *Archiv ffir Mineralogie, Georgnosie. Bergbau und Hiittenkunde* 10, 215-234 (1837).

[93] W. J. M. Rankine, On the causes of the unexpected breakage of the journals of railway axles, and on the means of preventing such accidents by observing the law of continuity in

their construction. Institution of Civil Engineers, Minutes of Proceedings, Vol. 2, pp. 105-108, London (1842).

[94] A. Morin, Lemons de m6canique practique---resistance des materiaux. Paris, Librairie de L. Hachette et Cie, p. 456 (1853).

[95] F. Braithwaite, On the fatigue and consequent fracture of metals. Institution of Civil Engineers, Minutes of Proceedings, Vol. XlI1, pp. 463-474, London (1854).

[96] A. Wohler, Versuche zur Ermittlung der auf die Eisenbahnwagenachsen einwirkenden Krifte und die Widerstandsfihigkeit der Wagen-Achsen. Zeitschrift fiir Bauwesen. X, 583-616 (1860).

[97] A. Wohler, Bericht fiber die Versuche, welche auf der konigl. Niederschlesisch-miirkischen eisenbahn mit Apparaten zum Messen der Biegung und Verdehung von Eisenbahnwagenachsen wihrend der Fahrt angestellt wurden. Zeitschrift fiir Bauwesen, VIII, 641- 652 (1858).

[98] A. Wohler, Uber die Festigkeits-Versuche mit Eisen und Stahl. Zeitschriftfiir Bauwesen, XX, 73-106 (1870).

[99] A. Wohler, Ober die Festigkeitsversuche mit Eisen und Stahl. Auf Anordnung des Ministers fiir Handel, Gewerbe uffentl. Arbeiten, Grafen Itzenblitz, angestellt. Berlin, Ernst und Korn (1870).

[100] A. Wohler, Achsen, deren Dimensionen, Form der Achsschenkel, Material, in Handbuch fiir Spezielle Eisenbahn-Technik. 2. Band. Der Eisenbahn-Wagenbau in seinem ganzen Umfange. E. Heusinger von Waldegg Hrsg. Verlag Wilhelm Engelmann, Leipzig (1870).

[101] W. Kloth and Th. Stroppel, Kriifte, Beanspruchungen und Sicherheiten in den Landmaschinen. Z-VDI g0, 85-92 (1936).

[102] J. A. Ewing et J. C. W. Humfrey. The fracture of metals under repeated alternations of stress, *Proceedings of the Royal Society of London (1854-1905)*, 1903

[103] J. Bauschinger, Ober die Verinderung der Elastizititsgrenze und der Festigkeit des Eisens und Stahls durch Strecken und Quetschen, durch Erwormen und AbkiJhlen und durch oftmals wiederholte Beanspruchung. *Mitt. Mech.-Tech. Lab. Miinch.* 13, 1-115 (1886).

[104] J. Bauschinger, lIber die Verinderung der Elastizititsgrenze und des Elastizititsmoduls verschiedener Metalle. *Civilingenieur* XXVII, pp. 289-348, Felix, Leipzig (1881).

[105] J. Bauschinger, Ober das Kristallinischwerden und die Festigkeitsverminderung des Eisens durch den Gebrauch. Dinglers J. 235, 169-173 (1880).

[106] H. J. Gough, The Fatigue of Metals. London, Scott, Greenwood (1924).

[107] Laird, Campbell, Philip Charsley, and Haël Mughrabi. "Low energy dislocation structures produced by cyclic deformation." *Materials Science and Engineering* 81 (1986): 433-450.

[108] Mughrabi, H. "The cyclic hardening and saturation behaviour of copper single crystals." *Materials Science and Engineering* 33.2 (1978): 207-223.

[109] KOZLOV, E. V., ZHDANOV, A. N., KONEVA, N.A., *Physical Mesomechanics*, 2008, Vol. 11, 1-2, p. 95

[110] KOZLOV, E. V., KONEVA, N.A., TRISHKINA, L. I., ZHDANOV, A. N., FEDORISCHEVA, M. V., *Materials Science Forum*, 2008, Vols. 584-586, p. 35-40

[111] Mughrabi, H., H. W. Höppel, and M. Kautz. "Fatigue and microstructure of ultrafine-grained metals produced by severe plastic deformation." *Scripta Materialia* 51.8 (2004): 807-812.

[112] Höppel, H. W., et al. "Microstructural study of the parameters governing coarsening and cyclic softening in fatigued ultrafine-grained copper." *Philosophical Magazine A* 82.9 (2002): 1781-1794.

[113] Ukai S, Ohtsuka S. Low cycle fatigue properties of ODS ferritic-martensitic steels at high temperature. *Journal of Nuclear Materials* 2007;367-370:234-8.

[114] I. Kubena, T. Kruml, P. Spätig, N. Baluc, Z. Oksiuta, M. Petrenec, K. Obrtlík, J. Polák, *Pro. Eng. 2* (2010) 717–724

[115] Kubena, Ivo, Benjamin Fournier, and Tomas Kruml. "Effect of microstructure on low cycle fatigue properties of ODS steels." *Journal of Nuclear Materials* 424.1 (2012): 101-108.

[116] R. Valiev, et al., *Acta Met. Mat.* 42 (1994) 2467-2475

[117] R. Valiev, *Mat. Sci. and Eng*. A234-236 (1997) 59-66.

[118] R.O. Ritchie, *Int. Journal of Fracture*. 100 (1999) 55-83.

[119] R.R. Ambriz and V. Mayagoitia (2011). Welding of Aluminum Alloys, Recent Trends in Processing and Degradation of Aluminium Alloys, Prof. Zaki Ahmad (Ed.), ISBN: 978-953-307-734-5, InTech, Available from: http://www.intechopen.com/books/recent-trends-in-processing-and-degradation-of-aluminium-alloys/weldingof-aluminum-alloys

[120] Aurelio Somà and Muhammad Mubasher Saleem, *J. Micromech. Microeng.* 25 (2015) 055007 (15pp)